# METHYLAMMONIUM ACETATE ASSISTED DEPOSITION OF HYBRID HALIDE PEROVSKITE FOR EFFICIENT DEVICES

by

Mehedhi Hasan, M.S.

A dissertation submitted to the Graduate Council
of Texas State University in partial fulfillment
of the requirements for the degree of
Doctor of Philosophy
with a Major in Materials Science, Engineering and Commercialization
August 2019

Committee Members:

Alex Zakhidov, Chair

Edwin L Piner

Wilhelmus J. Geerts

Casey Smith

William Chittenden

## FAIR USE AND AUTHOR'S PERMISSION STATEMENT

### Fair Use



### Duplication Permission

## DEDICATION

I would like to dedicate this dissertation to my family members for all the guidance, encouragement and support throughout my life.

## ACKNOWLEDGEMENTS

First, I would like to take this opportunity to express my sincere gratitude to my advisor Dr. Alex Zakhidov for offering his guidance and the opportunity to work in his lab over the last four years. He helped me in numerous ways during the challenging research I was a part of and provided access to our excellent lab facilities. Dr. Zakhidov not only helped me in academic matters, but also in adjusting to the completely new culture as a newcomer from the other side of the world. Without his active supervision it would not be possible to complete my work and this thesis.

I would also like to thank the other members of my dissertation committee, Dr. Edwin L. Piner, Dr. Wilhelmus J. Geerts, Dr. Casey Smith, Dr. William Chittenden for their time and valuable suggestions. I am especially grateful to Dr. Casey Smith, who helped me above and beyond his regular schedule regarding instruments and analysis.

I would like to thank Dr. Dmitry Lyashenko for the technical training in the organic semiconductor lab and ARSC facilities. I would specially acknowledge my colleague Dr. Swaminathan Venkatesan. We worked together for the solar cell project from the beginning to end. I have achieved many technical skills, software skills and analysis skill thanks to him.

I would like to acknowledge Dr. Mark Hotlz for giving the opportunity to use the low temperature probe station. I am very thankful to Dr. Sanjoy Paul, who is an expert of low temperature transport study. He helped in data collection, analysis and report preparation for whole temperature dependent study.

I am thankful to my fellow lab mate Dr. Chris Manspeaker, Kevin Lyon, Eric Welch, Tanjina Ahmed, Garrett Merrion, Nischal Khakurel, Aureliano Perez, Joseph Sadler. Dr. Manspeaker was my colleague for the longest time in the lab. He not only supported during the experimental work in the lab but did a thorough review of my dissertation from remote without any hesitation.

My gratitude and appreciation are not enough for my wife Rafea Sultana Rea, whose support and encouragement has helped me greatly through these last few years. I look forward to helping her through her journey as she has helped me.

Many thanks to my friend Anwar Siddique and Raju Ahmed for sharing their experience, characterization and analysis skills and endless support throughout the graduate life.

I wish to thank Dr. Jennifer Irvin, Dr. Clois Powell and Dr. Gary Beall for their guidance and encouragement.

I also like to thank MSEC staff Pizana Karla and Kelsie Crumpton; SRO staff Alissa Savage, Dr. Juan Gomez, Nate England, MSEC colleague Md. Dalim Mia, Joyce Anderson.

I would like to acknowledge *ONR HBCU/MI Instrumentation grant* (#W911NF-16-1-0518, Program Manager Dr. Paul Armistead) and *American Chemical Society Petroleum Research Fund* grant (#UNI656095-UNI6, Program Manager Dr. Askar Fahr) for financial support.

Finally, I wish to acknowledge, all the members (this can be a very big list of names) of *Bangladesh Student Association* community who made San Marcos my second home also made the graduate life eventful.

## TABLE OF CONTENTS

**Page**

## LIST OF TABLES

**Table** **Page**

## LIST OF FIGURES

**Figure** **Page**

## LIST OF ABBREVIATIONS

| | |
|---|---|
| $ABX_3$ | Generic chemical formula for a perovskite |
| AFM | Atomic Force Microscopy |
| Ag | Silver |
| Al | Aluminum |
| AM1.5G | Global Air Mass Standard 1.5 |
| BCP | Bathocuproine |
| Bphen | Bathophenathroline |
| Br | Bromine |
| C60 | Fullerene 60 |
| CaTiO3 | Calcium titanate |
| CdTe | Cadmium telluride |
| CE | Counter electrode |
| CFC | Chlorofluorocarbon |
| $CH_3NH_2$ | Methylamine |
| $CH_3NH_3PbI_3$ | Methylammonium lead iodide |
| CIGS | Copper indium gallium selenide |
| Cl | Chlorine |
| C-V | Capacitance - Voltage |
| DEC | Diethyl carbonate |
| DLCP | Drive level capacitance profiling |
| DMF | N, N-dimethylformamide |
| DMSO | Dimethyl sulfoxide |
| $E_a$ | Activation energy |
| CompleteEASE | Ellipsometry data analysis software |
| EDS | Energy dispersive spectroscopy |

| | |
|---|---|
| EQE | External quantum efficiency |
| ETL | Electron transport layer |
| FA | Formamidinium |
| FET | Field effect transistor |
| FF | Fill factor |
| FIB | Focused ion beam |
| FTIR | Fourier-transform infrared spectroscopy |
| GaAs | Gallium arsenide |
| GaN | Gallium nitride |
| GBL | γ-butyrolactone |
| Ge | Germanium |
| GEN-OSC | General oscillator |
| HCFC | Hydrochlorofluorocarbons |
| He | Helium |
| HFE | Hydrofluroether |
| HOMO | Highest occupied molecular orbital |
| I | Iodine |
| $I_{mp}$ | Current at maximum power point |
| IP | Ionization potential |
| $I_{PC}$ | Peal cathode current |
| $I_{SC}$ | Short circuit current |
| ITO | Indium tin oxide |
| I-V | Current-Voltage |
| $J_{SC}$ | Short circuit current density |
| J-V | Current density- Voltage |
| J-V-L | Current density-voltage-luminance |
| LED | Light emitting diode |

| | |
|---|---|
| LiF | Lithium fluoride |
| LiTFSI | Bis (trifluoromethane) sulfonimide lithium |
| LUMO | Lowest unoccupied molecular orbital |
| MA | Methylammonium (cation) |
| MAAc | Methylammonium Acetate ($NH_4CH_3CO_2$) |
| MAI | Methylammonium iodide |
| $MAPbBr_3$ | Methylammonium lead bromide |
| $MAPbX_3$ | Methylammonium lead halide |
| MAPI | Methylammonium lead iodide |
| MAX | Methylammonium halide |
| MSE | Mean square error |
| NaOH | Sodium hydroxide |
| NMP | N-methyl-2-pyrrolidone |
| OLED | Organic light emitting diode |
| Pb | Lead |
| $Pb(Ac)_2$ | Lead acetate |
| $PbI_2$ | Lead iodide |
| $PbX_2$ | Lead halide |
| PCE | Power conversion efficiency |
| PEDOT: PSS | Poly (3,4-ethylenedioxythiophene) polystyrene sulfonate |
| PeLED | Perovskite light emitting diode |
| PhA | Phenylammonium |
| PL | Photoluminescence |
| PMMA | Poly methyl methacrylate |
| PTFE | Polytetrafluoroethylene |
| RE | Reference electrode |
| RH | Relative humidity |

| | |
|---|---|
| $R_s$ | Series resistance |
| $R_{sh}$ | Shunt resistance |
| SE | Spectroscopic ellipsometry |
| SEM | Scanning electron microscopy |
| Si | Silicon |
| SiC | Silicon carbide |
| Sn | Tin |
| SPM | Scanning probe microscopy |
| SRH | Shockley-Read-Hall |
| TFT | Thin film transistor |
| TRPL | Time-resolved photoluminescence |
| UV-Vis | Ultraviolet-visible |
| VESTA | Visualization for electronic structural analysis- a software for crystal structure study |
| $V_{mp}$ | Voltage at maximum power point |
| $V_{OC}$ | Open circuit voltage |
| WE | Working electrode |
| XPS | X-ray photoelectron spectroscopy |
| XRD | X-ray Refraction Diffraction |
| λ | Wavelength |
| τ | Recombination lifetime |
| η | Efficiency |

## ABSTRACT

Hybrid halide perovskites have emerged as competitive semiconducting materials for optoelectronic devices due to their superior optoelectronic properties and low cost processability. Current perovskite solar cell efficiency fabricated in lab is 24.2% which is approaching towards the maximum theoretical limit of 30.14% in a fast pace. However, commercialization ventures of this technology are experiencing some key challenges. Production scalability, operational stability in various extreme environment, and toxicity of the materials are three main concerns. Attempt to scale up the solar cells for large panels cannot retain the high efficiency as in lab scale. One of the main reasons behind this limitation is inability to deposit high quality active perovskite film on large area substrates. The conventional approach to create high quality films from solution is to introduce additional arrangement or increasing process steps. These solutions result in impressive film quality, however are unsuitable for large scale film deposition. In this dissertation, an optimum ink formulation was developed for methylammonium lead iodide (MAPI) perovskite instead of increasing process steps to improve film quality. An additive named methylammonium acetate (MAAc) was introduced to the precursor solution at different ratio to retard the reaction kinetics by forming an intermediate phase. The processing parameters were determined for high quality film deposition. Films derived from different MAAc precursor ratios were characterized using SEM, XRD, XPS, UV-Vis, PL, and ellipsometry. Finally, solar cells and light emitting diodes were fabricated to evaluate the perovskite films in functioning devices.

Further, the performance and operational stability of the MAPI solar cell devices were investigated under wide range of temperature and illumination intensities to interrogate the performance in various extreme conditions. The temperature range (40 – 430 K) covers two phase transition points of perovskite. Recombination of generated carriers is one of the foremost loss mechanisms in the solar cell. The combined intensity dependent short circuit density ($J_{SC}$) and open circuit voltage ($V_{OC}$) analysis were exploited for a recombination study. The mixture of bimolecular and trap-assisted recombination was observed in the devices.

MAPI thin films are soluble in most of the polar organic solvents and thus until now they were not considered suitable for electrochemical processing. In this work, we report on hydrofluroether (HFE) solvent-based electrolyte for electrochemical processing and characterization of perovskite thin films. The results obtained here show that chemically orthogonal electrolytes based on HFE solvents do not dissolve organic perovskite films and thus allow electrochemical characterization of the electronic structure, investigation of charge transport properties and potential electrochemical doping of the films with in-situ diagnostic capabilities.

# 1. INTRODUCTION

## 1.1 Overview

In the quest of better alternatives to reduce the cost and improve the performance of electronic devices, scientists are continuously looking for newer semiconductors for different applications. Since the mid-20$^{th}$-century semiconductor device fabrication technology is advancing fast. Although the current semiconductor industries are mainly dominated by inorganic semiconductors, particularly by silicon (Si), the research for new type semiconductors has been going on for last half of the century. So far developed semiconductors can be classified in three main groups: inorganic, organic and hybrid semiconductor. The mostly used inorganic semiconductors are silicon (Si), gallium arsenide (GaAs), gallium nitride (GaN), germanium (Ge), silicon carbide (SiC), cadmium telluride (CdTe) and copper indium gallium selenide/sulfide (CIGS) etc. All types of devices currently in use, can be fabricated using inorganic semiconductor. The inorganic semiconductor technology is technically and commercially matured. Devices based on organic semiconductor were first reported in 1973 [1]. Later in 1986, the first organic solar cell of 1% efficiency was reported [2]. Recently, organic semiconductor exhibited remarkable success in organic light emitting diode (OLED) technology. The state-of-the-art commercial displays of smart phones (e.g. Samsung, iPhone) are made of OLED. While research on organic semiconductor devices are in progress, very recently a new class of semiconductors named hybrid semiconductors came into the spotlight. Hybrid semiconductors have both inorganic and organic constituent in their structure. Organic-inorganic hybrid halide perovskite (later we use the term “hybrid perovskite” or “perovskite”) made incredible progress in photovoltaic device efficiency in less than a decade. Within seven years the perovskite solar cell efficiency jumped to more than 24%

[3], which is comparable to the efficiency of CdTe thin film solar cell [4]. Perovskite based light emitting diodes (LED) achieved quantum efficiencies up to 8%. Two years ago the efficiencies of those devices was 3.5% [5]. The comparative performance improvement of perovskite solar cell with other third generation solar cells are presented in fig. 1.1 for the period of 1985 to 2015. The steepest line starting at 2009 represents the remarkable efficiency increase of perovskite-based solar cell.

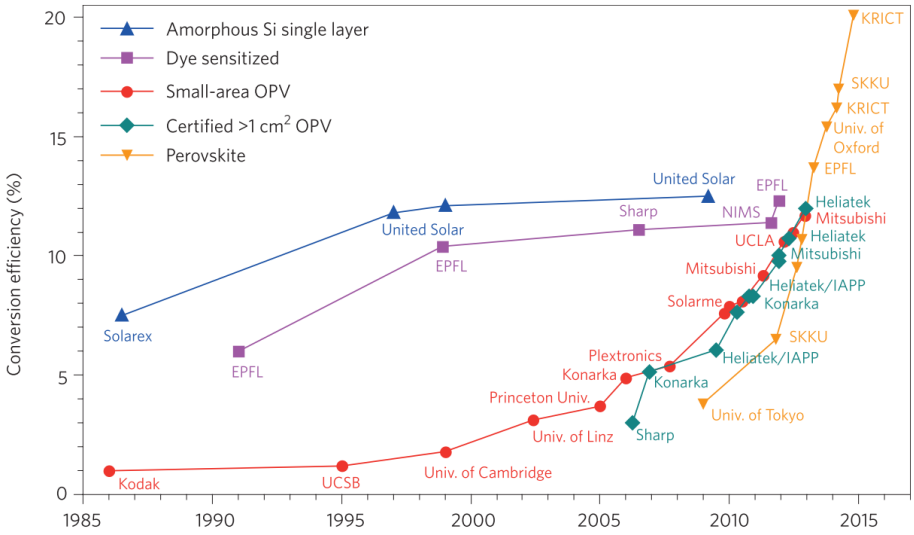


Fig. 1.1 Comparative progress in efficiency of perovskite solar cell with other third generation solar cells [6].

Hybrid halide perovskite possesses a lot of desired properties which one would like for optoelectronic devices. The prominent properties that attract researcher's attention are the ease of processing and the low material cost. Unlike conventional semiconductor materials, hybrid perovskites can be deposited by spin coating from the precursor solution of constituent chemicals on a wide variety of substrates including flexible plastics. Since there is no major issue regarding the substrate selection, perovskite devices can be fabricated on inexpensive substrates. Moreover, by changing

the chemical precursor(s) and relative ratio thereof the bandgap can be engineered easily. This feature facilitates synthesis of desired material of chosen properties in a facile way. To utilize all the advantageous features, researchers have developed a lot of different techniques for high quality perovskite deposition. The attempts to enhance the film quality makes the process more complicated and limits the process window. As a result, for achieving high quality films the techniques are no more remaining facile. Sometime the process windows of the developed methods are so narrow that a minor change in the process environment impacts the reproducibility greatly. Being comparatively young, the technology perovskite devices is still under investigation. Although the initial proof of concept for the potential of perovskite devices has already been established, there are some key challenges to overcome for commercialization. First, the stability of the material. Perovskite is not yet a stable material like the competitive inorganic semiconductors. Second, almost all the reported best performances of perovskite devices are on small devices. Commercialization requires the development of process that can be scaled up.

For commercial upscaling, it is crucial to develop a facile scalable, reproducible yet less expensive perovskite deposition technique that results in high quality thin films. In this dissertation, we report a facile perovskite deposition protocol. We investigated the properties of the developed thin film by different characterization techniques. Then the solar cell and light emitting diode (LED) were fabricated using as developed perovskite films to determine the best recipe of film deposition from device performances. Perovskite materials are extremely photosensitive. This family of materials also changes phase within the temperature range from 50 K – 400 K. Solar cell efficiency strongly

depends on the intensity of illumination. In a real operating environment both the temperature and the light intensity changes continuously. In some cases, the operating temperature can exceeds 85°C [7]. Therefore, it is essential to investigate the performances, and transport mechanism and optimum operating window of the perovskite devices over a wide range of light intensities and operating temperatures. Temperature and light intensity dependent studies pave the way to understand some key transport mechanism in the device interfaces. The temperature and light intensity dependent solar cell performance were studied here.

This study can provide us valuable information on how the devices will perform in a real environment and will provide further insight of temperature and illumination intensity dependent transport.

While the solution-based deposition of perovskite is being studied all around the world, the solution-based characterization such as an electrochemical study for perovskite is barely reported. The reason behind this is the unavailability of a suitable electrolyte that will not dissolve the perovskite. The development of suitable electrolytes and an electrochemical toolkit for perovskite studies are also reported on this dissertation.

## 1.2 Perovskite: Hybrid halide perovskites

This section is devoted to introducing the perovskite material with more technical information. The name perovskite is adopted from the mineral named calcium titanium oxide ($CaTiO_3$) due to the structural analogy. Calcium titanium oxide ($CaTiO_3$) was first discovered in 1839 by a German mineralogist Gustav Rose and was named after the Russian mineralogist, nobleman and a politician Lev A. Perovski who first characterized the structure [8]. The scope of this dissertation includes organic-inorganic hybrid halide

perovskites which have emerged as competitive semiconducting materials for devices due to their superior optoelectronic properties and low processing cost. In this dissertation the term *"perovskite"* always refers to *"organic inorganic hybrid halide perovskite"*.

Like its inorganic counterparts, hybrid halide perovskite is a family of compounds represented by the general chemical formula $ABX_3$. A is the organic cation, B is the metal cation and X is the halide anion. Fig. 1.2. (a) illustrates the basic crystal structure and (b) shows the typical representatives of A, B and X of the perovskite family along with its crystal structure.

As shown in the schema, a 3D network is formed by the corner sharing $BX_6$ octahedra. The cation 'A' occupies the central cavity of the network. The organic cations can be methylammonium (MA), formamidinium (FA) and phenylammonium (PhA). The metal cations can be Sn or Pb and the halide anions can be Cl, Br, I or composite of them [5].

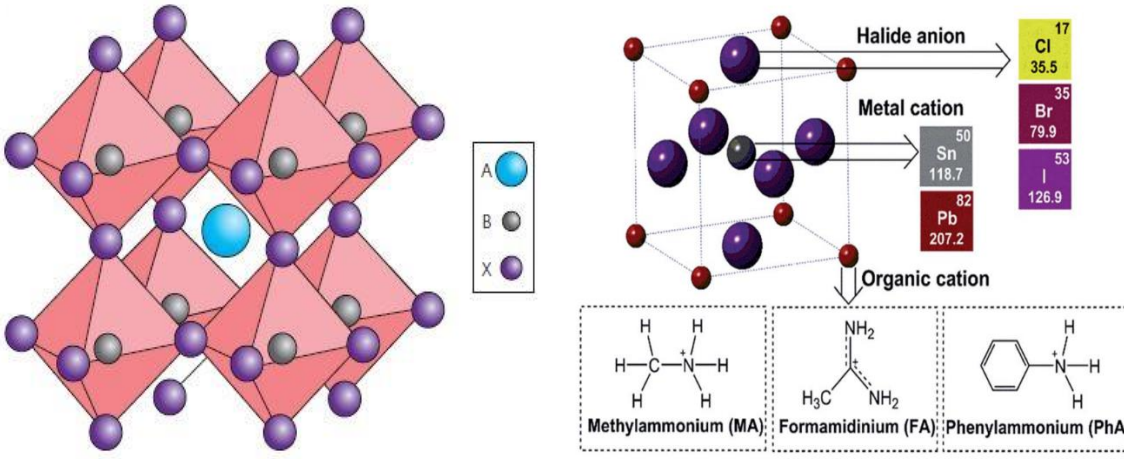


(a) (b)

Fig. 1.2 (a) Basic crystal structure of a generic perovskite [9] (b) Typical representatives of A, B and X of perovskite family along with its crystal structure [10].

By varying the 'A', 'B' and 'X', a lot of different perovskites can be realized. All the perovskite phases are not equally stable. The crystallographic stability of a perovskite species is determined by the tolerance factor '$t$' and octahedral factor μ developed by Goldschimidt (see equation 1.1 and 1.2).

$$t = \frac{R_A + R_X}{\sqrt{2(R_B + R_X)}} \qquad (1.1)$$

$$\mu = R_B / R_X \qquad (1.2)$$

Here, $R_A$, $R_B$ and $R_X$ are the ionic radii of the $A, B$ and $X$ respectively. The ideal value of the tolerance factor is $t = 1$. However, a stable cubic structure of hybrid perovskites can be acquired if $0.89 < t < 1$ and $\mu < 0.442$ [8], [9]. Deviation of tolerance factor from above mentioned acceptable range results in an orthorhombic or tetragonal phase. As a representative of stable perovskite the current discussion will be based on methylammonium lead iodide ($CH_3NH_3PbI_3$) which has a tolerance factor slightly higher than 0.9 [11]. This material is often referred to as $MAPbI_3$ or simply MAPI for convenience. MAPI is one of the most studied hybrid perovskites in the whole perovskite family. Apart from the constituent ion's radius, at different temperature and pressure the perovskite crystal may have different phases. The following table 1.1 summarizes the phases, the transition temperatures, the lattice constants and the volume of the unit cell. Note that, the transition temperature from tetragonal to cubic is ~55°C which is in the typical device operating range (-40°C to 85°) [11].

Table 1.1 Phase transition points and crystallographic information of MAPI, (adopted from ref. [11]).

| Phase | Temperature (K) | Crystal System | Space Group | Lattice (pm) | Volume ($10^4$ pm$^3$) |
|---|---|---|---|---|---|
| $CH_3NH_3PbI_3^-$ | | | | | |
| α | >327.4 | cubic | Pm3m | a = 632.85(4) | 253.5 |
| β | 162.2–327.4 | tetragonal | I4/mcm | a = 885.5(6)<br>c = 1265.9(8) | 992.6 |
| γ | <162.2 | orthorhombic | $Pna2_1$ | a = 886.1(2)<br>b = 858.1(2)<br>c = 1262.0(3) | 959.5 |

## 1.3 Optoelectronic properties of perovskite

Hybrid halide perovskites have been reported predominantly for optoelectronic devices such as solar cells and light emitting diodes (LED). Thin film transistors are also fabricated using perovskite as channel material. Both solar cells and LEDs are studied for this this dissertation. This section reviews the optoelectronic and electrical transport properties of perovskite materials. Perovskite is reported to be an extraordinary absorber material for photovoltaic solar cell. Moreover, it exhibits as light emitting properties and being investigated for application in light emitting diodes (LED). An efficient absorber material for solar cell can absorb from visible to near infrared range (350 – 950 nm) [12]. Perovskites exhibit a very high optical absorbance across the whole visible spectrum. Fig. 3. (a) shows the absorbance of several lead (Pb) and tin (Sn) based perovskites including MAPI. Note that change in cations causes the change of the onset of absorption in the spectrum. Likewise, by changing the halide ion or using a composite halide ion mix, one can change the absorption properties of the material [13]. Thus, the bandgap can be tuned by changing the composition of $ABX_3$. Moreover, the sharp absorption peak and large absorption coefficient of the perovskite are indicative of it being a direct bandgap

semiconductor. The range of tunable bandgap is from 1.3eV to 2.3 eV which cover the major portion of visible light. Fig. 1.3 (b) depicts the bandgap of three different member of perovskite family with their associated HOMO and LUMO level. 1.34eV is the optimum bandgap to achieve the Shockley-Queisser limit resulting in a 33.5% solar cell efficiency [5]. The bandgap of benchmark MAPI perovskite is ~1.59 eV which is very close to the Shockley-Queisser optimum bandgap. Its onset of absorption is approximately 800nm.

Fig. 1.4 pictures the solar radiation spectra at the top of the atmosphere and at the sea level. Note that the maximum radiation is observed for the visible range, i.e from 400nm – 700nm. Clearly MAPI has the desired absorption range for solar energy harvester.

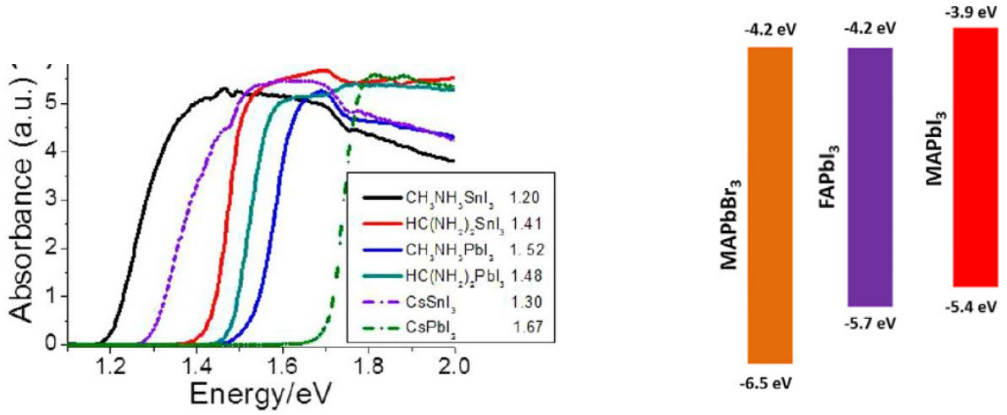


(a) (b)

Fig. 1.3 (a) Absorption spectra of few perovskite compound (b) Bandgap of three perovskite compounds [14].

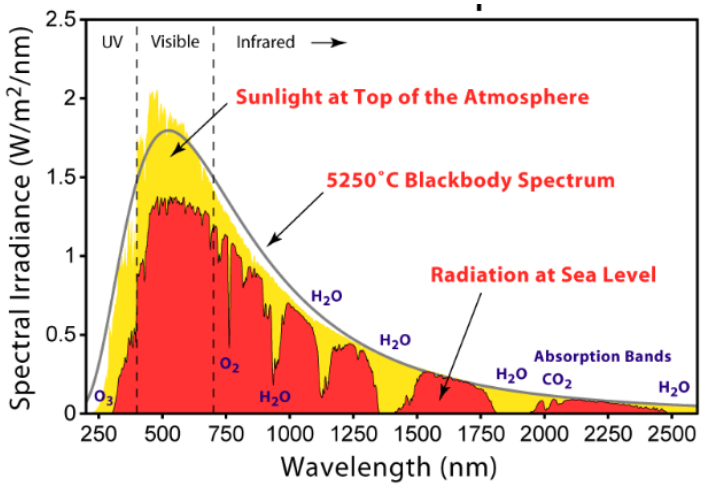


Fig. 1.4 Solar radiation spectra.

An outstanding solar cell material is often also an excellent photo emitter. An ideal LED emitter exhibits radiative recombination of charge carriers. Tunability of bandgap is a desired property to achieve different color LEDs. Ambipolar transport can maximize the efficiency of the devices. Fortunately, perovskites are outstanding candidate material for LEDs due to having all the desired attributes. LEDs are fabricated from the materials in the $MAPbX_3$ family include green and red light [5].

## 1.4 Perovskite deposition techniques

A wide variety of methods have been developed to produce high-quality perovskite layers [15]. All perovskite deposition methods broadly can be classified into three main categories,

(I) Solution based synthesis

(II) Vapor phase synthesis

(III) Hybrid synthesis, i.e. combination of (I) and (II).

All the above-mentioned techniques are graphically represented in fig. 1.5.

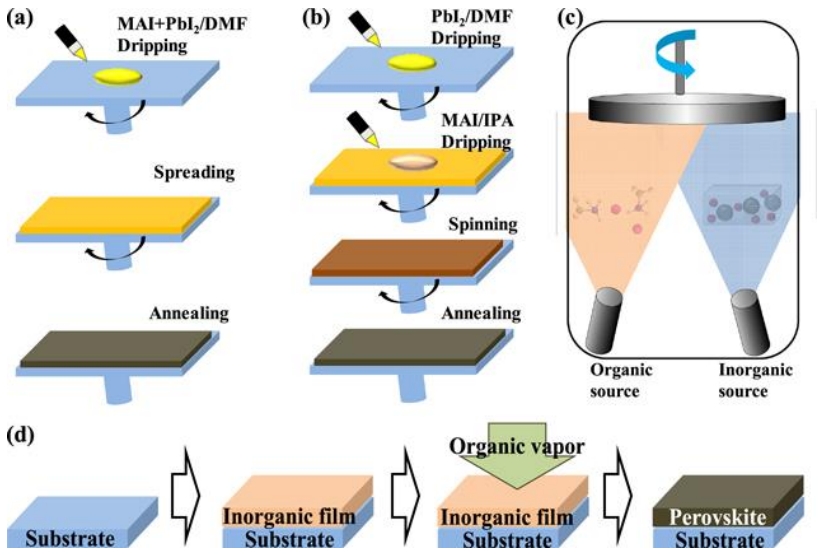


Fig. 1.5 Schematic diagram of perovskite deposition techniques. (a) One-step precursor deposition, (b) two-step sequential deposition method, (c) Vapor deposition and (d) Hybrid deposition. [16]

Solution based deposition is the most commonly used technique to create perovskite thin films and is used by a lot of research group worldwide. Organic-inorganic trihalide perovskite films are deposited from solutions that consists of an organic salt, e.g. methylammonium halide (MAX, here X=Cl, Br, I) and an inorganic salt, e.g. lead halide ($PbX_2$). Organic solvents (N,N-dimethylformamide (DMF) [17], γ-butyrolactone (GBL) or dimethyl sulfoxide (DMSO) [18]) dissolve the constituent salts. The solution is spin casted onto the substrate followed by an annealing step at approximately 100°C. The spin coating technique can further be classified as a single step or two step deposition. In the single step method, both organic and inorganic precursors are dissolved in a solvent and spin casted on the substrate as shown in fig. 1.5 (a). In the two step deposition, the inorganic precursor is deposited by spin coating first followed by dipping in an organic solution (fig. 1.5 (b))[19].

A schematic diagram of a solvent free thermal evaporation vapor deposition process is given in fig. 1.5 (c). In this technique, inorganic precursor (e.g. $PbX_2$) and organic precursor (MAX) are placed in a crucible and heated simultaneously up to their sublimation temperatures. The substrate is maintained at room temperature to avoid phase conversion of the grown film [20].

Fig. 1.5 (d) depicts the hybrid deposition which is a combination of the solution-based technique and vapor deposition. The inorganic precursor ($PbX_2$) is deposited by spin coating from solution followed by annealing. Then the organic precursor is deposited using physical vapor deposition [21].

In addition to the techniques discussed above, recently solid-solid interface reaction of two constituent salt films has been demonstrated for perovskite film synthesis. In this method two separately spin coated film of MAI and $PbI_2$ are brought into contact face to face as shown in the fig. 1.6. After annealing the precursors inter-diffuse and form MAPI by reaction [22].

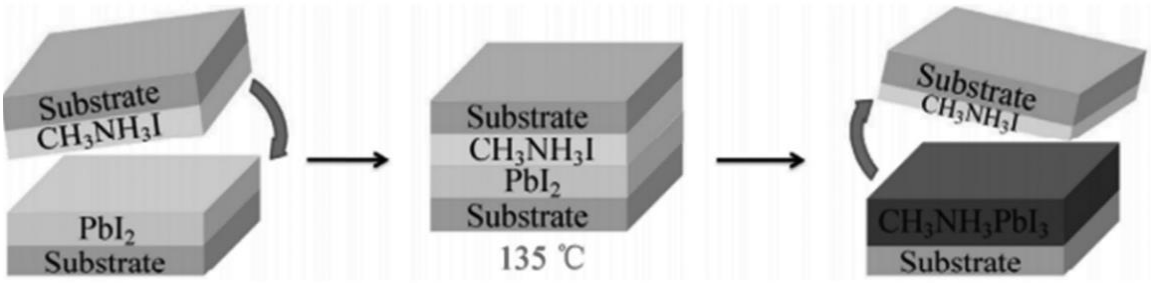


Fig. 1.6 Solid-solid interface reaction method of perovskite synthesis.

Vapor deposition offers some advantages over solution-based techniques at the expense of complexity and cost. Highly pure thin films can be grown from sublimation of

precursors in a vacuum chamber. The control of growth in solution-based processing is limited by the solubility of the precursors. Different precursors have different solubility. This limits the flexibility of film composition. Intercalation of solvents in perovskite films produces a stable unwanted perovskite-solvent intermediate (e.g. $CH_3NH_3PbI_3$.DMF, $CH_3NH_3PbI_3.H_2O$, and $CH_3NH_3PbI_3$.DMSO) which affects the stability of the film. Multiple layers of perovskite can be grown using vapor deposition. This is not feasible with solution processes due to the unavailability of orthogonal solvent pairs that can dissolve the precursors. Pinhole and partial coverage of the substrate attributed to wettability of the substrate can be overcome by solvent free vapor deposition [15].

At the expense of additional complexity and cost, high quality perovskite films can be synthesized using physical vapor deposition. One of the main reasons for the promise of perovskite thin films is its low-cost solution-based processing though. Despite the advantages of completely or partially vapor phase synthesis, our interest is focused on optimizing a solution-based one step deposition technique. Single step perovskite deposition techniques suffer from different problems. Many different approaches have been developed to overcome the problems. In chapter 3 a detailed literature review on the single step deposition technique is presented. Our approach to develop a scalable single step perovskite deposition technique is discussed.

## 1.5 Crystal growth and optimum growth parameters

Since part of this dissertation is about the development of a solution based scalable perovskite deposition process, it is very essential to discuss the crystal growth

mechanism from solution. Crystal growth form solution-based spin coating involves several mechanisms.

- Supersaturation of the solution
- Nucleation
- Diffusion
- Crystal growth

A solvent is called supersaturated when it contains more dissolved solute(s) than the solvent would normally be able to dissolve. Supersaturation is a metastable state of the solution and is the first step of crystal growth from the solution. The supersaturation state can be achieved in different ways including:

- Increasing the solution concentration by evaporating the solvent.
- Making the solution at relatively high temperature and then cool down.

In spin coating technique the solution becomes supersaturated due the evaporation of solvent during spinning. The crystal growth process is schematically represented with the simplified diagram in fig. 1.7 (a, b). After driving of the solvent, nucleation is the next step. In this step solid crystal nucleus are formed. Based on the nucleuses more and more materials are added to it make to make it bigger until it becomes stable. For a nucleus to be stable it needs to achieve a critical size and overcome the activation energy barrier. This energy barrier can be interpreted as the required additional energy to create the new liquid-solid interface of the solid in the liquid. The average number of nucleus that is formed per unit time per unit volume is called the nucleation rate [23]. The nucleation rate is an important parameter and determines the grain size of the thin film. If the nucleation rate is high grain size of the crystal will be small and the film’s roughness

will be small (fig. 1.7 c). On the other hand, a low nucleation rate results in bigger grain and the film will have a larger roughness. So, nucleation rate has a large impact on the film's morphology as shown in fig. 1.7 d. After the creation of the stable nucleus, the nuclei will grow and get bigger by incorporation of atoms or molecules from the solution. The process of moving the atoms or molecules from the solution to the nucleus is called diffusion. Crystal growth form a supersaturated solution essentially involves three processes: nucleation, diffusion and growth. The slowest process among these three controls the size and shape of the crystal grains.

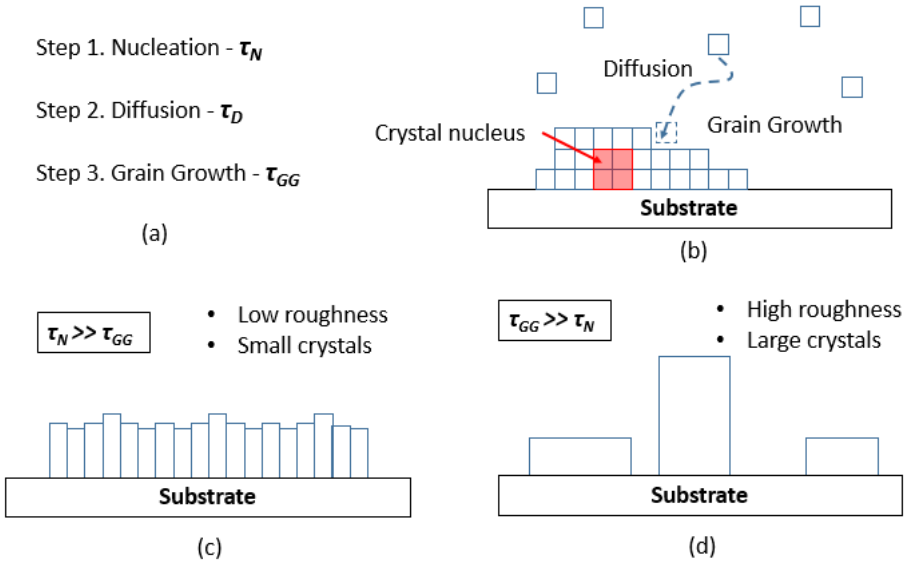


Fig. 1.7 (a) Crystal growth steps after supersaturation, (b) Schematic diagram of crystal growth process. Simplified qualitative diagram film morphology when (c) nucleation rate is higher and grain growth is slow (d) grain growth rate is high and nucleation rate is low.

Solution based perovskite which assume the chemical formula $ABX_3$ is typically obtained by the reaction between an organic salt namely methylammonium salt (AX) and

a lead salt ($BX_2$) where X is I, Br or Cl. In conventional material deposition and growth techniques either seed crystals are used or the substrate itself works as a seed to obtain the desired crystallographic orientation. The deposition of the perovskite form solution of precursors is a completely different case technically. In this case three different species of ions with different size, reactivity stay together in a solvent. To obtain ideal crystals the constituents of perovskite need to react maintaining desired stoichiometry. Since the substrate is a foreign material for the $ABX_3$ perovskite structure, it does not contribute for the initiation of crystallization. Moreover, spin coating is a very fast process which makes the control of the growth aspects, including nucleation rate, diffusion and growth rate difficult. To date there is no established model for solution based thin film growth by spin coating. To achieve control over perovskite crystal growth for better quality we introduce an additive in the precursor. Introduction of the additive slow down the overall crystallization process by forming an intermediate phase. Finally, we need to make sure of the removal of all solvents, additives and byproducts after the depositing the film. In chapter three we present the detail of tailoring the nucleation and grain growth by changing precursor ratio.

## 1.6 Perovskite devices and device architecture

Three types of devices are realized using perovskite thin films: solar cells, light emitting diodes and transistors. Lasing action and photodetectors with perovskite material have been demonstrated.[5] A description and dissection of the archetypical structures of the implemented and proposed perovskite devices are shown below. Unlike conventional optoelectronic devices, perovskite solar cells and light emitting diodes are not p-n junctions. Fig. 1.8 (a) represents the typical device architecture of a perovskite

solar cell or a LED. Both type of devices have an active layer of un-doped perovskite sandwiched between an electron and a hole transport layer. The carrier transport layer can be deposited in any order with respect to the substrate. Two electrodes are required for external contact on two sides of the sandwich. The perovskite layer acts as absorber for the solar cell and emitter for the LED. [5], [24]

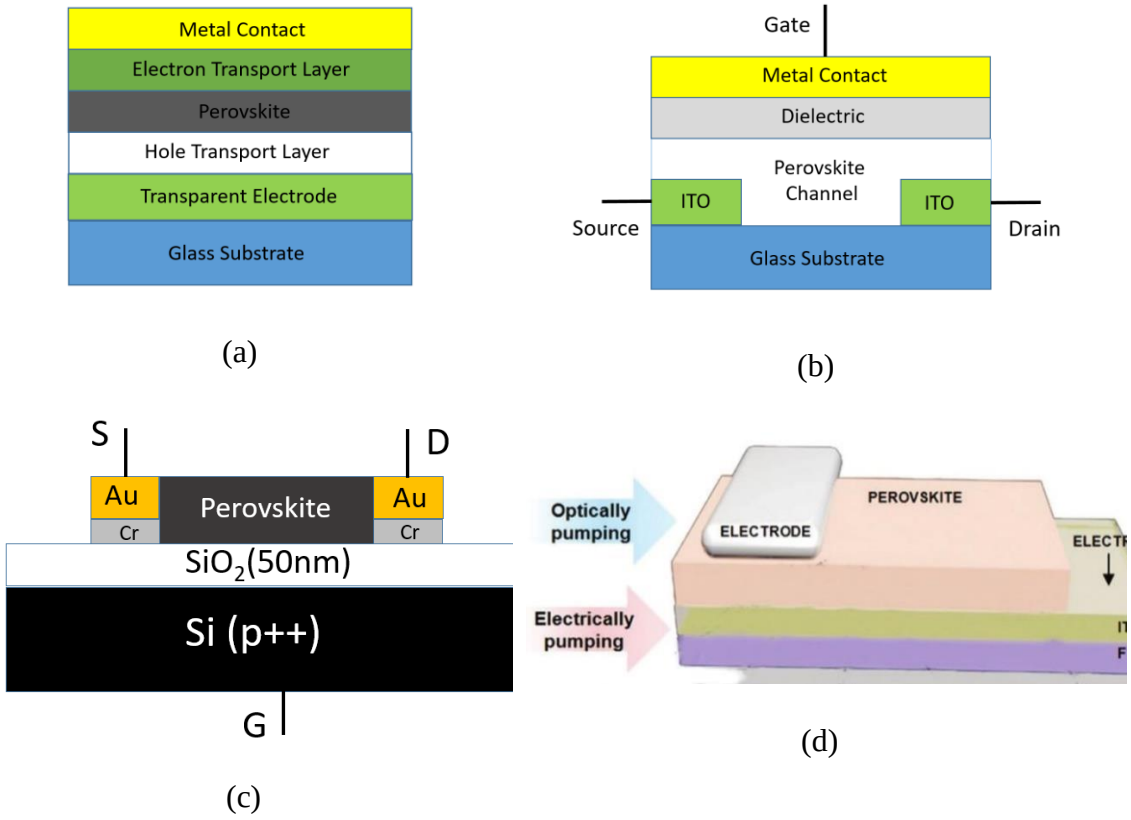


Fig. 1.8 Typical device architecture of perovskite (a) solar cell and LED (b) Field effect transistor (c) laser (concept) [5].

Based on the nature of the substrate on which the device is fabricated, the perovskite solar cell can be classified as [25]:

- A mesoporous scaffold perovskite solar cell or
- A planar heterostructure perovskite solar cell.

Based on the orientation of carrier transport layer with the active perovskite layer the above-mentioned solar cell structures can be subcategorized as:

- p-i-n structure
- n-i-p structure

Figure 1.8. (b) and (c) shows a typical top gate and bottom gate field effect transistor structure respectively. In a typical thin film transistor (TFT) or field effect transistor (FET), two electrodes (source and drain) are connected through a semiconducting channel. Carrier conduction is controlled by another electrode named the gate, which is separated from the channel by a thin sheet of dielectric material. Unlike the solar cell and LED, the TFT structure has two *'metal/perovskite'* contacts and a '*metal/dielectric/perovskite*' contact for all possible architectures of the TFT. Instead of metal, the conductive electrode can be a highly doped semiconductor or transparent conductive oxide (Indium tin oxide).

Fig. 1.8. (d) shows the schema of the perovskite laser which is in concept stage. This structure also contains metal/perovskite interfaces.

## 1.7 Organization of the thesis

This chapter presented a general introduction of perovskite materials, deposition method, devices made of perovskite. We also discussed the problem with the existing depositions techniques towards scaling up of the thin film devices. Then the issues of perovskite device transport mechanism which need further attention of the researchers were introduced. We presented research questions and scope this dissertation would cover to find the answers of the question.

In the second chapter, we will briefly introduce the major characterization tools and techniques used in this research. The instruments include imaging tools, optical characterization tools, electrical characterization tools and finally electrochemical techniques.

Chapter three is focused on the development of a single sept additive assisted scalable perovskite deposition technique. It contains a detailed background literature study of the single step perovskite deposition technique.

In chapter four, the performance of perovskite solar cell and light emitting diode using the newly developed deposition technique are evaluated. The performance optimization through different layers and interfaces are also reported.

Chapter five deals with a temperature and light intensity dependent study of the optimized solar cell. The interface of the devices where loss mechanism takes place are identified and investigated.

Chapter six presents the development of orthogonal electrolyte and electrochemical toolkit for the perovskite characterization.

Finally, chapter seven draws the conclusion of the dissertation and proposes some suggestions for future potential research.

# 2. CHARACTERIZATION TECHNIQUES

## 2.1 Introduction

On the way to perovskite thin films and perovskite device optimization, many different characterization techniques have been employed at different steps of the research. These techniques include imaging, structural and crystallographic, electrical and optical measurements. This chapter is dedicated for a brief overview of the characterization techniques. Moreover, the necessary technical specifications of the tools used in the research are provided.

## 2.2 Morphological and Structural characterizations

Surface morphology and crystalline structure are the two most important materials properties to be studied. Scanning electron microscopy (SEM) with embedded energy dispersive spectroscopy (EDS), atomic force microscopy (AFM) and surface profilometry were used for the morphology study. For the structural investigation, an X-ray diffractometer (XRD) was used. The following sections present the working principle and technical specifications of the tools mentioned above.

### 2.2.1 SEM and EDS

Scanning electron microscope (SEM) is capable of imaging the surface morphology with a nanometer scale resolution. The operating principle of SEM is analogous to an optical microscope. A SEM system consists of an electron gun, condenser lenses, scanning coil, objective lenses, detector and a display unit [26]. The components are organized as shown in the fig. 2.1 (a).

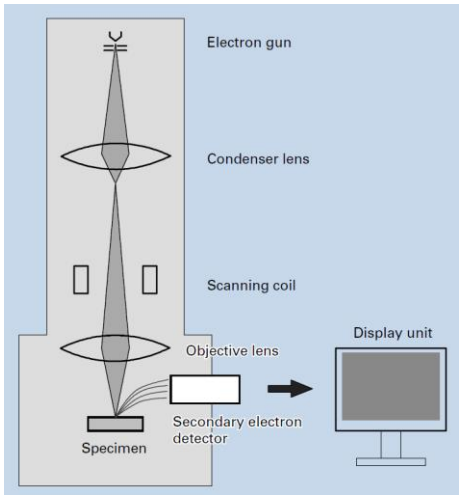


(a)

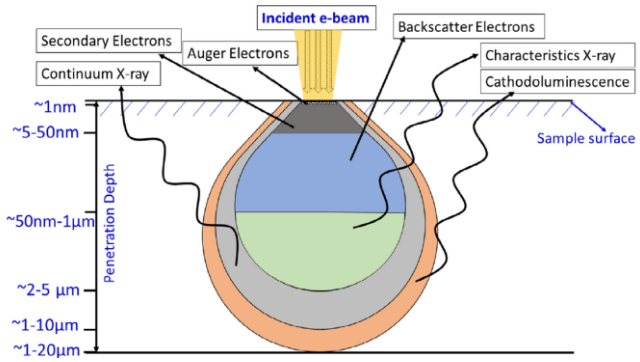


(b)

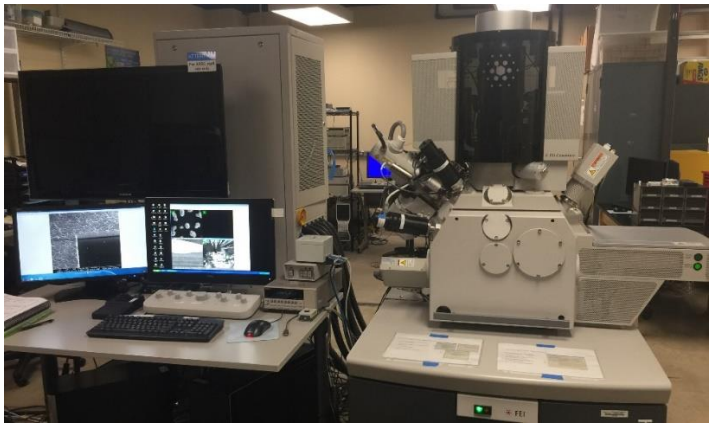

(c)

Fig. 2.1 (a) Schematic diagram of a scanning electron microscope [26] (b) Different type of signal generated from the irradiated spot of the sample along with corresponding depth from the surface [27], (c) FEI Helios NanoLab 400 DualBeam field emission scanning electron microscope of Texas State University.

Both electron gun and the sample are required to be in a high vacuum chamber. The electron gun can be thermionic or field emission type. Images of the samples are obtained by scanning the surface using a finely focused beam of electrons. Based on the type of sample, secondary electrons, backscattered electrons, Auger electrons, light, and

X-rays or combination thereof may be released (fig. 2.1 b). The state-of-the-art system has separate detectors for capturing the individual signals. The signals are collected and processed by a computer to generate the image and other valuable information about the sample [27]. To image the topography of the perovskite, the secondary electrons signal is used.

For this research, a FEI Helios NanoLab 400 DualBeam field emission scanning electron microscope of Texas State University was used. The electric potential of the incident energy beam of the system can be varied between 350V – 30kV. This system contains a focused ion beam (FIB) and has also energy dispersive spectroscopy (EDS) capabilities. FIB system uses heavy Gallium ions to sputter off material of the sample. This is useful to make cross-sections of the thin film and used for cross-sectional imaging. The EDS system is used to identify the elements from the characteristics X-ray released from the sample after its atoms are excited by the incident electron beam. SEM imaging of the perovskite surface is challenging as the grains start to separate when a high energy electron beam hits the surface. It requires a suitable selection of voltage and beam current to obtain high-quality image. Detailed information on imaging of perovskite thin films including top view and cross-sectional imaging are presented in section 3.3.3 of chapter 3.

### 2.2.2 X-Ray diffraction (XRD) and XRD pole figure

XRD is a powerful technique to investigate the crystallographic properties of materials. It is a nondestructive technique that can be performed in a normal atmosphere without any special sample preparation. X-ray diffractometry also can be done in a special environment such as, at elevated temperature or high pressure with special

arrangement. This technique is used for studying lattice constants, crystal structure, crystal orientations, preferred orientations including orientation distributions, strain, crystal defects, grain size, film thickness, and film density.[28]

Crystals contain a regular array of atoms. The spacings between the atomic planes are comparable with the X-ray wavelength. Therefore, a crystalline material can be considered as a three-dimensional diffraction grating for X-rays. When X-rays are incident at a certain angle on a crystalline sample, it interacts with the material and the X-ray beam is diffracted as illustrated in the Fig. 2.2 a. Based on the atomic spacing between the planes, angle of incidence and wavelength of the incident X-rays, the interference between the diffracted X-ray beam may be constructive or destructive. Constructive interference occurs when the parameters satisfy the Bragg's condition (equation 2.1).

$$n\lambda = 2d\ sin\theta \qquad (2.1)$$

Here, $n$ is an integer, $d$ is the atomic spacing, $\lambda$ is the wavelength of X-ray and $\theta$ is the diffraction angle. In a θ/2θ measurement, the X-ray beam incident on the sample at an angle θ and the detector collects the diffracted X-rays at an angle 2θ. Typically, the angle is varied from $5^o$ to $80^o$, and the detector collects the diffracted X-rays. Peaks are observed for certain positions of 2θ in an X-ray count versus 2θ plot, from which crystallographic information are extracted.

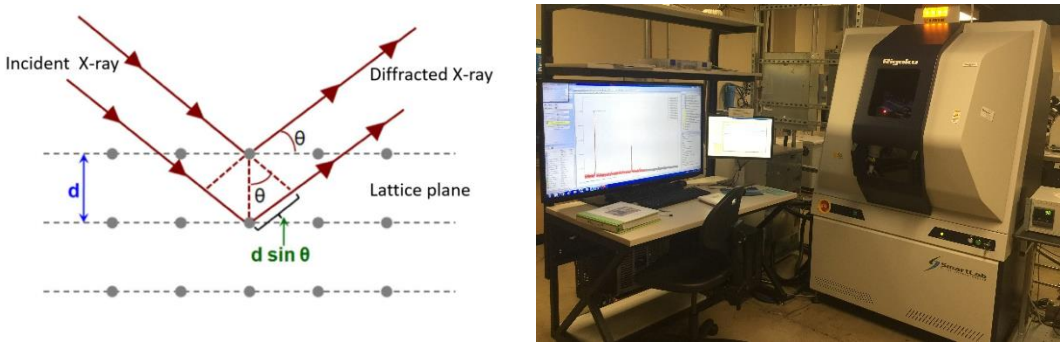


(a) (b)

Fig. 2.2 (a) Diffraction of X-ray at crystal planes (b) Rigaku SmartLab diffractometer of Texas State University

For this research, a Rigaku SmartLab diffractometer was used. The components of the system are an X-ray tube, an X-ray detector, a goniometer, an incident optical system, and a receiving optical system. This equipment has a high power 9kW copper rotating anode X-ray generator. The SmartLab diffractometer is a 5-axis tool. The position of the sample can be manipulated with a rotation stage and two goniometers and the detector can be moved along two circles as shown in the fig. 2.3 [29]. θ/2θ measurements can detect the plane parallel to the sample surface. Typically, a θ/2θ scan is performed for identification of phase and crystal structure. The inclined or perpendicular planes remain undetected. Especially, for single crystal system probability of undetected thin film planes are higher. The material of interest in this research (MAPI) is polycrystalline. Therefore, the planes of the crystals are oriented in different angles from the surface normal. In order to get the idea about the distribution of the crystal orientation of a polycrystalline film researchers often do pole figure measurements. A pole figure study is an appropriate choice to identify the preferred orientation and distribution of the planes from the surface normal

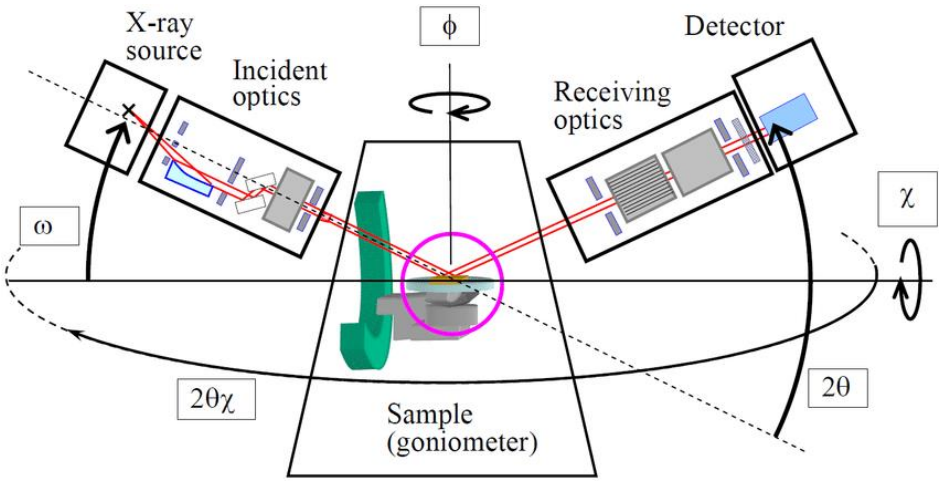


Fig. 2.3 Schematic diagram of Rigaku SmartLab diffractometer [30].

In pole figure measurements, detector is set to a fixed diffraction angle (2θ), where an X-ray peak is observed for the sample under investigation. The X-ray count is recorded for different tilt angles of the sample with respect to the diffraction vector. The angle between the surface normal and the diffraction vector is denoted by α, which is varied from 0° to 90° for pole figure measurement. For each tilt position, the sample is allowed to rotate 360°. This rotation angle is denoted by β. The intensity profile recorded in terms of α and β is referred to as a pole figure. This data can be presented both as a 3D plot of intensity distribution and plane of stereographic projection with polar coordinate α and β.

Both θ/2θ and pole figure measurement of perovskite were done for crystallography study. Perovskite changes phase between room temperature and 100ºC. To observe the phase change and identify the transition temperature XRD measurement were also done at elevated temperature.

### 2.2.3 Atomic force microscopy (AFM)

Atomic force microscopy (AFM) is a type of scanning probe microscopy (SPM). Unlike optical microscopy or SEM, in this case, a solid probe scan over the sample surface. The physical probe enables the imaging of non-conducting surface without prior sample preparation. The basic block diagram of an AFM system is shown in fig. 2.4. (a). It consists of a cantilever which has a nanometer scale sharp tip at the free end. The cantilever is mounted on a cylindrical 2D piezoelectric raster scanner. This tip scan over the sample surface when a voltage is applied to the X and Y electrode of the piezoelectric tube. When the tip comes to close proximity of the sample surface, a force of attraction or repulsion acts on the tip depending on the distance between surfaces and tip (see fig. 2.4. b). This force causes to deflect or bend of the cantilever. The deflection of the cantilever is detected using a reflected laser from cantilever head to a position sensitive photodiode. There are two imaging modes: contact mode and tapping mode. In contact mode, the tip is brought into contact with the sample surface. In contrast, the tip is brought in close proximity of the surface in tapping mode. The tip vibrates at a certain frequency.

A computer processor computes the photodiode signals and translates into useful data of the sample, e.g. surface topography.

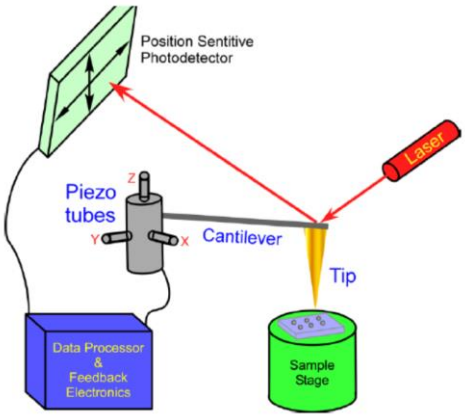


(a)

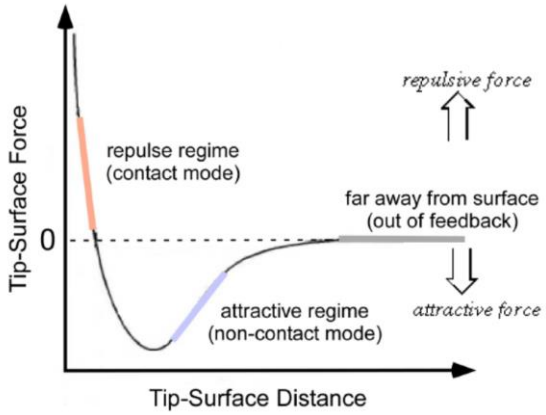


(b)

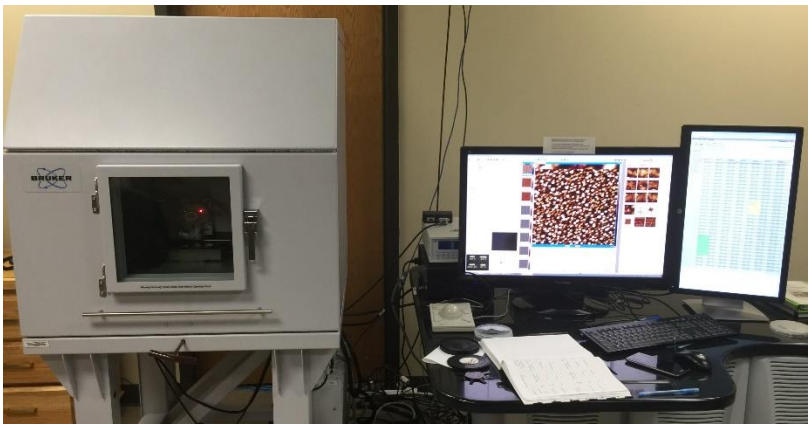

(c)

Fig. 2.4 (a) The basic building block of an AFM system, (b) Tip-surface force versus tip-surface distance plot, (c) Bruker dimension Icon Scanning Probe Microscope of Texas State University.

A Dimension Icon Scanning Probe Microscopy (fig. 2.4. c) was used in this research to determine the surface topography and the roughness of the samples.

### 2.2.4 Surface profilometry

A surface profilometer can be thought of as a simple version of an AFM. In this technique, a tiny stylus is dragged over the specimen surface to generate the profile of the surface based on the X, Y and Z coordinate of the stylus. In this research, this method is frequently used for quick thickness measurement of the thin films. For thickness measurement, a step or trance of the film to be measured is required. A set of fine scratches of the thin film were made on the substrate. Inherent softness of perovskite helps to make scratch without damaging the substrate. While this a simple technique, the accuracy is compromised by the radius of the stylus. The Bruker DektakXT profilometer was used in this work. The radius of the stylus tip was 2µm. The tip force on the measurements during the scans was 3mg and the length of the measurements was varied between 800 and 1200µm. Figure 2.5 shows the image of a scratched sample for profilometry and the surface scan profile.

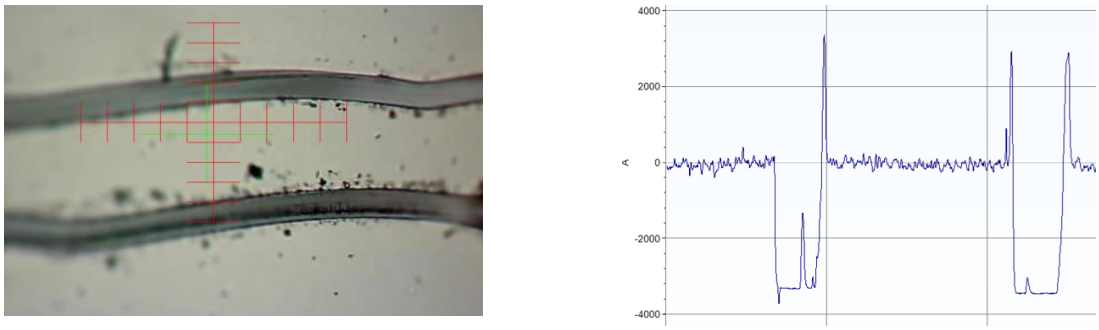


(a) (b)

Fig. 2.5 (a) Trances on the film, (b) Corresponding stylus profile.

## 2.3 Electrical and Transport

Perovskite solar cells and LEDs were fabricated and studied in this research. The performance of the devices was investigated by current-voltage (I-V) measurements. As

the performance of the solar cell depend on the intensity of exposed light and temperature, a special type of tool was used to do the temperature and light dependent study. The sections to follow present the description of the tools used for regular I-V measurement and temperature and light intensity dependent I-V measurements.

### 2.3.1 Current-voltage

To determine the solar cell's efficiency the current-voltage (I-V) characteristics have to be measured under solar illumination. An Oriel ABA sun simulator with an AM 1.5G filter which is calibrated to provide 100mW/cm$^2$ to the sample. A Keithley 2400 SourceMeter was used to measure I versus V. The whole setup is shown in the fig. 2.6. The samples were connected to the source meter through a custom-made 3D printed holder (shown in the inset of the of fig. 2.6). The measurements parameters were controlled via a LabView program which also took care of the data acquisition. The typical operating voltage ranged from -0.2V to 1.2V. After every measurement the LabView program return the value of device efficiency, open circuit voltage (Voc), short circuit current (Isc) and fill factor along with an array containing the measured I and V values.

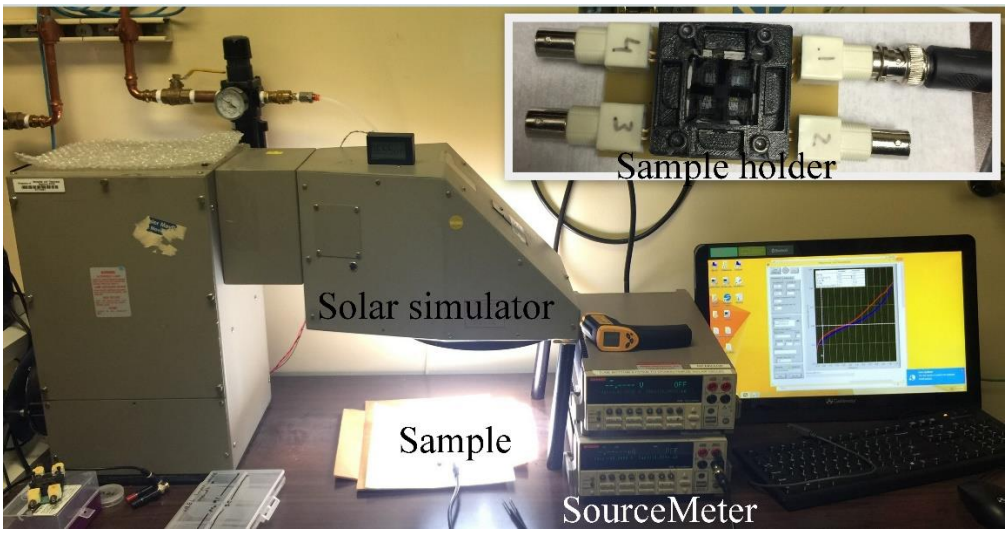


Fig. 2.6 Solar simulator used for the current research, top right inset showing the 3D printed solar cell holder.

### 2.3.2 Temperature dependent Current-Voltage

Illumination intensity and temperature dependent characterization of perovskite solar cells were performed using an ARS cryogenic probe station. The capability of this probe station includes temperature and light intensity dependent current-voltage (J-V), capacitance-voltage (C-V), admittance spectroscopy, and drive level capacitance profiling (DLCP) measurements. This tool is an integrated form of the following components: a light source, a chiller, a vacuum pump, optical filters, a probe station, a sample holder, a source meter, a temperature controller, an impedance analyzer and a microscope. The whole system is operated for measurement using a customized a LabView program. Fig. 2.7 shows the image of the cryogenic probe station of Texas State University.

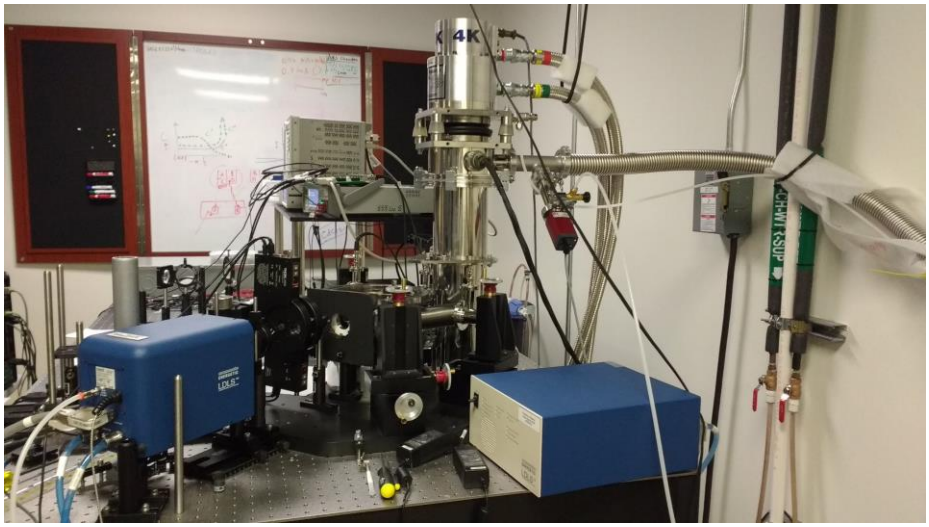

Fig. 2.7 ARS cryogenic probe station of Texas State University.

In this research, temperature and excitation-dependent open-circuit voltage, short circuit current measurement were performed inside the helium closed cycle cryogenic system using a Keysight B2912A source measure unit. This system operating temperature can be varied from 8K to 800K. The PV devices reported on this thesis were characterized over a temperature interval 40 – 430K. The illumination intensity of the light was varied from $1\times10^{-3}$ to 56.6 mW/cm$^2$. The intensity of light was controlled by neutral density filters.

## 2.4 Optical

Mainly two types of optical characterization techniques were employed in this research. UV-Vis spectroscopy was used to determine the absorbance of the thin films used in the devices. Ellipsometry was used for the determination of the optical constants and thickness measurement.

### 2.4.1 UV-Vis Spectroscopy

Ultraviolet and visible (in brief UV-Vis) spectroscopy is an optical characterization technique to quantify the light material interaction when a material is exposed to a light of a specified wavelength range. It can measure the absorbance, transmittance, and reflectance of thin films compared with a reference (if any). In this work, a Shimadzu UV-2501(PC) instrument was used. The wavelength range of the light source was 200 – 900nm. Fig. 2.8 shows the schematic diagram of a conventional UV-Vis spectroscope. It consists of a light source, a monochromator, a sample holder, a detector and a signal processor used for data analysis. The purpose of the monochromator is to select wavelengths during measurements.

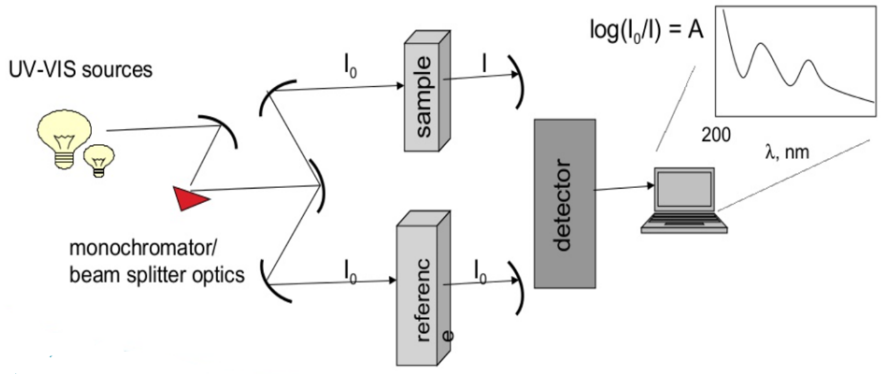


Fig. 2.8 Schematic diagram of a UV-Vis spectroscopy system.

UV-Vis spectroscopy can be used for a wide variety of applications. In the current research, this technique was mainly used for absorption measurement of the perovskite solar cell constituent layers. Thin films were grown on glass substrates. The clean glass substrate was used as the reference. The thin film absorbs light if the energy difference between the occupied and unoccupied electronic states of the film is lower or equal to the

energy of photons. The thin film is exposed over the entire wavelength range from 200-900nm. The system measures the intensity of the light that passes through the sample and compares it with the intensity through the reference sample. Finally, it outputs the data of absorbance as a function of wavelength. From the absorbance data, absorption centers (position of the absorption peaks), the bandgap of the thin film can be extracted.

### 2.4.2 Ellipsometry

Spectroscopic ellipsometry is a non-destructive optical technique for thin film characterization. It is widely used for estimating the optical properties and thickness of thin films. Besides, film roughness, material composition, crystallinity, doping concentration can be derived from ellipsometry data. The essential components of an ellipsometer are a light source, a polarization generator, a sample stage, a polarization analyzer, and a detector. The components are organized as shown in fig. 2.9 (a).

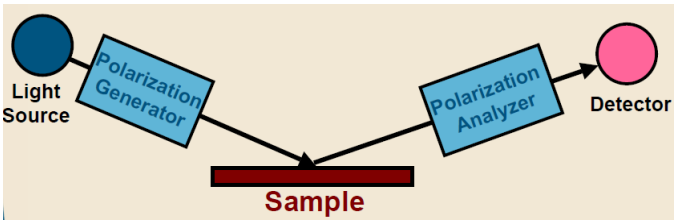


(a)

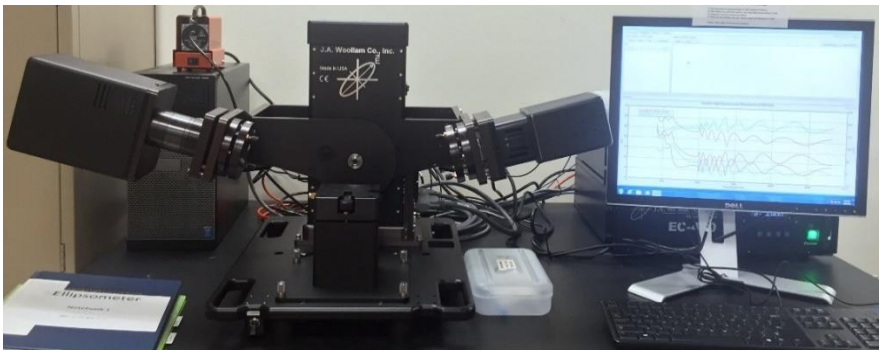

(b)

Fig. 2.9 (a) Basic building block of an ellipsometer (b) J. A. Wollam M2000 ellipsometer of Texas State University.

The principle of Ellipsometer operation is, it measures the changes in polarization upon reflection with the sample under investigation. Polarized light incident on a specimen undergoes a change in polarization depending on the optical properties and thickness of the thin film(s). This change is detected, quantified and expressed in terms of amplitude component Psi (Ψ) and phase difference Delta (Δ). These two parameters are related according to following the equation 2.2.

$$\tan(\Psi).\ e^{i\Delta} = \rho = \frac{r_p}{r_s} \qquad (2.2)$$

Here $\rho$ is the ratio of the reflectivity of p-polarized $(r_p)$ and s-polarized $(r_s)$ light.

The optical constants $n$ and $k$ can be derived from the following equation 2.3.

$$\langle \varepsilon \rangle = \langle \varepsilon_1 \rangle + i\langle \varepsilon_2 \rangle = \langle \tilde{n} \rangle^2 = (\langle n \rangle + i\langle k \rangle)^2 = \sin(\Phi)^2 . \left[ 1 + \tan(\Phi)^2 . \left( \frac{1-\rho}{1+\rho} \right)^2 \right] \quad (2.3)$$

The optical properties of MAPI, PEDOT:PSS and ITO were investigated using this tool. The J. A. Wollam M2000 ellipsometer was used for collecting the Ellipsometry data. CompleteEASE software was used for data analysis and modeling. Optical constants of thin films were extracted from the ellipsometry data. Then using the optical constants, models were built to measure the thickness of the thin films. The flow chart of the data analysis and modeling is represented in fig. 2.10.

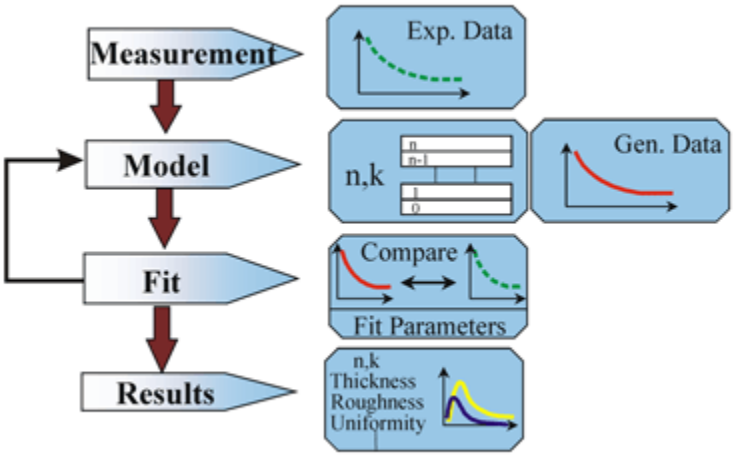


Fig. 2.10 Measurement and analysis flow chart of spectroscopic ellipsometry [31].

To quantify the accuracy of the model, a parameter named means square error (MSE) is used defined by the following equation 2.4.

$$MSE = \sqrt{\frac{1}{3m-l} \sum_{i=1}^{m} [(N_{Ei} - N_{Gi})^2 + (C_{Ei} - C_{Gi})^2 + (S_{Ei} - S_{Gi})^2]} \times 1000 \quad (2.4)$$

Here, $m$ is the number of wavelengths measured, $l$ is the number of fit parameters, $N = \cos(2\Psi)$, $C = \sin(2\Psi)\cos(\Delta)$, $S = \sin(2\Psi)\sin(\Delta)$. The reasonably small value of

MSE indicates the level of accuracy of the model. The Levenberg-Marquardt nonlinear regression algorithm is used to minimize the MSE of the fitting process.

## 2.5 Electrochemical: Cyclic-voltammetry

Cyclic voltammetry is a special type of I-V characterization method which involves an electrochemical cell with three electrodes. The three electrodes are referred to as working (WE), counter (CE), and reference (RE) electrode. A simplified circuit representation of a cyclic voltammetry system is shown in fig. 2.11 (a). All electrodes are submerged in an electrolyte solution.

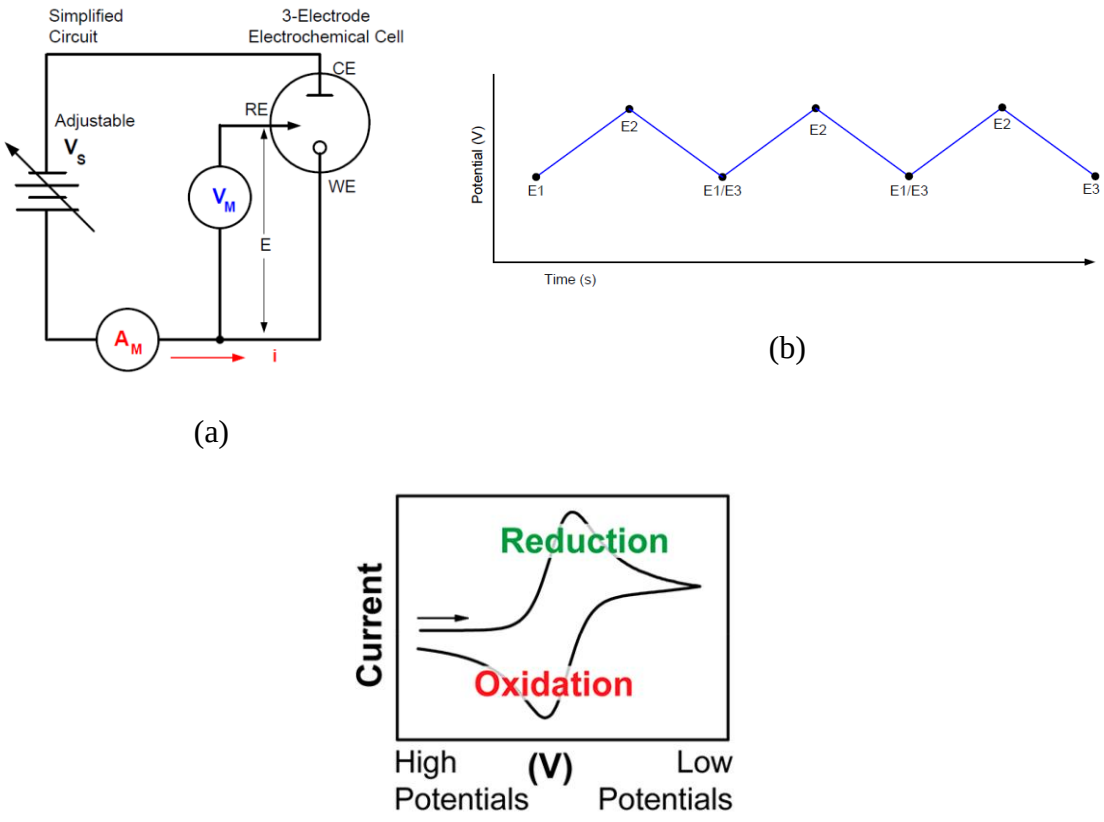


(a) (b) (c)

Fig. 2.11 (a) Simplified circuit representation of a cyclic voltammetry system [32], (b) Cyclic voltammetry waveform (3 cycles) [32] (c) A typical voltammogram.

This method is utilized for studying reactions involving electron transfers. In addition it provides information on the electron transfer kinetics and the reversibility of the reaction [33]. A variable voltage source is connected across the working electrode and the counter electrode. The applied voltage is swept over a range, and the scan is reversed (fig. 2.11.b). When the applied voltage is sufficiently high, electrolysis takes place. In this process, electrons are exchanged between the electrode and the electrolyte. The loss and gain of electron are known as oxidation and reduction respectively. For two arbitrary materials '*A*' and '*B*', the oxidation and the reduction processes can be represented by the following equations.

$$Oxidation: \ A = A^{+} + electron$$

$$Reduction: \ B + electron = B^{-}$$

The electric potential difference between RE and WE, and the current flowing in WE are recorded (see Fig. 2.11). This plot is called a voltammogram. Current peaks associated with the oxidation and reduction reaction are observed in the voltammogram as shown in fig. 2.11 (c). The oxidation and reduction reactions are related to ionization potential (IP) and electron affinity (EA). According to the Koopmans theorem, IP and EA are linked to the highest occupied molecular orbital (HOMO) and lowest unoccupied molecular orbital (LUMO) as following [34]:

$$IP = -E_{HOMO} \qquad (2.5)$$

$$EA = -E_{LUMO} \qquad (2.6)$$

Electronic and transport properties can be extracted from the peak positions and the onset of the reactions using the above relations. For instance, the HOMO level of the thin film can be calculated from the following equation:

$$E_{HOMO} = -e\,(E_{ox}^{onset} + E_{Electrode}) \qquad (2.7)$$

The whole scan can be repeated for many cycles to test the reversibility of the reaction.

# 3. PEROVSKITE FILM PROCESSING OPTIMIZATION

Note: Most of the contents from this chapter was published in the *Journal of Material Chemistry C* on 15 September 2017 by the author of this thesis along with other co-authors of the same research group. DOI number of the publication is 10.1039/C7TC02928D. The contents taken from the published article were cited where applicable.

## 3.1 Introduction/literature review

As of May 2019, the best certified perovskite solar cell (research) efficiency reached 24.2%[3]. Cell efficiencies reported over 20% were of the small area, fabricated in lab scale. To the best of our knowledge, the largest MAPI single solar cell was 25 $cm^2$ and had an efficiency of 6.8% [35]. Decrease of efficiency for larger devices largely attributes to the inability to scale up the deposition of high quality and homogeneous perovskite films. Commercialization is the final goal to take advantage of any promising technology. To transform the highly potential perovskite solar cells from lab scale to industrial scale dimensions, some key issues need to be addressed. First, a scalable and less expensive deposition technique need to be developed for high-quality perovskite. Second, the operational stability needs to be improved. Third, one need to control the toxicity of the materials. While a large worldwide research effort is focused to address all these issues, the motivation of this research is to develop a scalable deposition technique. As discussed in section 1.2, perovskite materials, which assume the chemical formula $MAPbX_3$ are typically obtained by the reaction between organic salt namely methylammonium salts (MAX) and lead salts ($PbX_2$) where X is I, Br

or Cl. Methylammonium lead iodide ($CH_3NH_3PbI_3$) appears to be one of the most successful and highly studied perovskites. To remind the readers again, instead of complex chemical formula $CH_3NH_3PbI_3$ or the long name, 'MAPI' has been used for 'methylammonium lead iodide' throughout the thesis. The reaction involved in the $CH_3NH_3PbI_3$ synthesis is

$$CH_3NH_3I + PbI_2 \rightarrow CH_3NH_3PbI_3$$

The broad categories of perovskite deposition techniques were discussed in the first chapter (section 1.4). Briefly, the techniques are solution based and fully or partially vapor based. There are many versions of solution-based techniques. Among all the techniques single step solution-based spin coating is the simplest one. The chemical reaction of $CH_3NH_3PbI_3$ formation from the precursors suggests that the stoichiometric ratio 1:1 of $CH_3NH_3I$ and $PbI_2$. Solution based spin coating is a very fast growth technique. Unlike vapor phase growth, it is very challenging to impose external control over the reaction in molecular scale to ensure the homogeneity and uniformity of the reaction. Due to the rapid reaction kinetics, often the resulting morphology of the films coated from a mixture of two salts is rough and not appropriate for thin film devices. Incomplete coverage and the presence of pinholes create a shunt path which causes degradation of device performance. To overcome this issue, researchers have either used an approach of intermediates using lead halide adducts or a sequential coating approach where each salt is deposited separately [36],[37]. While both approaches have resulted in spectacular device performances, these methods are not ideal for large scale coating due to several reasons. The single step intermediate phase approach

requires the films to be washed with an orthogonal solvent or a gas flush before thermal annealing [38]. The orthogonal solvent washing leads to quenching of a lead halide solvent adduct, which forms a uniform film and upon annealing induces a phase transformation which gives rise to desired smooth film morphology and coverage. While this is easily achieved on smaller scale substrates with spin coating methods, it poses severe challenges for larger scale coating methods such as roll to roll or slot die coating. On the other hand, two-step approaches need meticulous and careful optimization as conditions for both steps are interdependent. Ideally, for the roll to roll coating, a single solvent with low viscosity is needed with minimal post-processing steps to enable cost-effectiveness and high throughput [39]. To achieve a simple and scalable coating, perovskites derived from non-halogenated lead source namely, lead acetate ($Pb(Ac)_2$) shown to be effective. Perovskites films coated with $Pb(Ac)_2$ possess a uniform coverage and smooth morphology nullifying the requirement for any additional quenching process [40]–[42]. In spite of the advantages of smooth film formation, coverage, and quick conversion, the grain growth from $Pb(Ac)_2$ has shown to be the limiting factor for efficient photovoltaic devices. The reason is the nucleation and grain growth of the MAPI from the $Pb(Ac)_2$ precursor occurs very fast and at low annealing temperatures which lead to smaller grains and defective interfaces [43]. Often researchers have used alternative methods such as the inclusion of additives [44], lead chloride [45], ambient exposure, Ostwald ripening [46] and solvent annealing [47] to enhance grain size and lower defects. Notably, it has been shown that nucleation of the perovskite phase can be achieved by exposing the as-

deposited $Pb(Ac)_2$:MAI films before thermal annealing [48]. Such an ambient exposure leads to a substantial reduction in trap densities and charge transport barriers, thereby eventually enhancing the photovoltaic performance. Similarly, a study by Dubey et al. shows that solvent quenched intermediate films exposed to ambient air led to slow conversion of the intermediate phase to perovskite phase [49]. This slow conversion in ambient led to the ideal morphology of the perovskite films possessing improved optical and charge transport properties compared to films annealed in nitrogen. Highlighting the significance of nucleation, Grätzel, and coworkers obtained a power conversion efficiency above 21% by utilizing poly(methyl methacrylate) (PMMA) templated growth of the perovskite solar cells [50].

It is critical to understand the compositional induced perovskite nucleation and grain growth mechanism to realize optimal ink formulations and enabling quick conversion to high-quality perovskites. Such insight will be of importance for scaling up for large area and roll to roll coating technologies.

In this chapter, the role of MAAc additive with methylammonium salt (MAX) and lead salt ($PbX_2$) on solution-based spin casted perovskite thin film is presented. The optimum perovskite processing parameters were determined for device fabrication.

## 3.2 Experimental

The first goal of thin film synthesis process optimization is to determine the optimum ratio of the precursors. As the reaction suggests, the ideal ratio of $PbI_2$ and MAI for $MAPbI_3$ thin film synthesis is 1:1. Therefore, only the additive MAAc ratio was

varied from 0.5 to 2. The films synthesized using different ratio of MAAc were characterized using imaging, optical, and structural analysis tools. At the very beginning of the research, methylammonium acetate (MAAc) was not commercially available. That is why MAAc was synthesized in the lab using a custom build chemical setup. At some point later, MAAc was available from commercial vendors. The section to follow described the method of MAAc synthesis in the Organic Semiconductor Device lab of Texas State University.

### 3.2.1 Synthesis of Methylammonium Acetate (MAAc)

Methylammonium acetate (MAAc) was synthesized by reacting anhydrous methylammonium (MA) gas with acetic acid and quenching the salt in toluene. The setup of MAAc synthesis is pictured in the fig. 3.1. In this setup, two chemical flasks were connected through a column using flexible pipes. Both flasks were placed on individual magnetic stirrer with stir bar inside the flasks. The chemical column that bridged between two flasks was filled with NaOH. The left and right flasks are partially filled with MA solution and toluene with glacial acetic acid, respectively. MA gas is evolved when NaOH is added to an aqueous solution of MA. Then the MA gas is passed through NaOH column into the flask containing glacial acetic acid in toluene. MA reacts with acetic acid, and MAAc is produced. The full consumption of acetic acid in the reaction was confirmed by a pH test of right flask content. Once saturated, MAAc precipitates in the toluene. Then the salt is decanted and dried in vacuum overnight and stored in $N_2$ for further use.

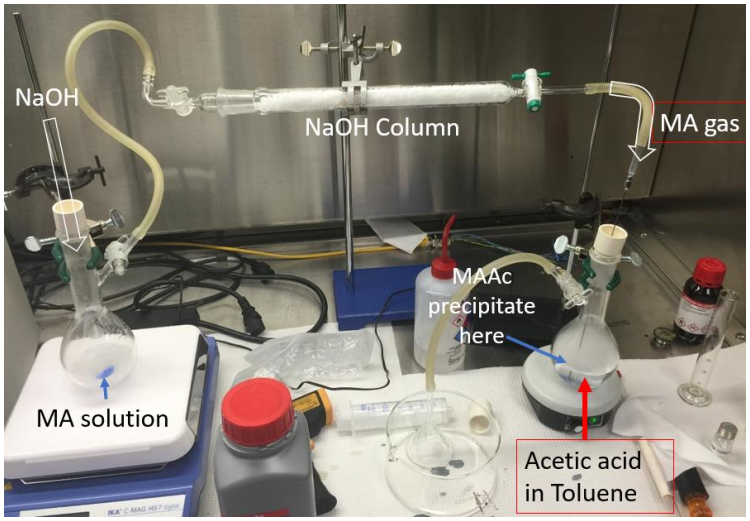


Fig. 3.1 Chemical setup for MAAc synthesis.

### 3.2.2 Preparation of Perovskite Thin Film

$PbI_2$ (Sigma Aldrich), MAAc (of Texas State University lab) and MAI (Lumtec) were mixed in different molar ratios (1:2:1, 1:1:1 and 1:0.5:1) in DMF (1M). 1:2:1 and 1:1:1 precursor solutions ratios were also achieved by mixing $Pb(Ac)_2$, $PbI_2$ and MAI when mixed in 1:0:3 and 0.5:0.5:2 molar ratios in DMF respectively. The solutions were filtered with 1µm PTFE filter before coating. The solutions were prepared inside the glove box. Thin films were deposited by the spin coating method. After coating the films were annealed at 100$^{o}$C for 5 min in a different humidity-controlled chamber at 30 – 35% RH.

## 3.3 Film characterization

### 3.3.1 UV-Visible spectroscopy and optical imaging of the films

UV-Visible absorption spectra were performed using a Shimadzu UV-2501 spectrophotometer. Absorption spectra of the films were collected from 900 nm to 200 nm. Fig. 3.2a shows the photographs of the as-casted films derived from different precursor ratios of $PbI_2$:MAAc:MAI. The films with 1:2:1

$PbI_2$:MAAc:MAI possessed a yellow color as observed for films coated from 1:3 molar ratio of $Pb(Ac)_2$:MAI which is the conventional mixing ratio for perovskite derived from $Pb(Ac)_2$ based precursor. Similarly, 1:1:1 $PbI_2$:MAAc:MAI precursors can be formulated from 0.5:0.5:2 molar ratios of $PbI_2$:$Pb(Ac)_2$:MAI. Films coated from 1:1:1 precursor ratio were specular dark brown colored, and the transition of color occurred during spinning. The transition of film color from transparent to dark brown was also noticed for films coated from 1:0.5:1 precursor ratio; however, these films were darker and had a whitish tint. This whitish tint arose from light scattering film possibly due to rougher morphology. Films derived from very low or no precursor MAAc molar ratios came out light brownish with quite rough morphology and incomplete surface coverage similar to those obtained from MAI and $PbI_2$ solution in DMF [51].

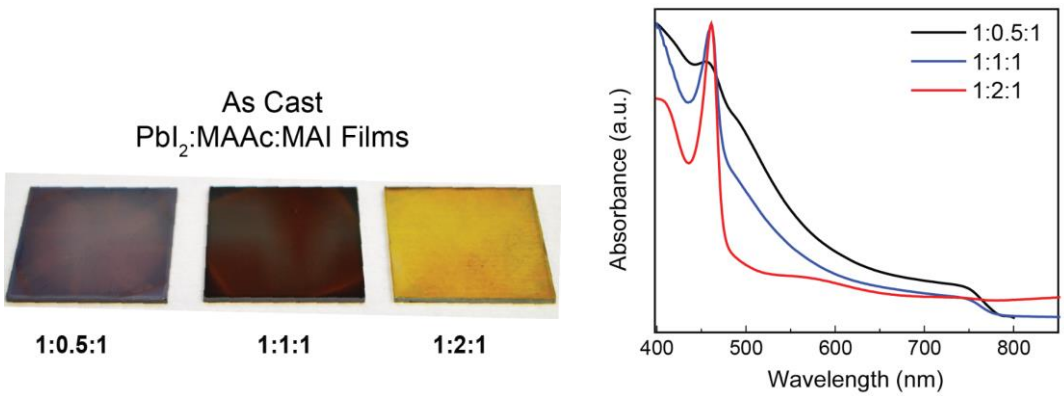


Fig. 3.2 (a) Photographs (b) UV-visible absorption spectra of as-deposited $PbI_2$:MAAc:MAI films mixed in different molar ratios.

To understand the optical transitions, UV-Visible absorption spectra for all as cast films were measured as shown in Figure 3.2.b. For all films, an excitonic absorption peak is observed at 460 nm. Such excitonic optical transitions are attributed to charge transfer in plumbate complexes [52],[53] and low dimensional perovskites[54]. In a previous study, it has been reported that this absorption peak belongs to the $PbI_x$·MAAc·MAI intermediate phase [55]. While all films show this excitonic peak, the brown color in 1:1:1 and 1:0.5:1 arises from the onset of absorption at 770 nm indicative of the formation of perovskite phase. The higher absorbance in 1:0.5:1 films compared to the absorbance of 1:1:1 films is attributed to the higher composition of the perovskite phase formation in 1:0.5:1 as evident from the XRD discussed in another section to follow.

### 3.3.2 FTIR

FTIR spectra were recorded using a Nicolet 6700 spectrometer in ATR mode. The optical cavity was continuously purged with $N_2$ while recording the FTIR spectra. Background scans were run before recording each sample's FTIR spectrum.

MAPI phase formation is also observed in the FTIR spectra of as-deposited 1:1:1 films as shown in Fig. 3.3. FTIR transmittance spectra of 1:2:1 films show peaks at 935 $cm^{-1}$, 988$cm^{-1}$ and 1258 $cm^{-1}$ characteristic of C-C stretch, $CH_3$ rock and $NH_3$ scissor of acetate functional group respectively. FTIR spectra of 1:1:1 films show similar peaks as of acetate along with specific characteristic peaks of perovskite phase namely $CH_3$ rock (911 $cm^{-1}$), C-N stretch (960 $cm^{-1}$) and $NH_3$ stretch (3132 $cm^{-1}$ and 3170 $cm^{-1}$) of MAPI [56]. Hence it is evident that in 1:1:1

films crystallization of perovskite phase occurs during spinning and for the case 1:2:1 films, the predominant phase is $PbI_x$·MAAc·MAI intermediate.

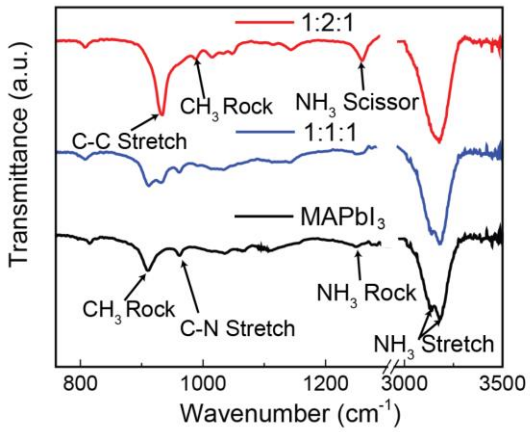


Fig. 3.3 Fourier transform infrared spectroscopy (FTIR) of perovskite films deposited using $PbI_2$:MAAc:MAI precursor mixed in different molar ratios.

### 3.3.3 SEM Measurements

SEM imaging was performed using the FEI Helios NanoLab 400 microscope. A probe current ranging between 5.4-21 pA was employed for imaging all samples at an accelerating voltage of 5 kV. Top view and cross-sectional SEM imaging was performed to investigate the film quality for different precursor ratios. Fig. 3.4 shows the SEM images of the top view and cross section of perovskite films prepared using the different ratio of precursor materials MAI, MAAc, and $PbI_2$. Figure 3.4 a - c represents the top view and Figure 3.4 d - f represents the cross-sectional view of 1:0.5:1, 1:1:1 and 1:2:1 films respectively.

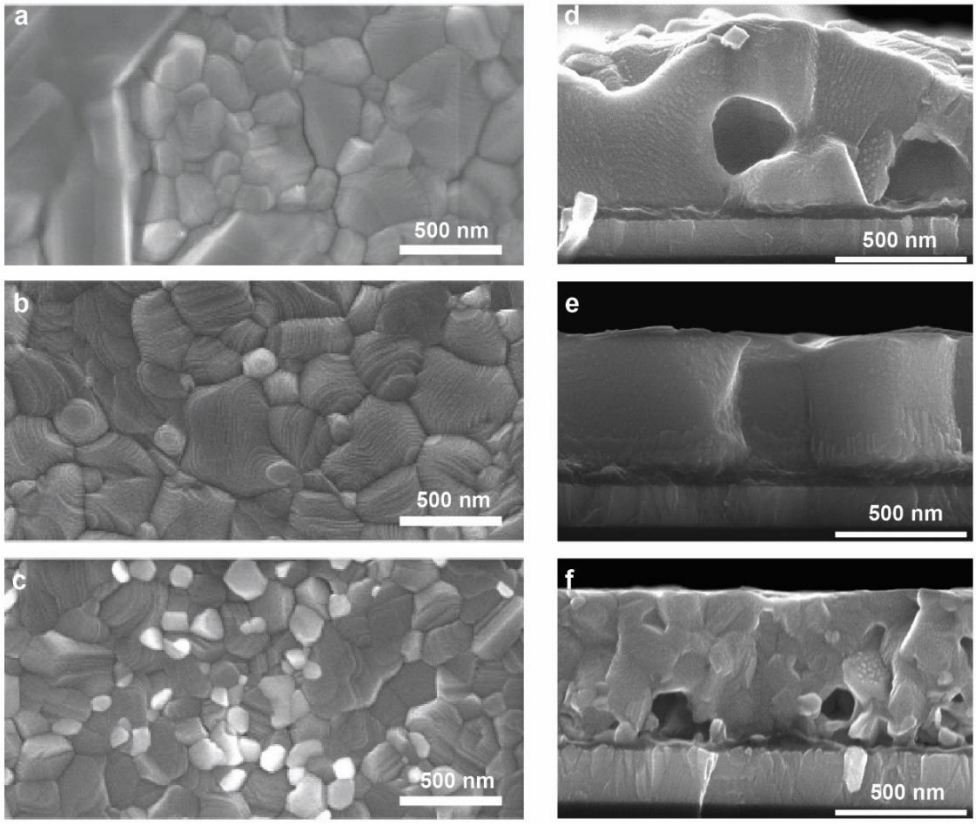


Fig. 3.4 Top view (a, b, c) and cross-sectional (d, e, f) scanning electron microscopy (SEM) of (a, d) 1:0.5:1, (b, e) 1:1:1 and (c, f) 1:2:1.

Obviously, precursor ratio has a significant impact on grain size, distribution, morphology, and surface roughness of the perovskite films. From the top view SEM images, for all ratios mostly polygon shaped grains of size ranged 100 nm – 500 nm formed the film. Film coated from pure $PbI_2$ and MAI show a very rough morphology with cracks and incomplete coverage as also observed previously by other (Fig. 3.5).[57]

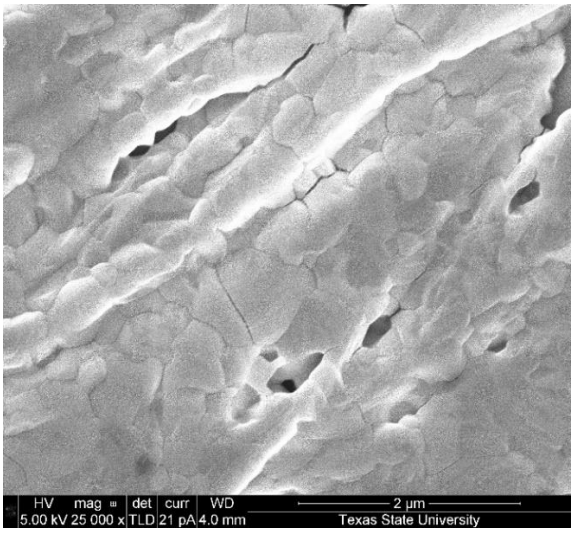


Fig. 3.5 SEM images of MAPI with precursor ratio $PbI_2$:MAI=1:1.

Thus, the precursor ratio plays a critical role in determining the surface morphology and specifically the grain sizes. Obviously, in terms of regularity and uniformity of grains, the 1:1:1 precursor ratio resulted in the best films. Although top view images show tightly packed grains and a continuous film surface for all ratios, the cross-sectional images show many irregularities especially, for 1:0.5:1 and 1:2:1 ratio. Grains are also laterally very uniform and large for 1:1:1 ratio compared to the other two ratios. The rougher surface was observed for films derived from 1:0.5:1 precursor ratio, whereas smoother flat surfaces were noticed for the 1:2:1 and 1:1:1 films. Such single crystalline grains were also observed by other for perovskite films grown by the two-step method when the as-deposited perovskite films are exposed to air before thermal annealing [58]. While the route of perovskite deposition is different, we observe the same effect here, where perovskite crystallization occurs during the spin deposition itself. This crystallization acts as a template for continuous grain growth along with the thickness as observed in both 1:0.5:1 and 1:1:1 films. The morphology of the 1:2:1

films is similar to the morphology reported for perovskite films derived from 3:1 MAI:$Pb(Ac)_2$ precursor [59].

At this point, it is essential to emphasize that the different precursor ratios only affect the phase composition, which in turn drives the nucleation and grain growth during film deposition. While the phase components for each ratio remains the same before and after annealing, the kinetics of perovskite nucleation seems to be the determining factor for the final film morphology. It is also important to note that, unlike DMSO, $PbI_2$ does not form mono or bi-adducts with MAAc as observed by others [60],[61]. These reports also emphasize that mono adducts are ideal for the formation of higher quality grains, however, the key difference is that the change in precursor ratio in our case only affects the nucleation rather than formation of different adducts or phases. Hence, the 1:1:1 precursor ratio aids in the formation of perovskite phase seeds which serve as a template for the growth of single crystalline grains along the thickness. Similar perovskite crystallization is also observed during the spin coating process of the 1:0.5:1 film but at the cost of rougher morphology. While the MAAc byproduct is essential to obtain a smoother morphology, the crystallization during the spin coating governs the growth mechanisms which in turn determines the final grain size of the perovskite films.

### 3.3.4 XRD

XRD measurements were done using a Rigaku SmartLab diffractometer. XRD patterns were obtained using a parallel beam configuration on perovskite films. To avoid conversion due to ambient exposure, in some case, films were coated with a thin layer of amorphous polymer PMMA in the glove box before

XRD characterization. Fig. 3.6 shows the XRD pattern of as-deposited films of three different mixing ratios.

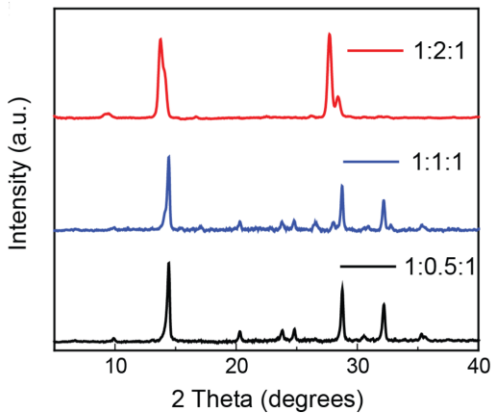


Fig. 3.6 X-ray diffraction (XRD) patterns of as-deposited $PbI_2$:MAAc:MAI films mixed in different molar ratios

The films derived from all three precursor ratios show peaks at ~ 14° and ~ 28° representative of the perovskite crystal orientations (002) /(110) and (004)/(220) respectively. A closer look at these peaks reveals that the 1:2:1 films show a more dominant (002) peak at 13.76° and a smaller (110) shoulder at 14.12°.[62] This difference is easily observable in the second order peak of each, namely, (004) at 27.7° and (220) at 28.46°. While the (110) and (220) peaks are also present in films coated from 1:1:1 precursor ratio, the preferred growth is still along the (110) crystallographic orientation. Growth along the (110) direction has been shown favorable for less defective grains by Li et al.[50] Their study highlights the role of inorganic seeding agents for the preferred crystal orientation. The peak at 9.5° belongs to the intermediate of PbIx-MAI-MAAc as shown in our previous study. The exact composition and structure are not known yet and still need to be elucidated.

### 3.3.5 Pole figure analysis

To further investigate the preferred crystallographic plane of spin-coated polycrystalline MAPI, the XRD pattern of the thin film were compared with both theoretical and experimental MAPI powder XRD. Pole figure analysis was performed to quantify the tilt angle between the preferred plane and the surface normal. From the previous discussion, it was evident that, 1:1:1 $PbI_2$: MAAc: MAI precursor ink results in best quality film among other ratios. That is why, 1:1:1 MAPI films were considered for this study. $\theta/2\theta$ scans of MAPI thin films were performed to determine the peak positions of different planes. Simulated XRD of MAPI powder was done using the VESTA software. Experimentally done powder XRD of MAPI reported in ref. [63] was adopted for comparison. Figure 3.7 shows XRD patterns of all three types of samples mentioned above. At room temperature, MAPI thin films are expected to be in the tetragonal phase. Distinct peaks from different crystallographic planes are observed, in the range from 10° to 50°. The list of the peaks obtained from MAPI thin films and associated miller indices are enlisted in table 3.1 below. This list of peaks agrees with the reported tetragonal perovskite XRD data. Three strong peaks are obtained at 14.06°, 28.45°, 31.88°, and 43.08°, which are representing the planes (110), (220), (310), and (314), respectively [63]–[65]. It is worth noting that, almost all the peaks obtained from simulation agree with the peaks obtained from the experiment data. Note that, the individual peaks in the peak clusters as observed from the theoretical data could not be resolved experimentally. The relative intensities of the peaks were varied from sample to sample.

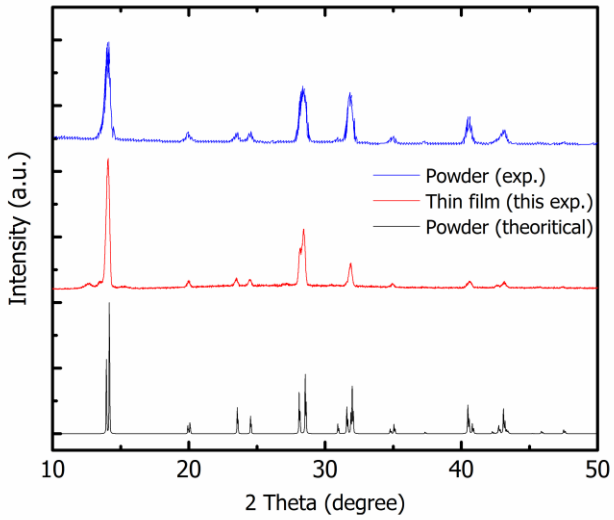


Fig. 3.7 Room temperature X-ray diffraction (XRD) patterns of MAPI powder (top) this XRD data reproduced from ref. [63], 1:1:1 $PbI_2$:MAAc:MAI film of this research (middle) and powder simulated using VESTA software (bottom).

Table 3.1 XRD peak positions of MAPI and associated Miller indices.

| Miller indices | | | Peak position, 2θ (degree) |
|---|---|---|---|
| h | k | l | |
| 1 | 1 | 0 | 14.06 |
| 2 | 0 | 0 | 19.99 |
| 2 | 1 | 1 | 23.497 |
| 1 | 0 | 1 | 24.502 |
| 2 | 2 | 0 | 28.451 |
| 2 | 1 | 3 | 30.96 |
| 3 | 1 | 0 | 31.884 |
| 2 | 0 | 4 | 34.96 |
| 2 | 2 | 4 | 40.586 |
| 3 | 1 | 4 | 43.14 |

In the following table 3.2, a quantitative comparison of X-ray counts for the different planes is made relative to the highest intensity (110) plane. For simulated

and experimental powder XRD, (310) plane count is about 36.4% and 44% of (110) plane respectively. The relative intensity of the (314) plane is lower or equal 25%. On the other hand, the MAPI thin film XRD shows only 21% and 7% relative intensities for the (310) and (314) plane respectively compared with (110) plane intensity. This quantative comparison suggets (110) that the crystallites prefer to growth with the (110) plane parallel to the substrate for the MAPI thin films.

Table 3.2 Quantative comparison among three different MAPI plane XRD counts.

| | Powder XRD using VESTA | | Thin film of (this work) | | Powder XRD (ref. [63]) | |
|---|---|---|---|---|---|---|
| Plane | Intensity | Ratio | Intensity | Ratio | Intensity | Ratio |
| (110) | 100 | 1 | 2013 | 1 | 1778 | 1 |
| (310) | 36.4 | 0.364 | 422 | 0.21 | 786 | 0.44 |
| (314) | 17.4 | 0.174 | 140 | 0.07 | 449 | 0.25 |

Only $\theta/2\theta$ scan are not adequate to explore the complete picture of preferred crystal orientation distributions. The angle between the surface normal and the preferred orientation is also needed to be determined. Pole figure measurement and their analysis were performed for two planes, i.e. (110) and (310). The detector was fixed at 14.06° and 31.884° positions respectively. The three-dimensional pole figure of (110) is shown in fig. 3.8a. The corresponding stereographic projection is presented in fig. 3.8 (b). Maximum Bragg reflection is observed at $\alpha=0^{o}$, as seen in the right panel of fig. 3.8 (b). The intensity decreases with $\alpha$. This implies that, for most of the crystallites, the (110) plane is parallel to the sample surface.
The sharpness of the peak of the alpha cut confirms the moderate strength of the texture.

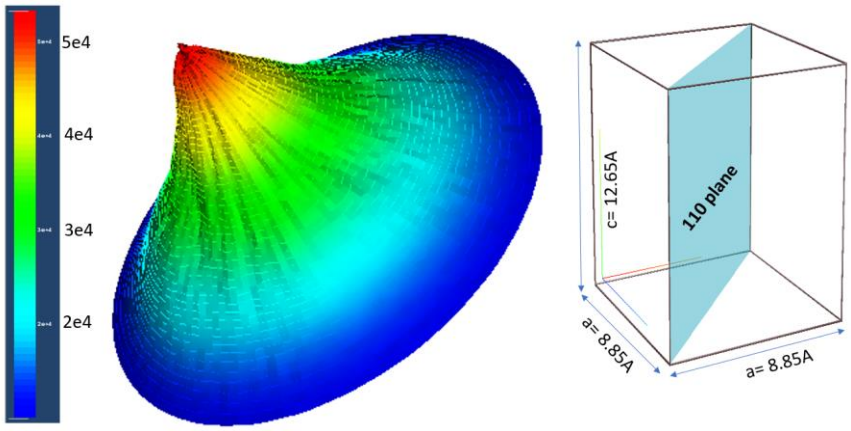


(a)

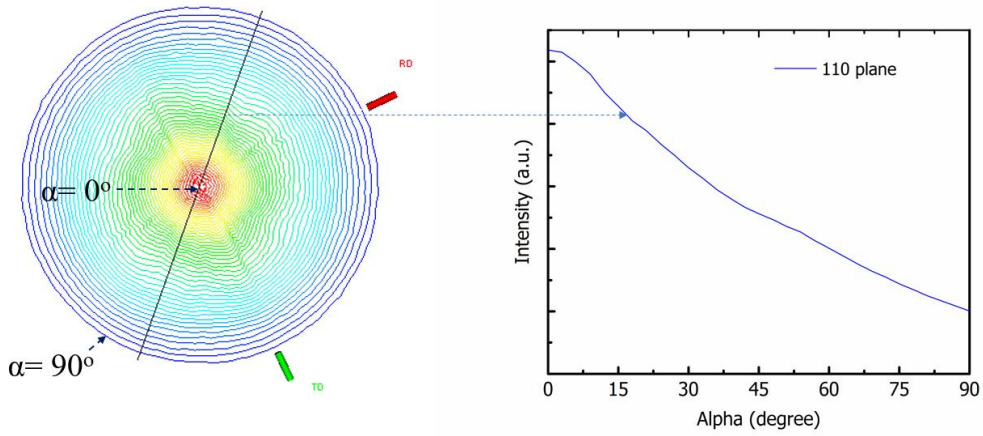


(b)

Fig. 3.8 (a) 3D pole figure of MAPI film at the (110) plane (top left) and the schema of associated in the crystal plane. (b) α-scan at β = 45°.

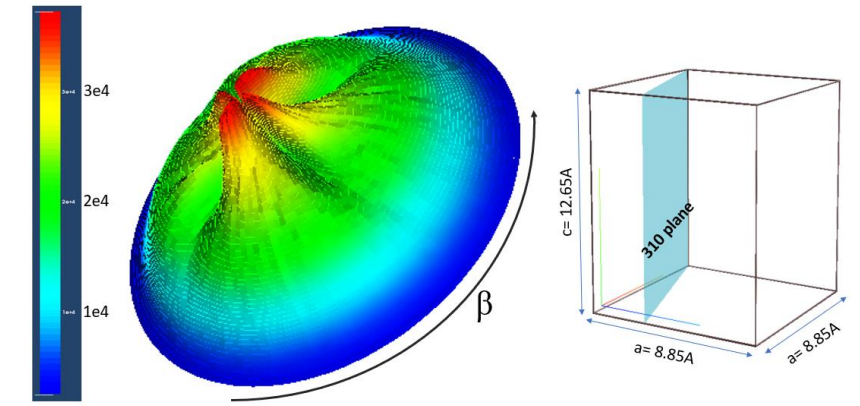


(a)

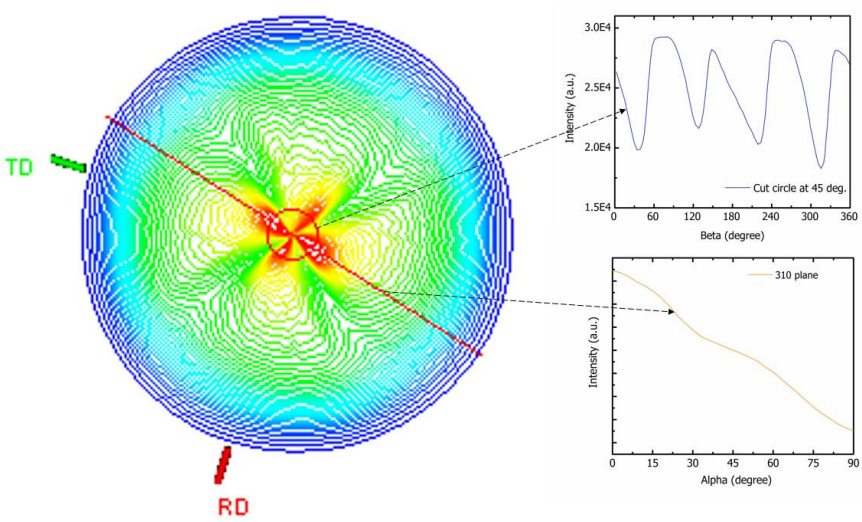


(b)

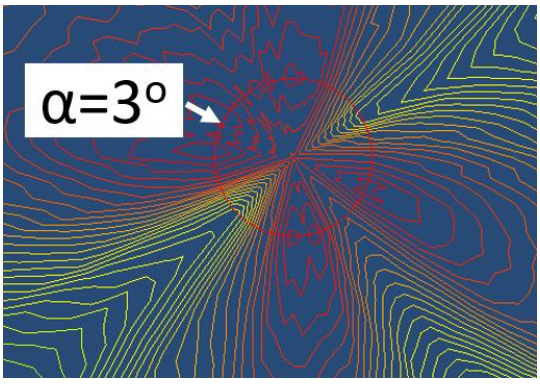


(c)

Fig. 3.9 (a) 3D pole figure of MAPI film at the (310) plane (top left) and the schema of associated in the crystal plane. (b) α-scan at β = 45°. (c) A magnified view of stereographic projection of 3D pole figure of MAPI film at the (310) plane.

Fig. 3.9 (1) shows the 3D pole figure for (310) planes and corresponding plane schema in a model crystal. The pole of (310) has a similar intensity profile of (110) plane except the presence of four symmetric lobes. These four lobes appear due to four-fold symmetry of this plane. Intensity profile at $\beta = 45^{o}$, as shown in fig. 3.9 b represents the four-fold symmetry more clearly. Although from the α-scan of stereographic projection, maximum Bragg reflection seems to be at $\alpha=0^{o}$. A magnified view of stereographic projection, as shown in fig. 3.9 c shows the maximum intensity distributed by three degrees from the center.

In summary, (110) and (310) are two most preferred orientations respectively. The (110) plane is parallel to the surface, whereas the (310) plane is tilted ~$3^{o}$ with the surface.

### 3.3.6 Crystal growth hypothesis and scope for future research

The fig. 3.10 below illustrated the mechanisms involved in spin coating step by step from left to right.

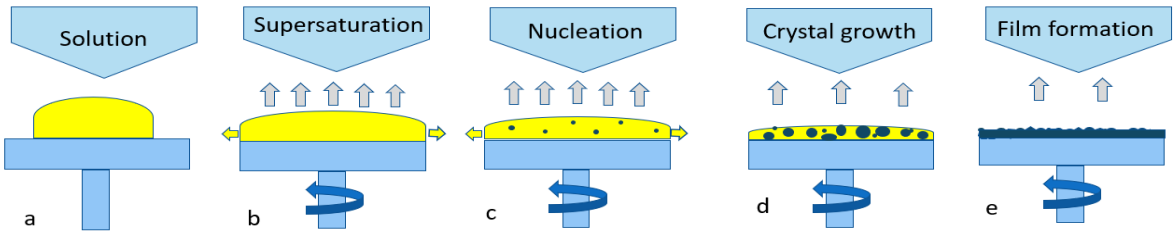


Fig. 3.10 Simplified schema of spin coating thin film deposition mechanism

In the first step, the MAPI precursor solution is drop casted on the static substrate. Then the sustrate allowed to spin at a desired rpm (2000 - 5000) for a specific time period (30 – 60 s). As a result of spinning, the access solvent push off the substrate and also

started to evaporate. Due to evaporation, the solution becomes supersaturated. Nucelation stated in the supersaturated solution followed by crystal growth. After finishing the spin coating, the samples are annealed for a certain time period (5 min) at a some temperature ($100^{o}$C). The purpose of the annealing is to get rid for the residue solvent and enhance crystallization process.

In the previous sections, the SEM and XRD results were presented for morphology and crystallography study. The results were conclusive. These analyses are not adequate to explain the detail of crystal growth mechanism. In particular, the issue whether the crystal growth happening from the top of supersaturated solution or from the substrate surface is still unresolved. One hypothesis can be made that the, nucleation started in the top of supersaturated solution during spinning since the solvent is evaporating from the top first. Then the nucleus continues to grow. The alternative hypothesis may be, nucleation starts at the surface of the substrate and grain grows upward, considering that the substrate offers energetically favorite sites for nucleation.

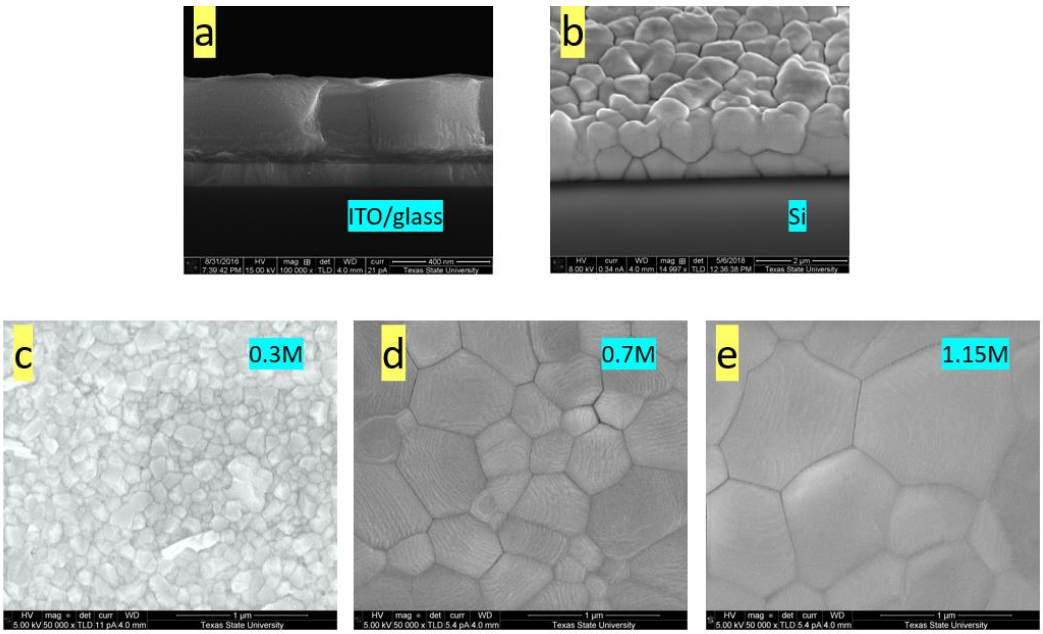


Fig. 3.11 (a) MAPI cross sectional SEM image on ITO/glass substrate (b) tilted cross sectional SEM on Si substrate. (c-e) Top view SEM images of MAPI thin film synthesized from different precursor concentration (1:1:1 of $PbI_2$:MAAc:MAI).

To investigate the surface dependency of MAPI thin film growth, MAPI was deposited using the identical recipe on both ITO/glass and Si substrate. Interestingly, for ITO/glass, only one layer of grains covered the substrate (see fig. 3.11a). On the other hand, there are two layers of MAPI grains on the Si substrate (see fig. 3.11b). This indicates the nucleation and crystal growth is surface sensitive. Also, MAPI films were deposited from different concentration of precursor resulted different grain size. Fig. 3.11 c to e represents the SEM images of the MAPI thin film synthesized from 0.3M, 0.7M and 1.15M precursor concentration respectively. In all cases 1:1:1 of $PbI_2$:MAAc:MAI ink formulation was used. The grain size increases with the solution concentration. Hence, assuming every grain grows from one nucleus, the nucleation rate is highly dependent on solution concentration. Nucleation and grain growth are dependent on

substrate and solution concentration. Other process parameters such as ambient pressure, temperature and humidity may have impact on nucleation and grain growth. The spin coating deposition process takes only 30 - 60 s. The nucleation and grain growth occurring within this short period. MAPI deposition is usually done in $N_2$ filled glove box. To study the nucleation and grain growth mechanism directly, an in-situ capability needs to be built which can be performed during spin coating. Therefore, the complete understanding of nucleation and grain growth worth a comprehensive study which is out of the capability of current facility and scope of this research.

### 3.3.7 Ellipsometry

The device structure of the MAPI solar cell used in this research was ITO/PEDOT:PSS/MAPI/$C_{60}$/BCP/Al on a glass substrate (fig. 3.12 a). Details of the MAPI solar cell fabrication, operation, and performance are presented in chapter 4. Most of the layers are deposited using solution-based spin coating processes, which make these devices very promising alternative candidates of current commercial solar cells. Due to inherent roughness of top layer and interfaces, the similarity of optical absorption spectra of transparent layers and anomalous dispersion of the perovskite, modeling of such device film stack is critical for resolution of individual film thicknesses. Ellipsometry was used to extract the optical constants and develop a method to determine the thickness of the constituent layers of MAPI solar cell.

In this section, the process of building the ellipsometry model from scratch for the benchmark hybrid perovskite $MAPbI_3$, and ITO/PEDOT:PSS bilayer thin film stacks on the glass substrate is presented. The models were extended to measure the individual

layer thickness MAPI/PEDOT:PSS/ITO film stack on the glass substrate as shown in fig. 3.12 b and c using the model of the individual layers.

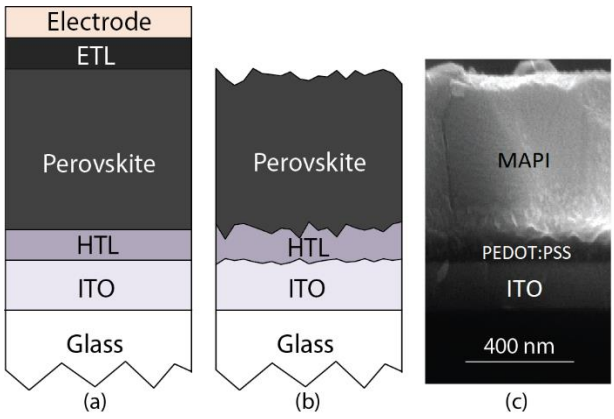


Fig. 3.12 (a) Inverted planar perovskite solar cell architecture with ideal interfaces, (b) Schematic model of real MAPI/PEDOT:PSS/ITO film stack with interface roughness representation, (a) Cross sectional SEM image of MAPI/PEDOT:PSS/ITO film stack on glass substrate.

### 3.3.7.1 MAPI

The first step of building an ellipsometry model from scratch with unknown optical properties is to determine whether the film is transparent, absorptive, or partially absorptive. Glass substrates were selected whose optical properties are well known. UV-Vis spectroscopy of the film has been performed. Fig. 3.13 (a) shows the UV-Vis absorption spectra. MAPI exhibited absorptive behavior. While thicker films' absorption was higher compared with thinner film counterpart, the pattern of absorption was similar for different film thickness derived from different solution concentrations. $MAPbI_3$ films have high absorbance for the entire visible spectra of 390 nm - 780 nm. The onset of absorption is at 780 nm, which implies the bandgap is ~1.58 eV. Two other absorption

peaks are observed at 375 nm (3.3eV) and 480 nm (2.58eV). This information is helpful for initial selection of layer type used in the ellipsometry model.

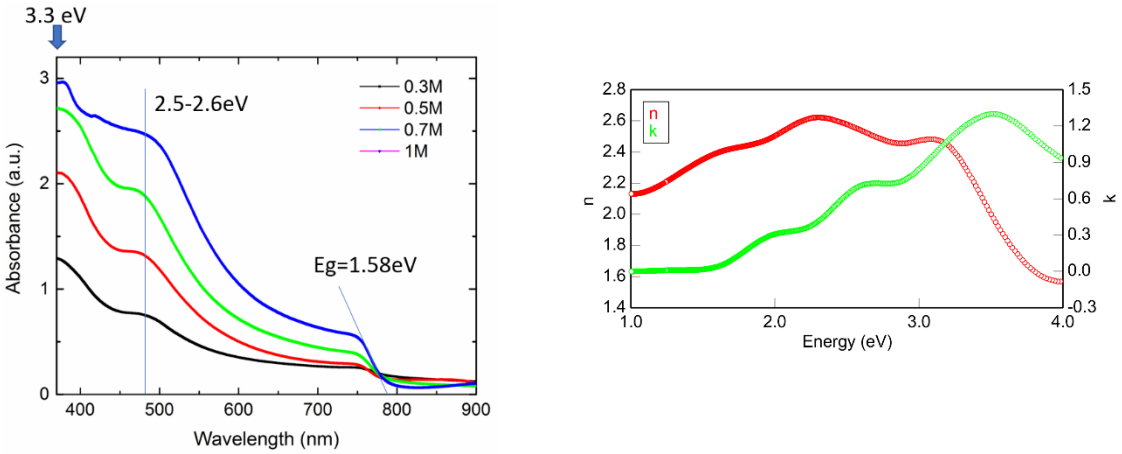


(a) (b)

Fig. 3.13 (a) UV-Vis absorption spectra, (b) Optimized optical constants vs. energy of MAPI film on glass substrate.

The B-spline model allows for arbitrary flexibility of $n$ and $k$ over the entire spectra. This feature is especially advantageous to determine the unknown optical properties for absorptive and partially absorptive thin films. For a MAPI on the glass substrate, '*B-spline material with transparent reflective substrate'* was chosen as the starting model. All the known parameters such as film thickness, rms roughness were supplied in the model. Only optical constants were fit. We have performed a global fit over a range of $n$ and $k$ value with a defined number of steps. The best fit was obtained for $n$ and $k$ ranging 1.3-3 and 0-1.5 respectively. Several verification steps were applied to justify the validity and accuracy of optical constants. First, the extinction coefficient spectra from the model is expected to be similar to the measured optical absorption spectra from UV-Vis which is a direct measurement. From the fig. 3.13 (b) the absorption

peaks match with the model extinction coefficient. The value of $n$ and $k$ are also physical. To quantify the accuracy of the model, a parameter named goodness of fit is used defined by the following equation 3.1.

$$MSE = \sqrt{\frac{1}{3m-l}\sum_{i=1}^{m}[(N_{Ei}-N_{Gi})^2+(C_{Ei}-C_{Gi})^2+(S_{Ei}-S_{Gi})^2]\times 1000} \qquad (3.1)$$

Where, $m$ is the number of wavelengths measured, $l$ is the number of fit parameters, $N = \cos(2\Psi)$, $C = \sin(2\Psi)\cos(\triangle)$, $S = \sin(2\Psi)\sin(\triangle)$.

The value of MSE indicates the level of accuracy of the model. Performing a global fit in each measurement is time-consuming option, especially if the step size of the parameters is small. Moreover, one may end up with a misleading result for the defective film caused by process drift since the global fit can fit the n and k value to reduce MSE. Thus, it is not the appropriate choice of model for fast data analysis and measurement. To build a straightforward model for quick measurement, the model was rebuilt by parameterizing the optical constants using GEN-OSC (stands for general oscillator). In this step, the optical constant obtained from B-spline global fit were fitted with a sum of several Tauc-Lorentz oscillators. Each Tauc-Lorentz oscillator is defined by its amplitude, energy center, broadening and bandgap. From the extinct coefficient spectra, three absorption peaks were observed at approximately ~2eV, ~2.5eV and ~3.3eV. Two of these peaks match closely with peaks observed in the measured UV-Vis spectra. The absorption peak at 2eV was not distinguishable in the UV-Vis spectra. All these critical energy points mentioned here are associated with valance band to conduction band transition confirmed by both experimental and theoretical studies [66]. The bandgap is extracted from UV-Vis and ellipsometry ~1.58eV and ~1.56eV respectively, which agree

with the literature [66]. To make the model initially sum of three oscillators were used with the energy center located in three known absorption peaks. The amplitude and broadening parameters were adjusted to find the best fit. Two more oscillators were needed to fit the nonzero absorption tail higher than 4eV. All oscillator parameters assigned for best fit are listed in the following table 3.3.

Table 3.3 Tauc-Lorentz oscillator parameters of GEN-OSC model. 1.56eV bandgap was used for all oscillator.

| Oscillator | Energy center (eV) | Amp | Br |
|---|---|---|---|
| OSC1 | 1.58 | 42 | 7.05 |
| OSC2 | 1.9 | 7 | 0.35 |
| OSC3 | 2.53 | 6 | 0.5 |
| OSC4 | 3.33 | 9.5 | 0.77 |
| OSC5 | 6.4 | 3.3 | 3.3 |

After finalizing the models, both B-spline and oscillator models were applied for thickness measurement of three samples of different thicknesses. The measurements were also performed using profilometer. It is observed that for higher thickness, MSE and deviation of the two measurements increased. Increase in MSE for higher thickness is reasonable. The thickness of sample 1 also measured using cross-sectional SEM (see fig. 3.14) and step height measurement by AFM in three different locations. All the measurement results were summarized in table 3.4.

Table 3.4 Comparative MAPI film thickness measurement results using different techniques.

| Sample | Profilometer thickness (nm) | Ellipsometer data | | | | SEM Cross section height* (nm) | AFM step height* (nm) (Three different location) |
|---|---|---|---|---|---|---|---|
| | | B-spline model | | GEN-OSC model | | | |
| | | Thickness (nm) | MSE | Thickness (nm) | MSE | | |
| 1 | 334 | 351 | 15.56 | 346.2 | 17.23 | 335 | 328.3<br>343.9<br>338.5 |
| 2 | 190 | 192 | 11.78 | 189 | 9.27 | | |
| 3 | 125 | 123 | 7.3 | 122.5 | 6.98 | | |

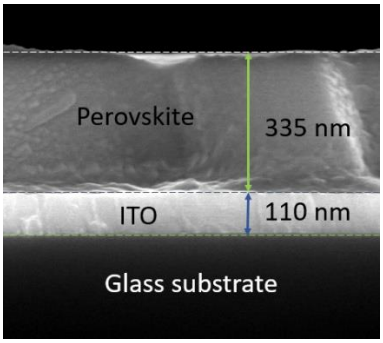


Fig. 3.14 Cross-sectional SEM of perovskite thin film on ITO/Glass substrate. ITO/Glass substrate was used to eliminate the charging problem.

3.3.7.2 PEDOT: PSS and ITO

PEDOT: PSS, which is an acronym of poly (3,4-ethylenedioxythiophene) polystyrene sulfonate, was used as the hole transport layer (HTL) of the solar cell. Optical constants of PEDOT:PSS was determined using ellipsometry, and a model was built for thickness measurement. From the UV-Vis absorption spectra as shown in Fig.

3.15 it can be concluded that, PEDOT: PSS thin film is transparent in the entire visible range. The transparency of a PEDOT:PSS thin film is also evident from the optical photograph of a coated film.

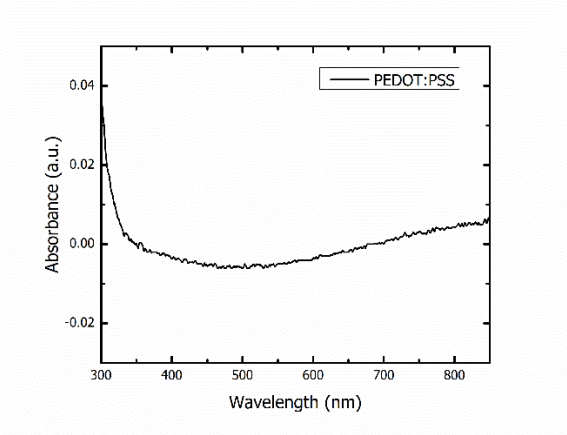


Fig. 3.15 The absorption spectra of PEDOT:PSS thin film deposited on a glass substrate using spin coating.

Optical transparency in the visible range allows us to consider the extinction coefficient, *k=0.* Refractive index *n* of such a transparent material can be described as wavelength, $\lambda$, using a Cauchy Equation, which is shown in equation 3.2 to three terms.

$$n(\lambda) = a + \frac{b}{\lambda^2} + \frac{c}{\lambda^4} \ldots \qquad 3.2$$

The coefficients *a*, *b*, and *c* were optimized by the CompleteEASE software of J. A. Wollam. In the fitting process, known thickness measured by profilometer were fixed to the model for fitting *a*, *b*, and *c*. Every single parameter was fitted individually. As the value of the second and third term are negligibly small compared to the first term, *a* can be considered as an appropriate approximation of the *n* dispersion. The coefficients a, b and c optimized as 1.196, 0.0756 and 0.00123 respectively. The refractive index was obtained between 1.26 – 1.65 for the wavelengths between 900 nm – 300 nm. This range

conforms with reported results [67]. Once the model was completed by optimizing all parameters, it was used for thickness measurement of varied PEDOT:PSS film thickness on glass substrates.

Table 3.5 Comparison of thickness measurement of PEDOT:PSS thin film using profilometer and ellipsometer.

| PEDOT:PSS on Glass | Spin coater RPM | Profilometer thickness (nm) | | | Ellipsometer thickness (nm) | MSE |
|---|---|---|---|---|---|---|
| | | Spot 1 | Spot 2 | Spot 3 | | |
| Sample 1 | 2000 | 63.82 | 61.98 | 62.06 | 65.37 | 12.35 |
| Sample 2 | 3000 | 45.98 | 48.94 | 46.94 | 47.89 | 10.33 |
| Sample 3 | 4000 | 37.59 | 36.2 | 39.3 | 38.96 | 9.16 |

Table 3.5 presents the thickness data measured by profilometer and ellipsometer. Ellipsometer results agreed with the profilometer with a maximum 5% variation. Note that, there is a possibility of 2 nm offset in the profilometer measurement due to noise. The MSE increases for higher thickness.

Different build-in model options were available in the CompleteEASE library for ITO. Since the optical properties of the ITO thin films differ from process to process, the parameterized ITO model was selected and modified to fit with the ITO properties of this project.

#### 3.3.7.3 MAPI/PEDOT:PSS/ITO/Glass model

The individual optimized models were added sequentially to upgrade the model for a MAPI/PEDOT:PSS/ITO film stack thickness measurement. The top layer roughness, intermixing property at the interface, and backside reflection was taken into consideration for building the complete multilayer model. Fig. 3.16 (a) and (b) shows the

refractive index and extinction coefficient of MAPI, PEDOT: PSS and ITO thin film respectively.

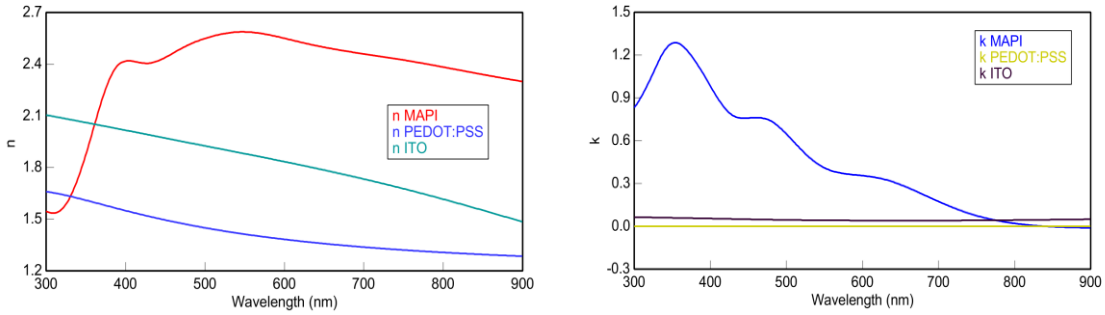


(a) (b)

Fig. 3.16 (a) Refractive index (b) Extinction coefficient of MAPI/PEDOT:PSS/ITO film stack.

From the three-layer model, the thickness of three layers cannot be resolved individually. The reason can be interpreted from the similarity of the extinction coefficient compared with the MAPI. However, if the thickness of the first two layers provided as input (measured before the deposition of MAPI layer), the third layer (which is MAPI film) thickness can be determined with reasonably high accuracy. Table 3.6 presents the results of MAPI film thickness measurement from two different techniques.

Table 3.6 Film thickness of MAPI using ellipsometer and profilometer.

| Sample ID | PEDOT: PSS thickness (nm) (fixed) | ITO thickness (nm) (fixed) | Perovskite thickness (nm) Measured | | MSE | Variation in two techniques (%) |
|---|---|---|---|---|---|---|
| | | | Profilometer (nm) | Ellipsometry (nm) | | |
| Sample 1 | 38 | 110 | 330 | 353 | 38.6 | 5.30% |
| Sample 2 | 25 | 110 | 370 | 365 | 27 | 1.40% |
| Sample 3 | 25 | 110 | 290 | 279 | 31 | 3.90% |

From table 3.6, the thickness of MAPI film can be determined by using the three-layer model by fixing sub-layer thickness obtained from pre-measurement. The maximum deviation with profilometer thickness is 5.3 %.

#### 3.3.7.4 Ellipsometry back reflection issue

Backside reflection is in transparent substrate is a common issue due to overlapping of the backside reflected signals and front surface signals at the detector. This unwanted backside reflection must be considered while fitting. Common practices to get rid of back side reflection are roughening the back surface by sand paper or attaching a scotch tape. The other way is using index matching materials.[68] These approaches to suppress backside reflection are very effective. However, for industrial production line, measurement time should be as short as possible. Thus, roughening or treating every samples individually are impractical. The final aim of this project is to build an industry compatible model for multilayer measurement. For this reason, instead of minimizing backside reflection using any physical method, we preferred to fit the *"backside reflection"* parameter in the CompleteEASE software.

### 3.3.8 Thickness control of perovskite thin film

The individual application requires a specific range of thickness of perovskite thin films. For instance, typically, 300 nm – 600 nm film thickness used for photovoltaic solar cells [37], [69]. On the other hand, for transistor applications, ~100 nm is the reported optimum thickness [70]. Hence, the capability of determining the process parameters for known film thickness is essential. For solution-based spin coating, there are two main control parameters for the film thickness. The concentration of solution and the spin

speed. Both parameters were studied for formulating a relation between film thickness and process parameters. It is important to note that, using solution-based spin coating arbitrarily thin or thick film cannot be created due to the solubility limit of the precursors and spin speed limit of the spin coater. For this experiment, the best ink formulation 1:1:1 of MAI: $PbI_2$: MAAc in DMF was utilized. Ink concentrations were varied from 0.1M to maximum achievable concentration 1.15M. The spin speed was varied from 1000 rpm to 10000 rpm (maximum limit of RPM in the lab).

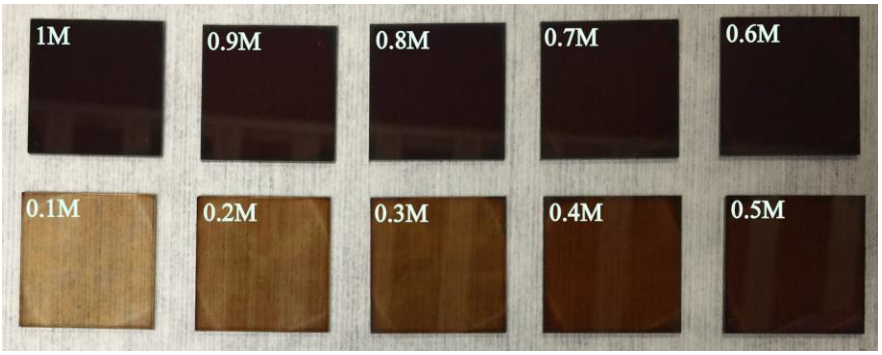


(a)

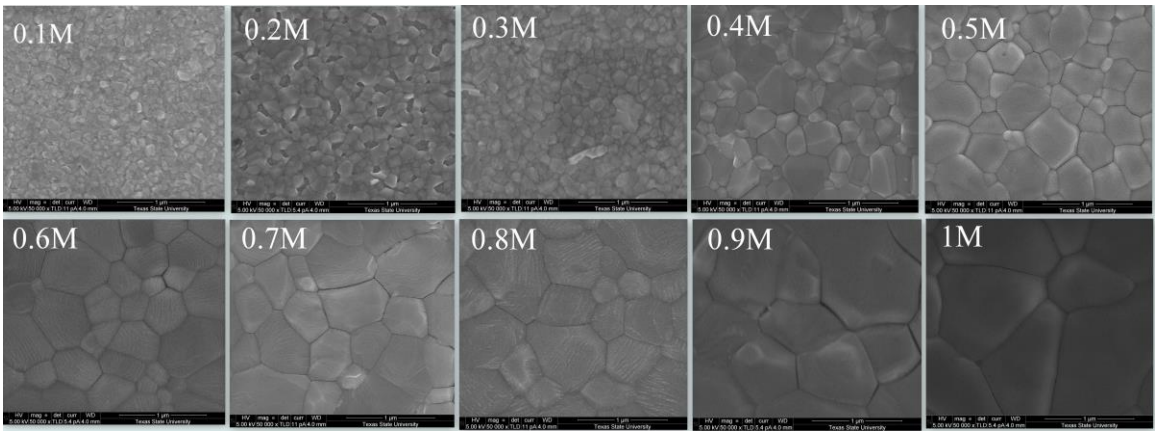


(b)

Fig. 3.17 (a) Optical photograph (b) SEM images of MAPI thin film deposited from different ink concentration at 3000 rpm.

As shown in fig. 3.17 (a), with the increase of concentration for the same spin speed of 3000 rpm the film color changes from light copper brown to dark brown. The transparency of the film decreases with concentration. Fig. 3.18 (a) represents the thickness versus solution concentration. Thicknesses were measured using profilometer, and the average thickness of three identical samples were used for the plot. The relationship is almost linear. From the linear fit of this graph, the film thickness can be expressed in terms of solution concentration as the following equation:

$$y = 335.6x - 42$$

Here, $y$ is film thickness in nm unit and $x$ is the solution concentration in the molar unit.

To investigate the coverage of the film, the SEM images of all 10 representative films were taken (fig. 3.17 b). It is evident that, below 0.3M concentration, the coverages were not complete. Although from 0.3 M to higher concentration, the full film coverage was observed, the average grain size was smaller for the lower concentration inks. The reason behind the grain size variation requires further systematic study which was out of the scope of this research. Fortunately, the film thickness required for this research was in the range of 300 nm – 600 nm. This thickness was achieved from 1M concentration ink, which results in larger crystal grains.

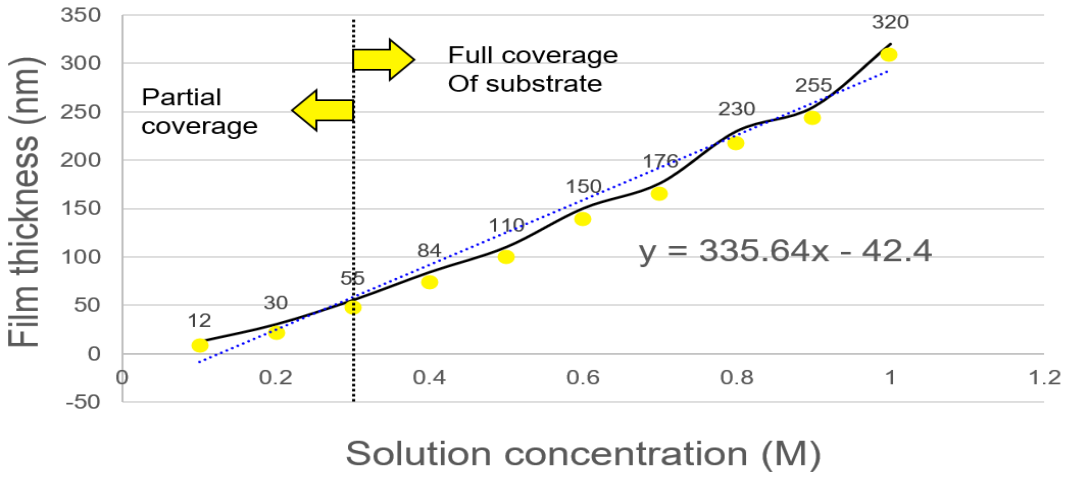


(a)

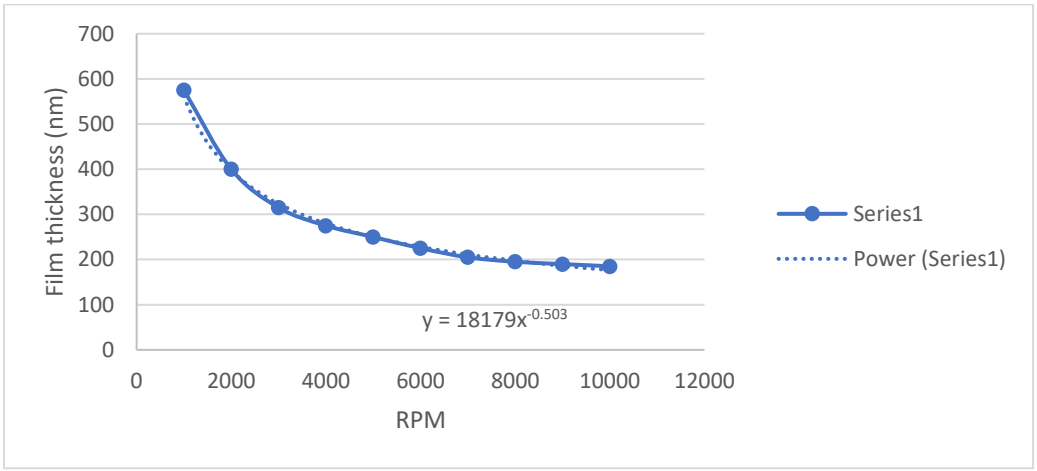


(b)

Fig. 3.18 (a) MAPI film thickness vs. solution concentration, (b) MAPI film thickness vs. spin speed.

The film thickness is generally proportional to the inverse of the square root of spin speed. Thus, thickness $y$ can be written as,

$$y = \frac{k}{\sqrt{w}}$$

Here, $y$ is the thickness in nm, $w$ is the spin speed in rpm and $k$ is the constant.

While this is a well-known equation, to make it work $k$ need to be determined experimentally for an individual process. In this experiment, MAPI films were deposited using 1M ink at different spin speed. The thicknesses of the film measure surface profilometer. The recorded data were plotted and fitted as shown in the fig. 3.18 (b). From fitting equation, $k$ is determined as 18180.

# 4. MAAc ASSISTED PEROVSKITE OPTOELECTRONIC DEVICES

Note: Most of the contents from this chapter was published in the *Journal of Material Chemistry C* on 15 September 2017 by the author of this thesis and co-authors of the same research group. DOI number of the publication is 10.1039/C7TC02928D. The contents taken from the published article were cited where applicable.

## 4.1 Introduction

The goal of MAPI thin film optimization using MAAc is to improve the performance of devices while keeping the process of deposition simple. Process simplicity will lead to higher scalability and reduce cost. In this chapter, the performance of solar cells using MAPI thin film derived from different precursor ratios are presented. To investigate the compatibility of the MAAc assisted method for other perovskites, $MAPbBr_3$ thin film was synthesized and used for perovskite LED fabrication. Perovskite LED shortened as PeLED and used interchangeably throughout this thesis. Performance of PeLED were investigated for different $MAPbBr_3$ precursor ratio to identify the best precursor formulation. Before moving to the experimental detail and metrology of the devices, the structure of the devices is revisited in the section to follow. The performance parameters used for evaluation of optoelectronic devices are also discussed.

## 4.2 Perovskite solar cell device architecture and operation

As described in section 1.6 of the first chapter, unlike conventional p-n junction solar cell, perovskite solar cells are either of n-i-p or p-i-n architecture. Both structures can further be categorized as mesoscopic and planar. Although the efficiency is relatively higher, high temperature (> 450$^{o}$C) treatment is needed for fabricating the mesoporous structure. On the other hand, regular n-i-p planar structure results in considerable hysteresis. Considering these facts, the inverted planar structure was chosen for this project. Note that, the aim of this project is not to develop the highest efficiency solar cell, instead enhance the scalability of fabrication.

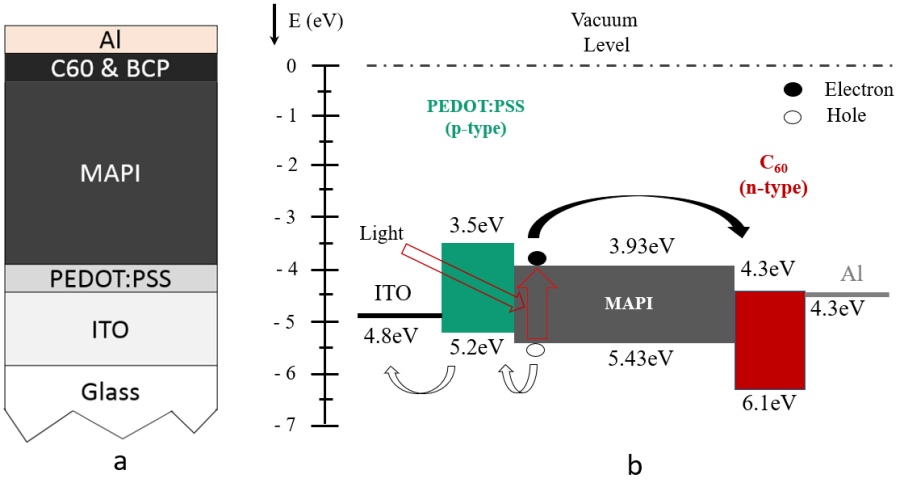


Fig. 4.1 (a) MAPI solar cell architecture used in this research, (b) Band diagram and carrier transport schema of the structure in illuminated condition.

In this structure, the p-type hole transport layer was deposited on the ITO/glass substrate. Subsequently, MAPI absorber, n-type C60, a BCP buffer layer and finally an aluminum electrode layer was deposited. The device layer stack and associated band diagram is presented in fig. 4.1 (a) and (b) respectively. The glass, ITO, and PEDOT:

PSS hole transport layer are transparent. The bandgap of MAPI is ~1.59 eV, which makes it an outstanding absorber material for PV cell. Thus, when sunlight is incident on the glass side of the device, it passes through glass, ITO and PEDOT: PSS and is absorbed in the MAPI thin film. Therefore, charge carriers (electrons and holes) are generated in the MAPI absorber. These photo generated electrons and holes are injected to electron transport layer (C60) and hole transport layer (PEDOT: PSS) respectively. If there is a load connected across the electrodes, power can be extracted from the solar cell to drive the load. The performance of the solar cell evaluated by current-voltage characteristics and some associated parameters. The following section discusses the solar cell performance evaluation parameters.

## 4.3 Solar cell model and performance parameters

The equivalent model of the solar cell, and the associated current-voltage characteristics curve are shown in fig. 4.2 (a) and (b) respectively. The solar cell model consists of a current source connected in parallel with an ideal diode. Since a real solar cell cannot be ideal, a series and a shunt resistance are added to the equivalent circuit as in the figure. The shaded area in the I-V curve (fig. 4.2 b) represents the maximum power. $V_{mp}$ and $I_{mp}$ are the associated voltage and current, respectively. However, clearly, $V_{mp}$ and $I_{mp}$ are not the maximum voltage and current that can be obtained from a solar cell. As can be seen from the curve, the maximum current generated by the solar cell when voltage across the device is zero. This current is known as short circuit current, represented by $I_{SC}$. $I_{SC}$ depends on area of the device. Thus, to remove the dependency, $I_{SC}$ often normalized by dividing the area of the device and represented as short circuit current density $J_{SC}$ (unit $mA/cm^2$).

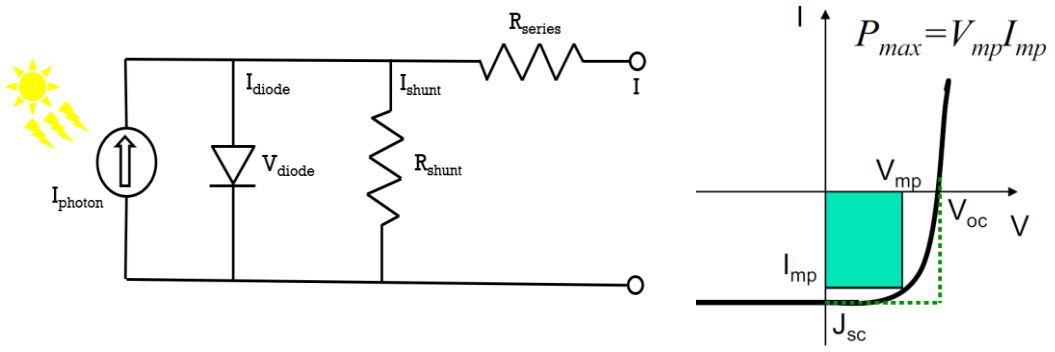


(a) (b)

Fig. 4.2 (a) Equivalent circuit model of solar cell. (b) A typical current-voltage characteristic of a solar cell.

The highest voltage obtained from a solar cell is called open circuit voltage ($V_{OC}$). It occurs when the current through the device is zero.

Efficiency

Efficiency is the most frequently used parameter to compare the performance of one solar cell with another, which is defined as the ratio of electrical output energy of solar cell to the energy of incident light. Following equation 4.1 describes the mathematical expression for efficiency of a solar cell in terms of devices' output current and voltage.

$$\eta = \frac{V_{OC} I_{SC} FF}{P_{in}} \qquad 4.1$$

Here, *FF* (fill factor) is defined as the ratio of the maximum power from the solar cell to the product of $V_{OC}$ and $I_{SC}$.

Series resistance ($R_S$) of the solar cell expected to be as low as possible and shunt resistance ($R_{SH}$) as high as possible. Series resistance mainly causes by the contact

resistance whereas shunt resistance attributed to defects, impurities, and processing errors of the device.

## 4.4 Solar cell fabrication

Pre-cut and pre-patterned ITO/glass substrates were cleaned by ultrasonication in Deconex OP121 detergent and deionized water. The substrates were dried, $O_2$ plasma treated for 7 minutes and then coated with PEDOT:PSS (Clevios™ P VP AI 4083) to form a ~35 nm thick layer. The substrates were then transferred into a $N_2$ glove box having <1 ppm of $O_2$ and $H_2O$. The precursor solutions were then spun cast on top of the ITO/PEDOT:PSS substrates at different speeds to attain different thicknesses. After coating the perovskite layers, substrates were transferred to a humidity control chamber and annealed at 100°C for 5 minutes in the air (R.H ~ 30-35%). The annealed perovskite layers were then transferred to an evaporation chamber for deposition of ~40 nm $C_{60}$, ~8 nm of BCP and ~100 nm of Al sequentially using a shadow mask. The active area of devices was calculated as 6.25 $mm^2$ from the overlap of the ITO and Al electrodes.

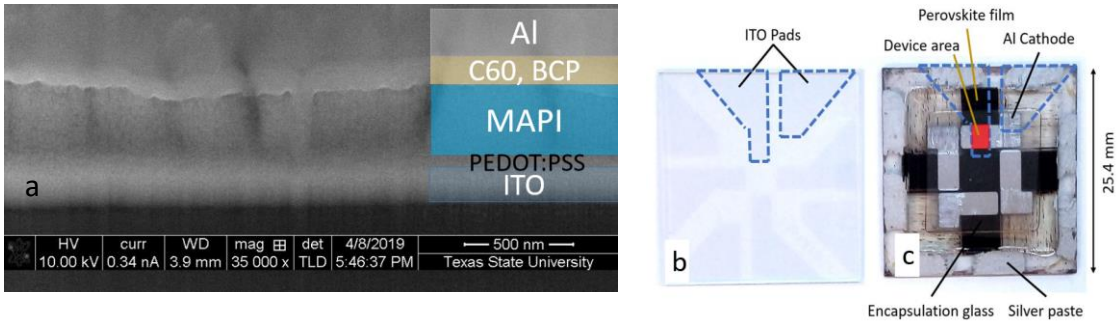


Fig. 4.3 (a) Cross-sectional SEM image of a fabricated solar cell layer stack, (b) Patterned ITO/glass 1 square inch substrate, (c) Encapsulated solar cells after fabrication.

Fig. 4.3a shows cross-sectional SEM image of a MAPI solar cell. The individual layers are labeled in the left side. As can be seen in the fig. 4.3 b, the blue-dashed enclosed areas are the ITO pads used as contacts for a single solar cell. One substrate contains four identical patterns which can accommodate four identical solar cells. Image of glass encapsulated solar cells after fabrication of all layers is shown in fig. 4.3c.

## 4.5 Result and discussion

### 4.5.1 Current density-voltage (J-V) characteristics

The current density-voltage (J-V) measurement was performed for all solar cells. It is used to compare the performance of different solar cell in terms of efficiency, FF, $V_{OC}$, and $J_{SC}$. The J-V characteristic is not only a mean to device characterization but also considered as the ultimate test of MAPI quality. Fig. 4.4 shows the current density-voltage plots of solar cells fabricated with perovskite active layers derived from different precursor ratios. The active layer thickness for the representative cells was ~ 500 nm. The photovoltaic parameters are tabulated in table 4.1.

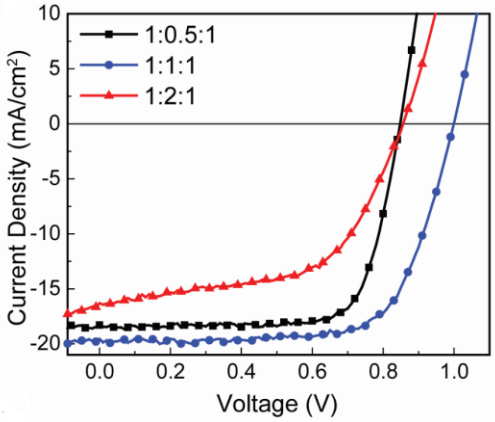


Fig. 4.4 Current density vs. voltage plot of solar cells.

Table 4.1. Photovoltaic parameters of perovskite solar cells derived from different precursor ratios.

| **Precursor Ratio ($PbI_2$: MAAc:MAI)** | **$V_{oc}$ (mV)** | **$J_{sc}$ ($mA/cm^2$)** | **FF (%)** | **PCE (%)** | **$R_s$ ($\Omega cm^2$)** | **$R_{sh}$ ($\Omega cm^2$)** |
|---|---|---|---|---|---|---|
| 1:0.5:1 | 847 | 18.29 | 75.69 | 11.74 | 5.12 | 7017.5 |
| 1:1:1 | 1002 | 21.66 | 69.10 | 15.00 | 7.35 | 3506.3 |
| 1:2:1 | 856 | 16.31 | 58.08 | 8.11 | 11.66 | 134.8 |

Among all devices, solar cells with 1:2:1 active layer exhibited the poorest power conversion efficiency (PCE) of 8.11% with open circuit voltage ($V_{oc}$) of 0.856V, short circuit current density ($J_{sc}$) of 16.31 $mA/cm^2$ and fill factor (FF) of 58.08. The devices with 1:1:1 ratio showed the best performance with PCE of 15.00% with $V_{oc}$ of 1.002V, $J_{sc}$ of 21.66 $mA/cm^2$ and FF of 69.11. Devices with 1:0.5:1 active layer showed a mediocre PCE of 11.74% with $V_{oc}$ of 0.847 V, $J_{sc}$ of 18.29 $mA/cm^2$ and highest FF of 75.69. The improved PCE in 1:1:1 and 1:0.5:1 devices arise mainly due to the increase in $J_{sc}$ and FF. The improved FF in these devices is attributed to the lower series resistance as calculated from the slope of current density vs. voltage plot of the devices. 1:1:1 devices show the best performance attributed to highest $J_{sc}$ and $V_{oc}$. The enhanced FF in 1:1:1 and 1:0.5:1 devices is attributed mainly to the significant improved shunt resistance ($R_{sh}$). The 1:2:1 devices showed a poor $R_{sh}$ of 134.8 $\Omega cm^2$ compared to 7017.5 $\Omega cm^2$ and 3506.3 for 1:0.5 and 1:1:1 devices respectively. The lower shunt resistance is attributed to current leakage which could possibly arise from poor morphology (pinholes, cracks, etc.) as seen in the SEM images.

### 4.5.2 Hysteresis in J-V curves

The difference in J-V curves for different scan direction is known as hysteresis. It has been a common problem in perovskite solar cell performance [71]. It is caused by defect-assisted trapping of carriers in the grain boundaries and interfaces [72]. To study the hysteresis of the solar cell group, the voltage scans were performed in both directions. The role of scan direction had minimal impact on the photovoltaic parameters for devices processed from all three precursor ratios. Fig. 4.5 shows the J-V characteristics of solar cell derived from all three ratio. The negligible hysteresis is observed for 1:0.5:1 and 1:1:1 ratio, that can be attributed to surface defect passivation by fullerene ($C_{60}$) layer as commonly observed in inverted perovskite solar cells [73]. Relatively higher hysteresis in 1:2:1 ratio device is caused by the large area of grain boundaries from smaller grains and possible pinholes.

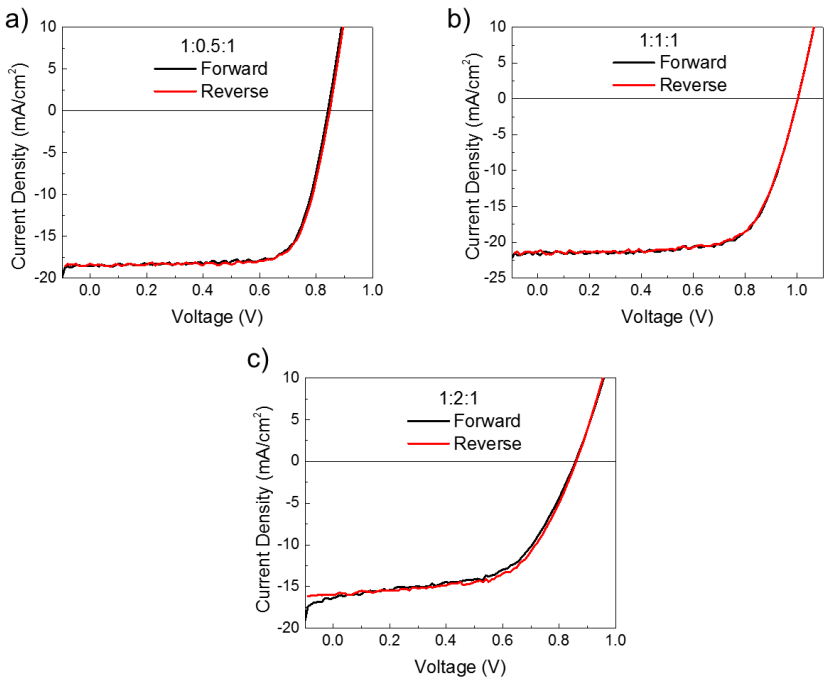


Fig. 4.5 Current density vs voltage plot under forward (short circuit → open circuit) and reverse (open circuit → short circuit) scan conditions of a) 1:0.5:1, b)1:1:1 and c)1:2:1 solar cells.

### 4.5.3 External quantum efficiency (EQE)

To study the wavelength dependent performance of the solar cell and understand the difference in current densities among the three ratios (Fig 4.4) the external quantum efficiency (EQE) spectra were measured, as shown in Fig. 4.6 a. The negligible shift in the onset of EQE was observed in all devices as supported by the similar onset of the UV-visible absorption spectra (Fig. 4.6 b).

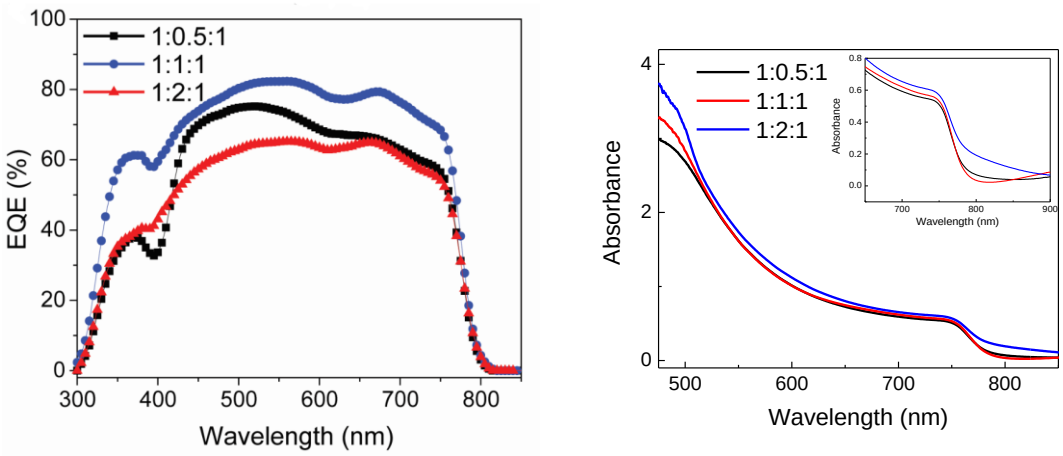


(a) (b)

Fig. 4.6 (a) external quantum efficiency (EQE) three category's solar cell, (b) UV-Visible absorption spectra of perovskite films coated from different precursor ratios. Inset is showing the magnified view of absorbance for wavelength range 650nm – 900 nm.

1:1:1 devices show the highest EQE in the absorption range of the active layer. While 1:2:1 devices showed the lowest EQE with a steady decrease in the entire absorption regime, 1:0.5:1 devices show comparatively higher EQE at lower wavelengths and lower EQE at higher wavelengths. The higher EQE is attributed to a higher charge collection in the devices in 1:1:1 solar cells. Specifically, the improvement in EQE at longer wavelengths can be attributed to enhanced charge extraction at the back interface in the 1:1:1 devices.[52] Although the integrated $J_{sc}$ values from the EQE measurements follow the same trend as the device parameters shown in fig. 4.3, a ~10% offset was observed, which could be due to spectral mismatch or shadow mask induced changes in device area.

### 4.5.4 Thickness dependent photovoltaic performance

It is also critical to understand the variation in photovoltaic parameters with the thickness, which can reveal the quality of the active layers. The change in photovoltaic parameters vs. thickness is plotted in fig. 4.7.

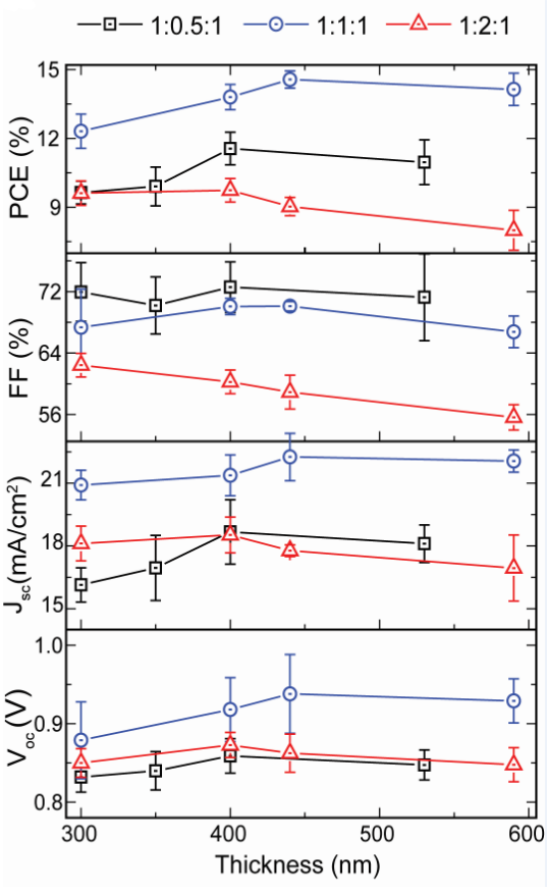


Fig. 4.7 Photovoltaic parameters vs. thickness of perovskite solar cells derived from different precursor ratios.

Different active layer thicknesses were obtained by varying the spin coating speed of the precursor solution. For 1:2:1 devices, it is clearly seen that as the active layer thickness increases from ~ 300 nm to ~ 600 nm the PCE and FF decreases. The decrease in FF is attributed to the higher series resistance of the

solar cells. The optimal thickness of the active layer was found to be 400 nm – 500 nm resulting in maximum PCE ~ 9.5% for devices with1:2:1 precursor ratio. On the contrary, devices derived from a 1:1:1 and 1:0.5:1 precursor ratio showed the opposite trend, i.e., with increasing active layer thickness the PCE improved. The improvement in PCE with a higher thickness in 1:1:1 devices due to enhanced $J_{sc}$ is indicative of higher absorption and improved charge collection. The FF in the 1:1:1 and 1:0.5:1 devices were fairly constant with increasing thickness indicative of a better quality perovskite film having a lower series resistance and leakage current. The optimal thickness for the highest PCE was found to be 400 nm - 500 nm for 1:1:1 and 1:0.5:1 devices. From these thickness dependent photovoltaic parameter trends, it can be concluded that, charge transport in 1:1:1 and 1:0.5:1 devices are superior to transport in 1:2:1 devices.

### 4.5.5 Photoluminescence

To study the grain structure induced fluctuations in carrier density and lifetime, photoluminescence (PL) measurements were performed. Integrated photoluminescence (PL) and time-resolved photoluminescence (TRPL) measurements were performed with 430 nm excitation wavelength. The excitation system (Spectra Physics) was comprised of a frequency-doubled neodymium vanadate laser pumping a mode-locked Ti: Sapphire laser to produce ~ 150 fs broad pulses at 860 nm wavelength with 80 MHz repetition rate. Pulse frequency was then chosen using a pulse selector. A second harmonic generator then produces the desired 430 nm excitation wavelength. The PL signal is collected and passed to a spectrometer with 0.64-m focal length equipped with a fast micro-

channel plate photomultiplier tube. The TRPL decay curves are obtained at an emission wavelength of 760 nm using time-correlated single photon counting calibrated to span a 2 ns measurement range. The instrument response of the TRPL system was ~ 2 ns. The laser spot size at samples is ~ 100 µm. Fig. 4.8 a shows the integrated PL spectra of perovskite films derived from 1:0.5:1, 1:1:1 and 1:2:1 precursor mixing ratios.

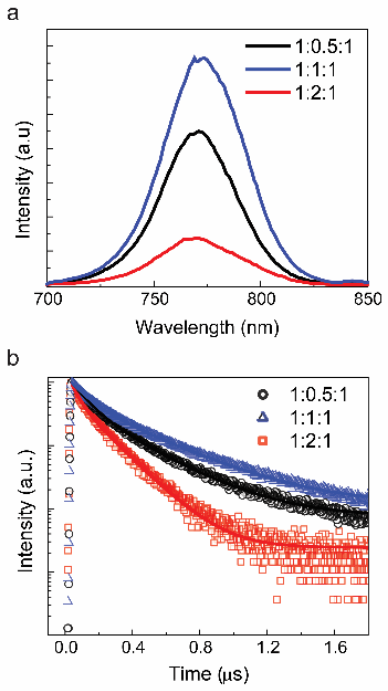


Fig. 4.8 (a) Integrated photoluminescence and (b) time resolved photoluminescence (symbols represent data and lines represent bi-exponential fit) of annealed perovskite films derived from different mixing ratios.

With the same excitation, the PL intensities obtained for films derived from 1:1:1 and 1:0.5:1 precursor ratio is much higher than 1:2:1 films. The enhanced PL in 1:1:1 is indicative of lower trap assisted (non-radiative) and higher band to band (radiative) recombination. Thus the 1:2:1 films have lower PL intensity due to the

higher density of trap states, which lead to higher trap-assisted recombination. As seen in the SEM images, 1:2:1 samples have smaller grains and higher density of grain boundaries, which act as non-radiative recombination centers.[56] The trend in peak PL intensity is in line with the $J_{sc}$ trend observed in photovoltaic devices. Further, time-resolved photoluminescence (TRPL) measurements were performed to evaluate the carrier lifetime in these films. The TRPL data were fit with a second-order exponential decay equation to find the fast recombination ($\tau_1$) and slow recombination ($\tau_2$) lifetimes. Previous reports of TRPL studies on perovskite films have shown that the fast decay is due to surface and grain boundary defects and the slow decay arises from bulk defects within the grain interiors.[74],[75] The 1:2:1 films showed $\tau_1$ = 46 ns and $\tau_2$ = 165 ns. In contrast, the 1:1:1 and 1:0.5:1 films showed much higher lifetime values compared to the 1:2:1 films. The $\tau_1$ times were 94 ns and 96 ns and the $\tau_2$ times were found to be 293 ns and 361 ns for the 1:0.5:1 and 1:1:1 films respectively. Higher carrier lifetimes for 1:1:1 and 1:0.5:1 films indicate slower trap-assisted recombination kinetics than that for the films derived from the 1:2:1 precursor ratio. Similar fast decay dynamics for 1:0.5:1 and 1:1:1 indicated lower surface and grain boundary defects in the films consistent with the SEM analysis. The highest $\tau_1$ and $\tau_2$ lifetimes in the 1:1:1 films indicated superior radiative recombination kinetics due to the suppressed surface and bulk defect density. Further, the comparable lifetimes of 1:0.5:1 films with 1:1:1 films indicate that relatively lower $V_{oc}$ values are observed in 1:0.5:1 devices which could be arising from the higher bulk recombination in the 1:0.5:1 derived

perovskite films.[73] However, the origin of high FF in 1:0.5:1 films is still not clear and needs to be further investigated.

### 4.5.6 Champion device with commercial MAAc

Until available commercially, at the beginning of this research, MAAc was synthesized in the organic semiconductor lab of Texas State University using the custom-made setup as described in section 3.2.1. Once available, commercial MAAc from the Greatcellsolar company was adopted for device fabrication. The best processing parameters were used for fabrication with the 1:1:1 MAI:MAAc:$PbI_2$ ink formulation. Using commercial MAAc, a 16.46% champion efficiency was achieved with FF of 76.67, $V_{OC}$ of 0.95 V, and $J_{SC}$ of 22.7 mA/cm$^2$. Fig. 4.9a shows the J-V curve for both scan directions of the champion solar cell. Note that, no hysteresis is observed in the J-V plot.

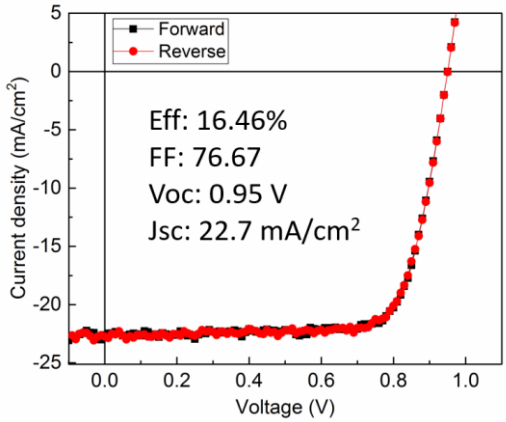


(a)

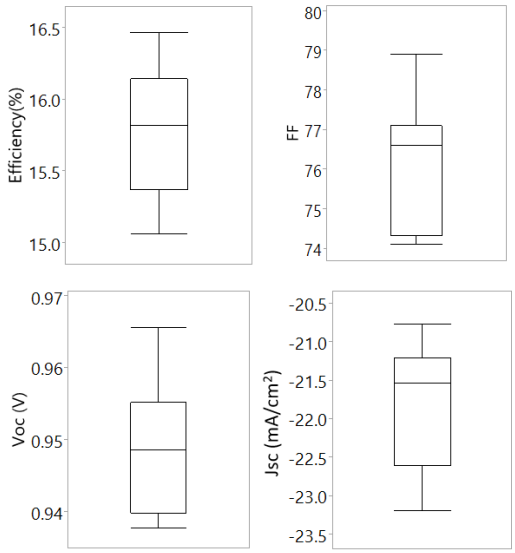


(b)

Fig. 4.9 (a) J-V curve of champion MAPI solar cell. (b) Statistics of 15 solar cell performance using commercial MAAc.

In order to study the reproducibility of the fabrication process, batch processing was conducted aiming 16 solar cells employing identical process parameters. One of the 16 devices failed. The other 15 devices exhibited the desired performance with a very small device to device variation. The performance statistics of 15 devices is graphically presented in fig. 4.9 b and tabulated in the following table 4.2.

Table 4.2 Performance statistics of 15 MAPI solar cell fabricated following identical process parameters.

| | **Eff[a] (%) FW[b]** | **Eff (%) RV[c]** | **$V_{OC}$ (V) FW** | **$V_{OC}$ (V) RV** | **$J_{SC}$ (mA/cm$^2$) FW** | **$J_{SC}$ (mA/cm$^2$) RV** | **FF FW** | **FF RV** |
|---|---|---|---|---|---|---|---|---|
| Mean | 15.64 | 15.55 | 0.95 | 0.95 | -21.79 | -21.82 | 75.75 | 75.16 |
| Std Dev | 0.69 | 0.73 | 0.008 | 0.008 | 0.76 | 0.61 | 2.30 | 2.55 |
| Range | 2.85 | 2.74 | 0.03 | 0.03 | 2.43 | 1.80 | 9.16 | 9.88 |
| Max | 16.46 | 16.44 | 0.97 | 0.96 | -20.76 | -21.1 | 78.91 | 78.1 |

[a]Eff is for efficiency, [b]FW is for forward scan and [c]RV is for reverse scan

Clearly, the average performance of the MAPI solar cell was ~15.50%, which is higher than our lab made champion MAAc device. Only $V_{OC}$ decreases slightly. All other parameters, such as efficiency, $J_{SC}$, and FF increases. These statistical data are suggesting excellent reproducibility of the device fabrication with very high performance.

### 4.5.7 Performance comparison with other deposition techniques

Table 4.3 enlisted the reported performances of solar cells for different synthesis technique of perovskite with generic architecture "**transparent electrode/PEDOT: PSS/perovskite/ETL/metal electrode"** which is similar to

our cell architecture. Most of them used MAPI as the absorber layer. Two of them reported hybrid halide perovskite. Evidently, MAAc precursor based perovskite solar cell exhibits superior performance than $PbAc_2$ and $PbCl_2$ precursor based counterpart. However, the two-step deposition and hot casted perovskite devices are shown to have better performance at the expense of additional complexity. Two-step perovskite deposition method requires an extra processing step and more optimization parameters. On the other hand, hot casting requires maintaining both solution and substrate temperature at the desired point for the optimum film, which is unsuitable for scalable reproduction. MAAc based synthesis technique ensure simplicity of process with the realization of high-quality film.

Table 4.3 Solar cell performances with generic architecture *"transparent electrode/PEDOT: PSS/perovskite/ETL/metal electrode"* for different perovskite deposition techniques.

| Deposition method | Device architecture | $V_{oc}$, V | $J_{sc}$, mA/cm$^2$ | FF, % | PCE, % | Ref. |
|---|---|---|---|---|---|---|
| $PbCl_2$ precursor | ITO/PEDOT:PSS/ $CH_3NH_3PbI_{3-x}Cl_x$ /$PC_{61}BM$)/$C_{60}$)/Ag | 0.92 | 17.5 | 73 | 11.8 | [76] |
| $PbAc_2$ precursor | ITO/PEDOT:PSS/$CH_3NH_3PbI_3$/PCBM/Ba-Ag | 0.954 | 18.8 | 69.7 | 12.5 | [40] |
| Two-step with polar solvent additive | ITO/PEDOT:PSS/ $CH_3NH_3PbI_xCl_{3-x}$ /$PC_{61}BM$/BCP/Ag | 1.03 | 23.4 | 79.6 | 19.2 | [77] |
| Solvent engineering | ITO/PEDOT:PSS/ $CH_3NH_3PbI_3$/PCBM/Al | 0.86 | 20.1 | 60.87 | 10.44 | [78] |
| Anti-solvent | ITO/PEDOT:PSS/ $CH_3NH_3PbI_3$/ETL/Ag | 0.84 | 17.11 | 75 | 9.88 | [79] |
| Hot casting | FTO/PEDOT:PSS/perovskite/PCBM/Al | - | - | - | ~18 | [72] |
| MAAC precursor (1:1:1) | ITO/PEDOT:PSS/$CH_3NH_3PbI_3$/$C_{60}$/BCP/Al | 0.95 | 22.7 | 76.67 | 16.46 | this work |

### 4.5.8 Towards Shockley-Queisser limit

Fig. 4.10 shows the current ratio Jsc/$J_{SQ}$ versus the product of Voc and FF fractions (FF*$V_{oc}$/$FF_{SQ}$*$V_{SQ}$) for champion MAPI solar cell of this research and the theoretical Shockley-Queisser maximum point. The ideal goal is to achieve the S-Q point performance. The position of current point relative to ideal point provides us the direction where to focus for improvement. Current position is (0.61, 0.89), which means our device is performing very good in terms of current generation. We have much room for improvement of open circuit voltage.

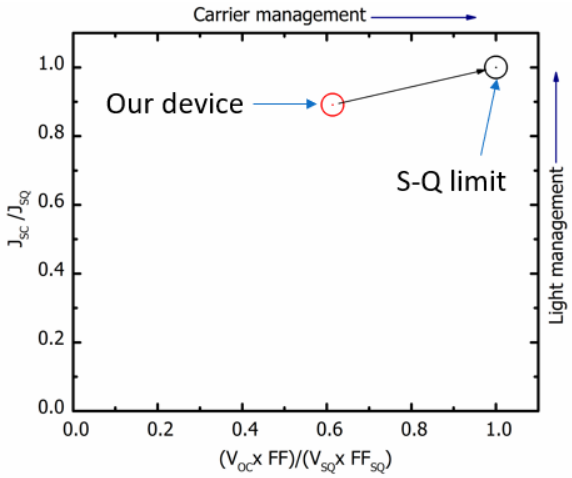


Fig. 4.10 Current density ratio Jsc/$J_{SQ}$ versus the product of Voc and FF fractions (FF*$V_{oc}$/$FF_{SQ}$*$V_{SQ}$) for champion MAPI solar cell of this research and the theoretical Shockley-Queisser maximum point.

The reason for low open circuit voltage can be a combination of bimolecular recombination in the MAPI absorber layer and energy level difference with carrier transport layers. The temperature dependent measurements of chapter 6 reveals both trap assisted and bimolecular carrier recombination occurring in the MAPI solar cell. Bimolecular recombination is particularly responsible for low Voc.[80] Voc is also

depends on the energy difference between HOMO level of MAPI and HTL. If the MAPI layer is fixed as absorber, selection of HTL to minimize the gap with MAPI HOMO level can help to improve the Voc.[81] Adoption of HTLs with desired energy level could be an effective future study to improve Voc as well as PCE of MAPI solar cell.

## 4.6 Perovskite light emitting diode (PeLED)

To ensure the compatibility of the discussed one-step method for other halides, we fabricated perovskite light emitting diodes (PeLED) with $CH_3NH_3PbBr_3$ as the emissive layer. Bromide based perovskites have shown to be promising for light emission due to their higher exciton binding energy compared to other halide based perovskites.[75],[82]

### 4.6.1 Light Emitting Diode Fabrication

Pre-cut and pre-patterned ITO glass substrates, samples were cleaned as described before for solar cell fabrication and coated with PEDOT:PSS. The precursor solution composed of 1:1:1 and 1:2:1 molar ratio of $PbBr_2$:MAAc:MABr were spun coat at 3000 rpm to achieve a 200 nm thick layer. Unlike the iodide-based perovskites, bromide-based perovskite films coated from 1:0.5:1 ratio possessed a very rough morphology and showed no electroluminescence and hence was not considered for comparison. The substrates were then annealed at 60°C for 60 mins in the air (R.H. ~ 35 - 45%). Following the annealing process, the perovskite substrates were transferred to the evaporation chamber for deposition of 40 nm BPhen, 7.5 nm LiF, and 100 nm of Al sequentially using a shadow mask.

### 4.6.2 Result and discussion

The device structure of PeLEDs is shown in fig. 4.11a. PEDOT:PSS and BPhen/LiF were used hole and electron injection layers, respectively. The emissive layers were coated in a similar fashion to that iodide based perovskite thin films with $PbBr_2$:MAAc:MABr molar ratio as 1:2:1 and 1:1:1. The photographs of fig. 4.11a shows the emission of PeLEDs from 1:1:1 and 1:2:1 ratio when biased at 5V. It is clearly seen that 1:1:1 PeLEDs show much brighter and intense emission of green light.

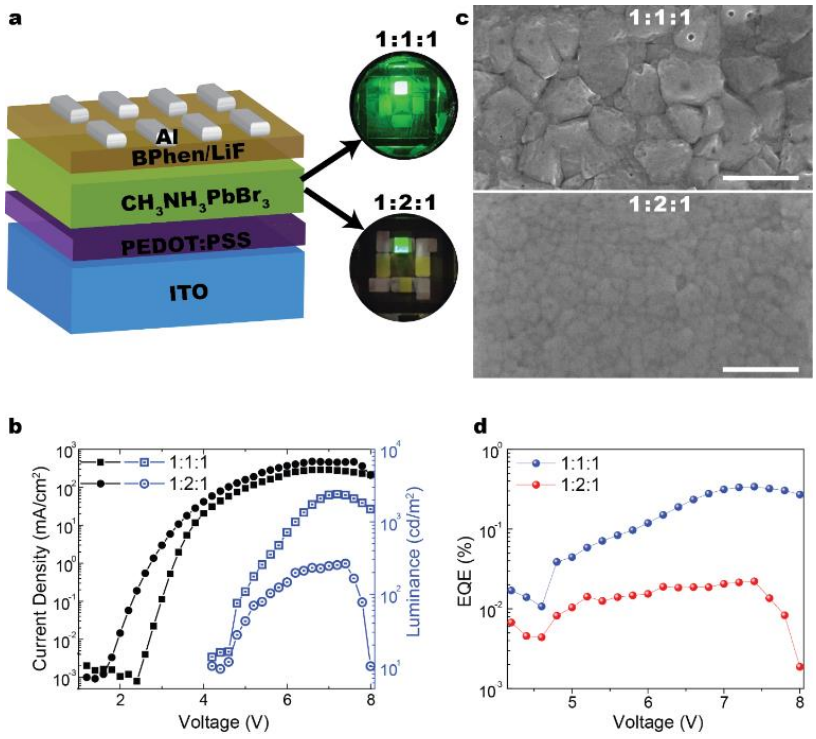


Fig. 4.11 (a) Device schematic of perovskite light emitting diodes (PeLEDs) with photographs of working PeLEDs at 5V bias, (b) current density-voltage-luminance plot (d) scanning electron microscopic images and (d) external quantum efficiency vs. input voltage of PeLEDs derived from different mixing ratios. Scale bar in SEM images represents 500 nm.

Fig. 4.11 b shows the current density-voltage-luminance (J-V-L) plots of PeLEDs fabricated with 1:1:1 and 1:2:1 precursor ratio. Both devices show a diode behavior with a turn on voltage ~ 4.5V. While the current density values are similar, 1:1:1 devices show an order of magnitude higher luminance than the 1:2:1 PeLED device. Similar to iodide-based films, higher luminance in 1:1:1 devices could be attributed to higher band-to-band radiative recombination. The lower luminance for 1:2:1 devices, on the other hand, can be due to higher trap induced recombination. The higher traps are attributed to higher defective regions such as grain boundaries as observed in FESEM images shown in Fig. 4.11 c. 1:1:1 films showed larger grains (300 nm – 500 nm) compared to 1:2:1 films which have grain sizes ranging from 50 nm – 100 nm. Due to the presence of smaller grains and higher density of grain boundaries, trap-assisted recombination is more dominant in 1:2:1 devices. Hence as seen in fig 4.11d, the EQE of 1:1:1 devices were an order magnitude higher than 1:2:1 devices. The maximum obtained EQE were 0.02% and 0.34% at 7.4V for 1:2:1 and 1:1:1 devices respectively. While the relative changes in device results were remarkable, the observed performance is still lower than the recent literature reported values. The observed photovoltaic and luminous efficiencies can be improved further by process optimization[58], interface engineering[59], and appropriate halide/cation doping.[61] Using this facile method of film deposition and growth, we anticipate that future efforts will be extended to other mixed cation and halide perovskites for efficient optoelectronic devices.

## 4.7 Conclusion

In conclusion, considering the film characterization data, solar cell and PeLED performances, MAAc based perovskite synthesis is a single step, the scalable and reproducible technique for efficient optoelectronic device fabrication compared with con-current methods under practice.

From the effect of precursor ratio (1:0.5:1, 1:1:1 and 1:2:1 of $PbI_2$:MAAc:MAI) on the growth of perovskite films and optoelectronic performances, it was found that that films derived from higher MAAc ratio (1:2:1) consisted of precursor intermediate phase predominantly. When the MAAc ratio was equimolar or lower to $PbI_2$ molar ratio (1:1:1 and 1:0.5:1), nucleation and crystallization of perovskite phase occurred during spinning. Photovoltaic devices fabricated with 1:1:1 and 1:0.5:1 precursor ratios showed enhanced power conversion efficiency compared to 1:2:1 devices.

Investigation of equimolar methylammonium acetate route compatibility with bromide-based perovskites for electroluminescent devices also suggested that perovskite LEDs fabricated from equimolar (1:1:1) precursor ratio showed enhanced electrical to optical performance compared to devices processed from 1:2:1 ratio. This study provides insight on the critical parameters of the growth mechanism for large perovskite grains with smooth and compact morphology. Further, it also shows strong potential for scalability due to facile deposition technique for large scale and high throughput coating process.

# 5. TEMPERATURE AND LIGHT INTENSITY DEPENDENT STUDY OF SOLAR CELL

## 5.1 Introduction/literature review

Despite the competitive photovoltaic efficiency and effort in improving the performance, the current challenges are also associated with the poor material's stability, which is becoming a key obstacle in the commercialization process of MAPI solar cells along with scalability and toxicity.[83]–[85] It is well known that halide perovskite deteriorates mostly in a humid environment [86], upon ultra-violet light exposure [87], [88], and in oxygen environments [89], [90]. Besides, the temperature is an important parameter on the device stability.[91] Temperature effect can be seen either during device fabrication or the device operation under varying temperature. Typically, in solution processed perovskite film growth, the annealing scheme is one of the major requirements to form crystals in the films and evaporate the residue solvent. Interestingly, perovskite itself is susceptible to damage/phase change via thermal annealing.[92] Under sun illumination and at high temperature, the solar cell performance affected by the phase transition behavior (tetragonal to cubic phase) and chemical instability.[83] While unclear, the microscopic origin and detailed degradation process under extensive research either *via* theoretical calculation or through experimental evaluation.[93]–[100]

Besides the device stability, recombination of the generated charge carrier has been identified as a major loss mechanism in solar cell and need deeper insight to understand the possible mechanism or responsible factors which determining the resultant PV performance.[101], [102] The temperature and illumination intensity dependent short-circuit current density ($J_{SC}$), and the open-circuit voltage ($V_{OC}$) analysis are suitable tools to analyze the recombination.[103], [104] In this quest, the device performance analysis

with variable temperature and illumination level are valuable to understand the stability, kinetics of charge carrier recombination, and correlated device physics particularly

In this chapter, the dependence of PV performance under a wide range of temperature (40 – 430K) and illumination intensity ($1\times10^{-3}$ – 56.6 mW/cm$^2$) were studied. While the phase transition and other aspects of the PV device parameters investigated but the primary motivation in this research is the recombination analysis. Open-circuit voltage ($V_{OC}$) and short-circuit current density ($J_{SC}$) as a function of light intensity level and temperature were utilized as a tool for recombination study. Using temperature-dependent CV measurements, the dielectric constant of MAPI and its temperature dependency was also investigated. The results and analysis provide insight – useful for further understanding of developing high efficiency and stable devices based on perovskites.

## 5.2 Experimental

For temperature and light intensity dependent study, MAPI solar cells were fabricated using 1:1:1 MAI: MAAc: $PbI_2$ ink formulation, as described in chapter 4, section 4.4. The temperature dependent dark and light current density-voltage (J-V) characteristics were performed using a closed-cycle helium (He) cryogenic probe-station in the temperature range 40 - 430K. Note that, the temperature dependent measurements were performed from low to high temperature. For the light J-V characteristics, a calibrated laser-driven light source[105] that can generate illumination intensity up to 56.6 mW/cm$^2$ in the spectral regime 400 nm – 850 nm were used. Illumination intensity was varied from ~$1\times10^{-3}$ to 56.6 mW/cm$^2$ using a series of calibrated neutral density filters. The carrier density was estimated using capacitance-voltage (CV) measurement at

dark and in the frequency range 100 – $10^6$ Hz. The ac-signal amplitude was used in CV measurement was 30 $mV_{rms}$ while the dc-bias was varied from -1.0V to1.2V. Drive level capacitance profiling (DLCP) was also performed. The ac-modulation signal was varied between 10 – 200 $mV_{rms}$ along with the dc-voltage sweep as in CV method. The temperature dependent dielectric constant (κ) of the perovskite absorber was measured by the CV method at zero bias at several frequencies $f$ = 1, 10, 100 kHz using a capacitor-like structure of perovskite thin film sandwiched between ITO and Al electrodes.

## 5.3 Illumination dependent J-V characteristics

Before starting the temperature and illumination intensity dependent J-V study, the dark and light current J-V characteristics of the representative MAPI solar cell was measured at room temperature under the standard one sun illumination condition using an Oriel ABA sun simulator with an AM 1.5G filter which is calibrated to a 100mW/$cm^2$. The device parameters are: $V_{OC}$ = 0.819 V, $J_{SC}$ = 24.9 mA/$cm^2$, FF = 66.5%, and η = 13.6% (fig. 5.1). It is worth mentioning that, this phase of the research was done before the adoption of the commercial MAAc. For this reason, the efficiency of the representative solar cell is 2-3% below the best-reported lot.

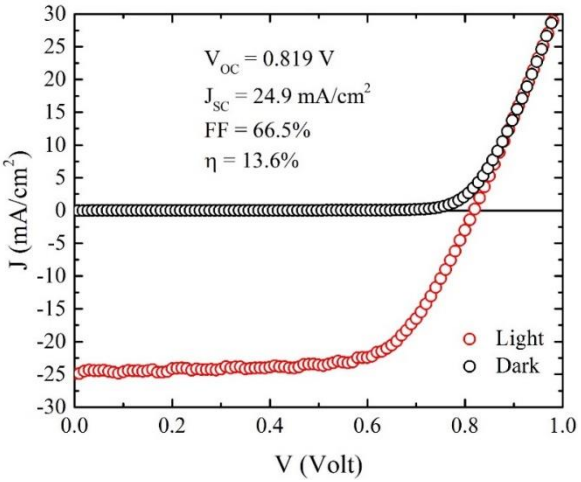


Fig. 5.1 The dark and light (Intensity: 100 mW/cm$^2$) J-V characteristics of the MAPI solar cell. The device parameters are in the figure.

J-V characteristics of the temperature (40 – 430K) and illumination intensity ($1\times10^{-3}$ – 56.6 mW/cm$^2$) dependent device are presented fig. 5.2. At room temperature, illumination intensity ($1\times10^{-3}$ – 56.6 mW/cm$^2$) dependent J-V characteristics are shown in fig. 5.2(a). $V_{OC}$ found to be very sensitive to illumination intensity level. For the intensity range $1\times10^{-3}$ – 56.6 mW/cm$^2$, the $V_{OC}$ was changed from 0.214 - 0.839 V. Under 56.6 mW/cm$^2$ illumination, the temperature dependent (40 – 430K) J-V characteristics (as in fig. 5.2b) shows the $V_{OC}$ varies between 0.581 V (T = 430K) – 0.921 V (T = 200K). Lowest $V_{OC}$ (0.036V) observed at T = 430K at an illumination level of $9.33\times10^{-4}$ mW/cm$^2$. Highest $V_{OC}$ observed is 0.921 V at 190K under 56.6 mW/cm$^2$ illumination. The $J_{SC}$, under 56.6 mW/cm$^2$ illumination, varies between 0.54 – 16.75 mA/cm$^2$ in the temperature range 40 – 330K and started to decrease as temperature increases towards 430K ($J_{SC}$ = 0.56 mA/cm$^2$). Note that, the $J_{SC}$ at 300K and under 100 mW/cm$^2$ illumination (standard solar simulator) is higher than that of our measurement, which is due to lower intensity (56.6 mW/cm$^2$).

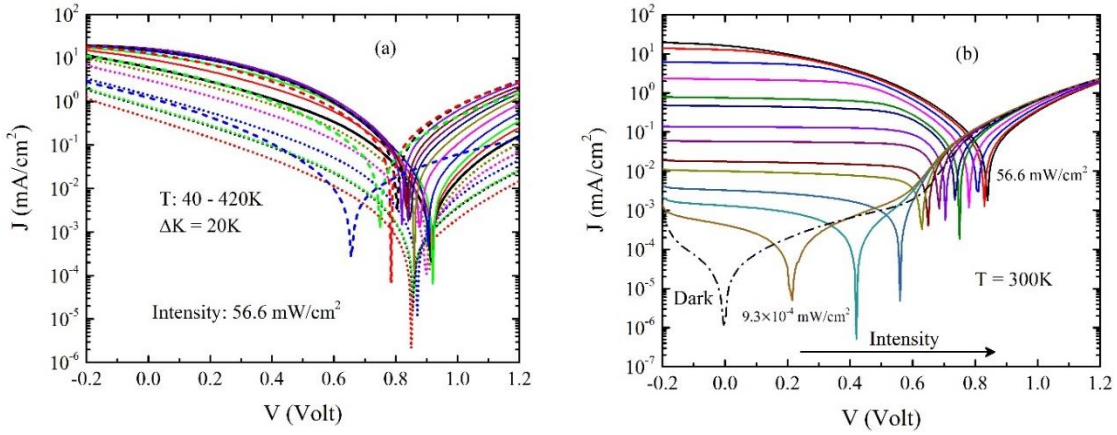


Fig. 5.2 Temperature and illumination intensity dependent J-V characteristics: (a) with variable temperature (40 – 420K, ΔT = 20K – dotted limes represent the temperature limit 40 -140K, solid lines represents 160 – 340K, and dash lines represents 360 – 420K) under 56.6 mW/cm$^2$ illumination intensity, and (b) Dark (black dotted line) and at various intensity ($1\times10^{-3}$ – 56.6 mW/cm$^2$) at 300K.

Temperature and illumination intensity dependent $V_{OC}$ and $J_{SC}$ can be better-visualized using two-dimensional representation, as shown in fig. 5.3 (a) and (b) respectively. This graph shows the $V_{OC}$ is sensitive to all intensity level and temperature while $J_{SC}$ is only sensitive to the high-intensity (> 10 mW/cm$^2$) and high temperature (>150K) regime. It is noteworthy; there are two known phase transition in MAPI in the temperature window 40 – 430K used in this study and the expected phase transition sequence is: Orthorhombic – 162K – Tetragonal – 330K - Cubic.[97], [106]–[108] The changes of $V_{OC}$ and $J_{SC}$ is related to the phase transition behavior can be clearly seen with temperature variation at a fixed intensity. The changes in $V_{OC}$ and $J_{SC}$ inside the phase, say tetragonal phase, can be associated with intrinsic instability. Recently, first-principle calculation shows that the room-temperature tetragonal phase of MAPI is thermodynamically unstable concerning the phase separation of $CH_3NH_3^+$ $PbI_2^-$

independent of humidity or oxygen in the atmosphere.[109] This dissimilarity could be due to the two different space groups *I4/mcm* and *I4cm* in the tetragonal structure of MAPI.[109], [110]

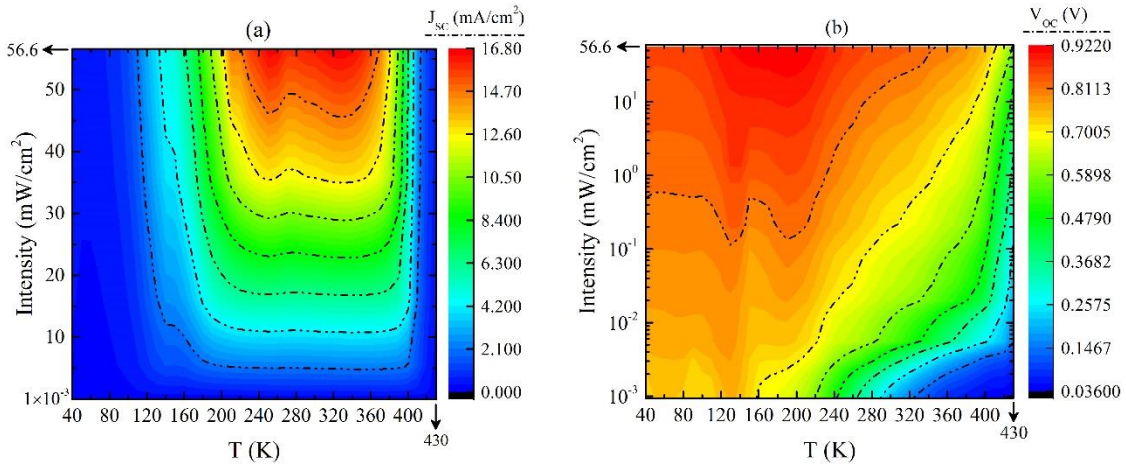


Fig. 5.3 Two-dimensional plots of $V_{OC}$ and $J_{SC}$ as a function of temperature (K) and illumination intensity (mW/cm$^2$). The color-code shows the values of $V_{OC}$ (V) and $J_{SC}$ (mA/cm$^2$).

## 5.4 Carrier recombination study

The temperature and illumination-dependent open-circuit voltage ($V_{OC}$) analysis is a well-established methodology to explore the non-radiative recombination, i.e., Shockley-Read-Hall (SRH) type. This method is utilized in various heterojunction based inorganic solar cells such as CdTe, CIGS, and Silicon.[111] The advantage of focusing on $V_{OC}$ point in J-V characteristics is that at $V = V_{OC}$, all photo-generated charge carriers recombine. Also, this allows negating the effect of series resistance, as there is no net current flow in the device. Further, $V_{OC}$ – T dependent study predicts the location in the absorber where the majority of generated charge carriers recombine.[112]

At, fixed illumination intensity (56.6 mW/cm$^2$), the temperature dependence of $V_{OC}$ is shown in the fig. 5.4 – marked with phase transition regimes. Both theoretically, and experimentally it is observed (for organic, organic, and perovskite solar cells) that the $V_{OC}$ is linear in T in the temperature regime near room temperature and the linear fitting and its extrapolation to T = 0K is the measure of activation energy ($E_a$) of dominant recombination[112]–[114] whose expression is given by equation 5.1. [115]

$$E_a = \frac{E_g}{q} - \frac{nk_BT}{q} ln\left(\frac{J_{00}}{J_{SC}}\right) \qquad 5.1$$

Here, $E_g$ is the bandgap, $J_{00}$ pre-factor for the reverse saturation current ($J_0$) which depends on the specific recombination mechanism, and *n* is the diode ideality factor. Note, the open circuit voltage, $V_{OC}$, is the measure of quasi-Fermi level separation under illumination and the extrapolated $E_a$ value is a measure of maximum attainable quasi-Fermi level separation. If the value of $E_a$ is same as perovskite absorber bandgap ($E_g$), then one would say the recombination is dominated in the semiconductor bulk. In contrary, if $E_a$value is lower than $E_g$value, then it is straightforward to say that the majority of generated electrons and holes recombine in the depletion regime and PEDOT:PSS/Perovskite interface.[113] For 56.6 mW/cm$^2$ illumination, 1.18 eV recombination activation energy, $E_a$, was observed (as shown in fig. 5.4).

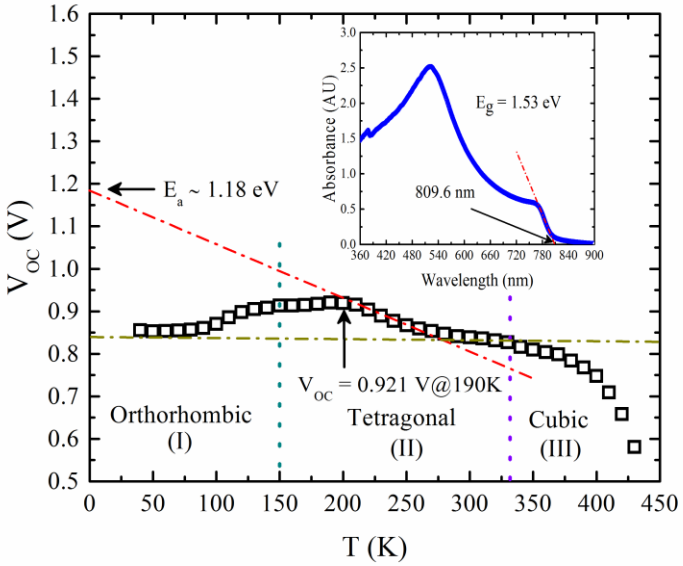


Fig. 5.4 The dependency of $V_{OC}$ on the temperature at an illumination intensity of 56.6 mW/cm$^2$. The activation energy of the dominant recombination is $E_a$=1.18 eV, which is estimated by extrapolating the $V_{OC}$ data to T = 0K. The inset shows the UV-Vis spectra of perovskite thin films of thickness 320 nm – show the optical bandgap of 1.53 eV.

The optical bandgap of MAPI was used in the device is 1.53 eV estimated via UV-Vis absorption spectroscopy – as shown in the inset of Fig. 5.4. This value is close to the HOMO and LUMO separation of the MAPI. Estimated recombination activation energy $E_a$ = 1.18 eV is much lower than optical bandgap ($E_g$ = 1.53 eV) of perovskite absorber tell that most generated carriers recombine at the PEDOT:PSS/MAPI interface. Improvement of material quality and the interface properties is required, which may lead to even higher efficiency than that of the current device (η ~ 13.6%) utilized in this report. Note that the $V_{OC}$ – T plot in fig. 5.4 is at 56.6 mW/cm$^2$ and not under one sun illumination (100 mW/cm$^2$). So, one should expect higher $E_a$ value and recombination in

perovskite bulk. However, the $V_{OC}$ – T plots at several intensities (as in fig. 5.5) shows $E_a$varies from 1.11 eV – 1.18 eV in the intensity range 0.02 – 56.6 mW/cm$^2$. Although the current facility of Texas State University can go maximum of 56.6 mW/cm$^2$ illumination to perform this characterization, the slow variation of $E_a$ with intensity suggest the existence of considerable interface recombination.

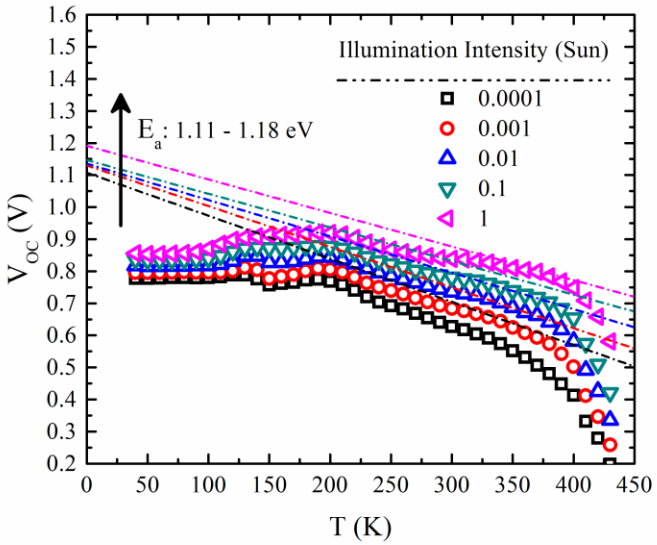


Fig. 5.5 Temperature-dependent $V_{OC}$ at various illumination intensity, which shows the recombination activation energy of dominant recombination is in the range of 1.11 – 1.18 eV.

Under illumination, most of the charge carriers generated at short depth within the 320 nm of MAPI absorber film. So, the recombination at PEDOT:PSS/MAPI interface and in the depletion region is highly possible. Khadka et al. investigated a comparative analysis with encapsulated perovskite solar cells with and without degradation where they found 0.98 eV and 1.4 eV recombination activation energy, respectively.[112] The solar cells used in this research was encapsulated to minimize degradation. Test of the

same device after preserving in the glove box at room temperature for two weeks exhibited negligible deviation in performance. The other possibility of deterioration of the devices is the low-temperature effect and the instability in the orthorhombic phase.[116] The device was intentionally kept in the temperature range of orthorhombic and cubic phase, and performance was measured again at room temperature to test the reversibility of the phase. Minimum variation in performance is observed, which implies the device can recover its phase change.

Generally, $V_{OC}$ – T plot gives information on the location where the majority of recombination happening with the activation energy $E_a$. However, there are three major types of recombination: trap-assisted or defect mediated recombination (Shockley-Read-Hall; SRH type)[117], bimolecular recombination[118], and monomolecular recombination[119]. The bimolecular recombination refers to the recombination of free electrons and holes in the photoactive layer, while the monomolecular recombination refers to a first-order process including the geminate recombination of a bound electron–hole pair before dissociation, and the SRH recombination at the shallow traps created by defects and impurities in the interfacial layer.[120]

Previous analysis uncovers the types of recombination in the device utilized in this report. So, the further emphasis was given on the illumination intensity (mW/cm$^2$) dependent $J_{SC}$. In general, $J_{SC}$ and intensity ($I_0$) follows a power law relationship, i.e., $J_{SC} \sim {I_0}^{\alpha}$ and $\alpha$ value of predicts the types of recombination. The power exponent expected to be $\alpha$ ~1 if first-order monomolecular (either trap-assisted or geminate) recombination is dominating. On the other hand, if the second order bimolecular

recombination process plays significant role, then we should observe the saturation of $J_{SC}$ with the intensity and power exponent should approach lower value.

Fig. 5.6a represents the $J_{SC}$ vs. intensity plots on a double logarithmic graph. It is observed that $J_{SC}$ is not linear for the entire intensity window. Instead, illumination intensity dependent $J_{SC}$ can be separated into two regimes below and above the intensity of 0.12 mW/cm$^2$ to explore the trend by fitting. Fig. 5.6 b and c represent double-logarithmic representation of $J_{SC}$ and intensity in the lower and higher intensity regions respectively for the temperature window T: 50 – 400K, $\Delta T = 50K$. The dependency of the slope (α) on temperature (T) is shown in the 5.7. The α is different for the two different intensity regimes. Evidently, the trend of the plot for both intensities has changed around the known phase transition temperatures (~162K and ~330K). Especially, in the temperature window below 162K, the change of α is abrupt and follow the opposite trend. Referring fig. 5.3, the Jsc of the device was also very poor. This indicates the poor carrier generation and reduced functionality of the orthorhombic phase perovskite device at the temperature below ~162K. It has been reported that at the temperature range140 - 170 K, both tetragonal and orthorhombic phase co-exists.[118] Thus, no conclusion was drawn about recombination. Noteworthy, this is highly unlikely operational temperature regime for a solar cell in real life on the earth application. For the rest part of the temperature widow (163K – 400K), the value of α is consistent and changed gradually. In the low-intensity regime (< 0.02 mW/cm$^2$), the exponent (α) varies between 1 and 1.1 – dictates trap-assisted recombination. On the other hand, in the intensity regime (> 0.02 mW/cm$^2$), α value ~0.85, and suggest bimolecular recombination. Bimolecular recombination in the higher intensity is possible due to higher generation. Overall, the

presence of both bimolecular and trap-assisted recombination process are possible in ITO/PEDOT:PSS/MAPI/$C_{60}$/BCP/Al architecture solar cell. To be noted, at short-circuit condition, there is a developed built-in potential which assist the photogenerated carriers to swept out and hence charge collection at the electrode contacts. Because of this, the intensity-dependent $J_{SC}$ is not sensitive enough to traps of any amount and whereas intensity dependent $V_{OC}$ analysis is.[104]

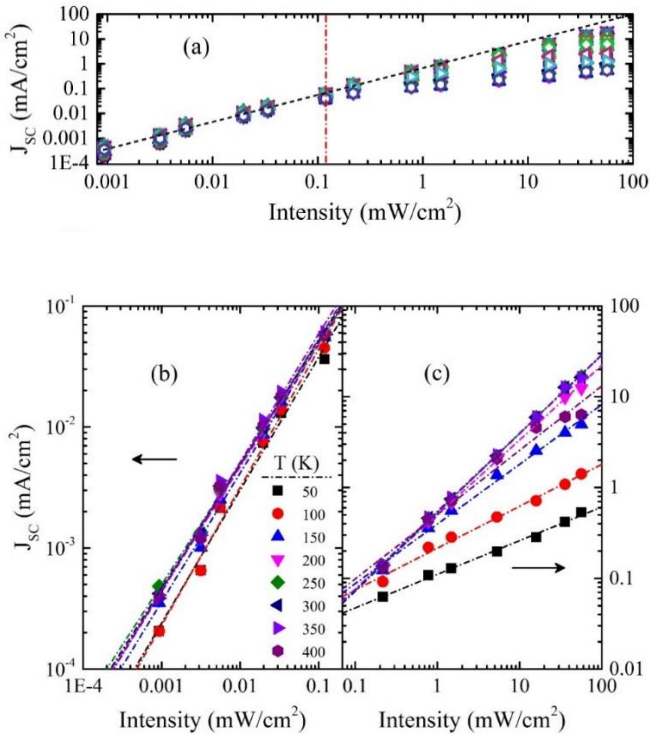


Fig. 5.6 (a) Illumination intensity (mW/cm$^2$) dependent $J_{SC}$ (mA/cm$^2$), Linear fitting of $\log_e$ [$J_{SC}$ (mA/cm$^2$)] vs. $\log_e$ [Intensity (mW/cm$^2$)] in the lower intensity - (b) and higher intensity - (c).

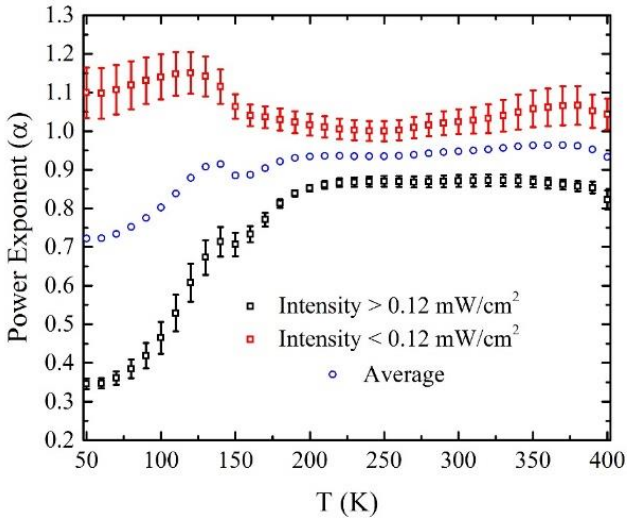


Fig. 5.7 The variation of the power exponent factor (α) in $J_{SC} \sim {I_0}^{\alpha}$ with the temperature T.

In further understanding the recombination losses of photo-generated carriers (in account of the limitation of intensity dependent $J_{SC}$ analysis – as stated earlier) during device operation, the presentation of $V_{OC}$ as a function of illumination light level is essential. The irradiation dependent $V_{OC}$ analysis is a versatile diagnostic tool to interrogate the influences of traps in the recombination process.[121] The intensity dependent $V_{OC}$ expression can be written as,

$$V_{OC} = \frac{k_B T}{q} \ln\left({I_0}^{\xi}\right) + C \qquad 5.2$$

Here, $\xi$ is the exponent ideality factor, $k_B$ is the Boltzmann's constant, $I_0$ is the intensity of illumination ($mW/cm^2$) light, and C is the constant.

Even complex, ideally, the slope of the semi-logarithmic plot of $V_{OC}$ and the illumination intensity should give a slope of $\frac{k_B T}{q}$ for the absence of trap-assisted (SRH

type) recombination. The deviation of the slope from $\frac{k_B T}{q}$ signifies the influence of traps. We present semi-logarithmic plots of $V_{OC}$ (V) vs. intensity (in the range 0.02 – 56.6 mW/cm$^2$) at various temperature (T: 50 – 400K, $\Delta T$ = 50K) and shown in fig. 5.8 a. Note that, the lower intensities (below 0.02 mW/cm$^2$) was excluded for which $V_{OC}$ deviates downward due to the shunting effect as discussed before. The slopes extracted for different temperature (50K – 400K) from the fitting is shown in fig. 5.8 b. A slight variation of the slope from $\frac{k_B T}{q}$ in all phases suggest that we have a mixture of bimolecular and trap-assisted recombination.[122] Also, in the orthorhombic and cubic phase (slope > $\frac{k_B T}{q}$ ) suggest the high possibility to have higher trap-assisted recombination.

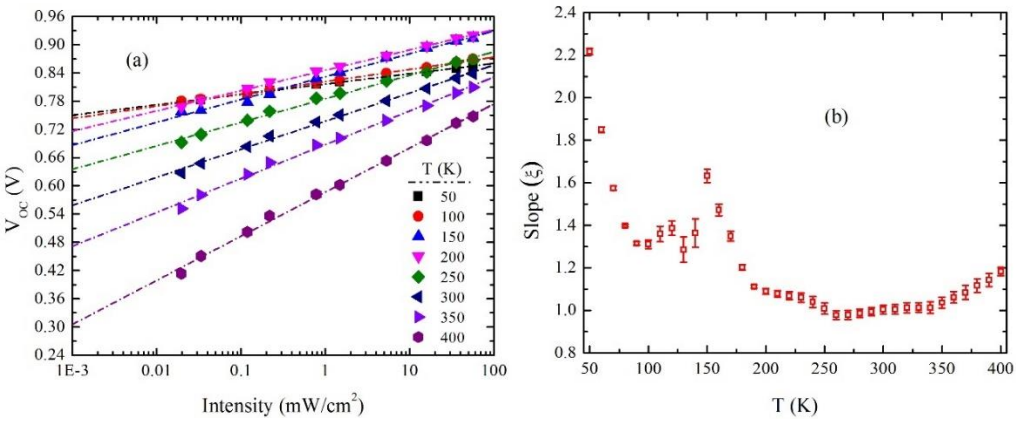


Fig. 5.8 (a) The variation of $V_{OC}$ with the logarithmic illumination intensity (mW/cm$^2$) and the fitting, (b) temperature dependent slopes to understand the recombination mechanism.

The temperature dependent $V_{OC}$ analysis at a fixed illumination level suggests recombination of the majority of generated charge at the PEDOT:PSS/Perovskite

interface. Also, the intensity-dependent $J_{SC}$ and $V_{OC}$ analysis suggest that the presence of both bimolecular and trap-assisted recombination. In solution processed perovskite solar cell, it is highly possible to incorporate chemical impurities which act as defects and locates at the interface. Also, perovskite itself has some structural disorder and have grain boundaries, as seen in the SEM images of MAPI in fig 3.4. All together leads to having trap-assisted recombination. The presence of bimolecular recombination along with the trap-assisted recombination is interesting, and the results are truly complex - compel further examination. For example, do we have exciton in our system? Well, may be no - based on the preliminary dielectric properties but not ignorable. The optical study, like combined absorption and emission spectroscopy, will be interesting path to pursue which is beyond the scope in this project.

## 5.5 MAPI phase transition study

Form the electrical performance, and recombination study the impact of phase transition on devices is evident. Room temperature XRD of MAPI thin film aiming crystallographic study and preferred orientation was presented in section 3.3.4 of chapter 3. At this point, it is essential to investigate the phase transition of the MAPI thin film used in this research. To confirm the phase transition of active MAPI film, XRD was performed at temperature 30$^{o}$C (303K) to 100$^{o}$C (373K) at 5$^{o}$C intervals. Fig. 5.9a shows the 3D waterfall plot MAPI XRD data as a function of temperature ranged between 30$^{o}$C to 100$^{o}$C at 5$^{o}$C interval. All the expected peaks of MAPI were observed. However, with the increase of temperature from 30$^{o}$C, the intensity of the peak observed 23.45$^{o}$ for 121 planes in tetragonal phase decreases. This peak completely disappeared for the temperature $\geq$ 55$^{o}$C (shown in fig. 5.9 b). The other peaks are shifted to the different

position as seen in the fig. 5.9 c. The position of peaks after 55 $^{o}$C agreed with the cubic phase peaks [65].

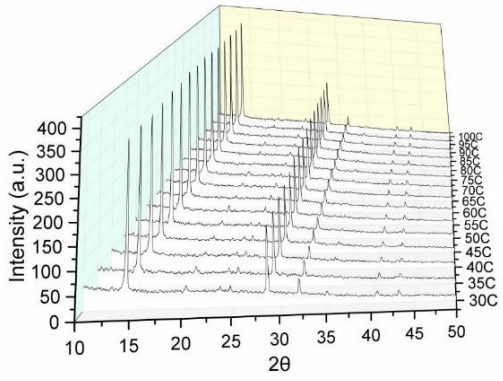


(a)

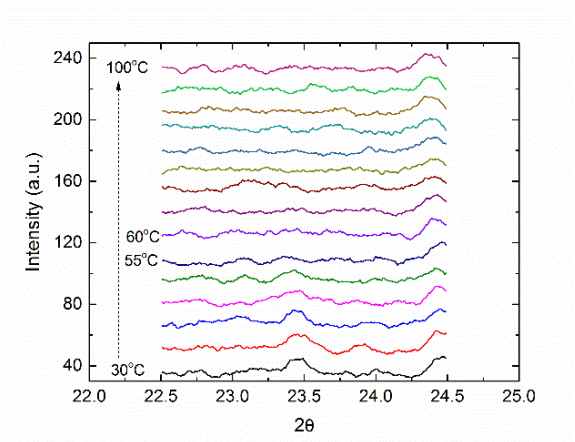


(b)

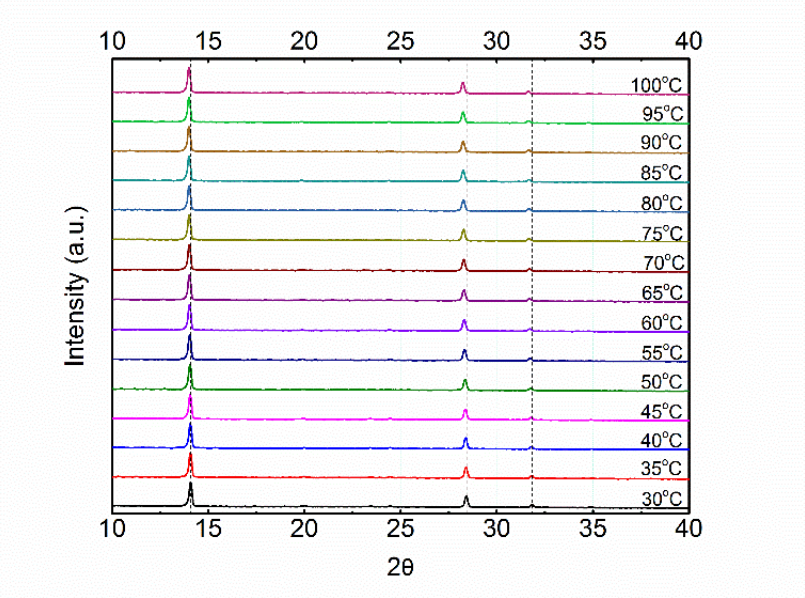


(c)

Fig. 5.9 (a) 3D waterfall plot MAPI XRD data as a function of temperature ranged between 30$^{o}$C to 100$^{o}$C at 5$^{o}$C interval. (b) The peak for 121 planes in tetragonal phase around 23.45$^{o}$ disappeared at temperature 55$^{o}$C. (c) The gradual shift of peaks' position.

The XRD facility of Texas State University does not support the low-temperature XRD measurement. That is why the orthorhombic transition could not be studied. After doing the temperature dependent XRD, the sample is cooled down to room temperature. XRD of the same sample was performed again at room temperature. MAPI converted to tetragonal phase again, which mean the phase transition is reversible. The reversibility of the MAPI phase supportive of restored device performance after keeping the device in different temperature regime.

From fig. 5.9 b and c, it is observed that the shifts of the peaks are gradual with temperature which can be associated with the thermal expansion of the lattice. The thermal expansion coefficient can be extracted from this data.

## 5.6 Temperature-dependent dielectric constant (κ)

To estimate the temperature dependent dielectric constant (κ), the frequency-dependent capacitance measurement as a function of temperature in a capacitor structure (ITO/Perovskite/Al) was performed. The value of dielectric constant (κ) found to be temperature as well as frequency dependent, as shown in fig. 5.10. The variation of dielectric (κ) constant in the temperature window of 20 – 430K is associated with the phase transition behavior (Orthorhombic – 162K – Tetragonal – 330K - Cubic) as mentioned in the figure itself. At, 10 kHz and room temperature we obtain the dielectric constant of 9.45±0.5. Note, the variation of the dielectric constant with temperature at a particular frequency - related to the $V_{OC}$ changes with T at a fixed illumination level.

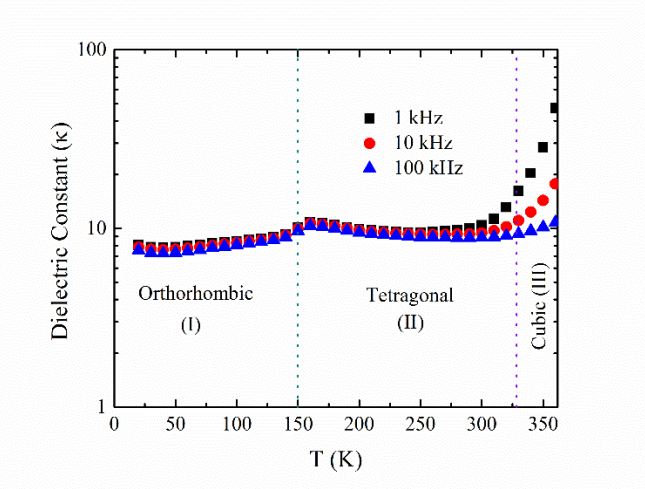


Fig. 5.10 Variation of the dielectric constant of the perovskite film with temperature (T) measured at various frequencies $f$ = 1, 10, 100 kHz.

## 5.7 Conclusion

A wide range of temperature and illumination-dependent complete device analysis was performed with the ITO/PEDOT:PSS/MAPI/$C_{60}$/BCP/Al architecture solar cell. The analysis is helpful to understand the phase transition behavior and its impact on the device parameters, particularly the $J_{SC}$ and $V_{OC}$. The temperature dependent $V_{OC}$ analysis suggest that the majority of generated charge carriers recombine at the PEDOT:PSS/Perovskite interface and in the depletion regime. The combined illumination intensity dependent analysis of $J_{SC}$ and $V_{OC}$ predicts in the device we have a mixture of the bimolecular and trap-assisted interface. The room temperature dielectric constant of 9.45±0.5 was estimated and its temperature dependency was explored– correlated with the temperature dependent either $J_{SC}$ or $V_{OC}$, and the phase transition in MAPI based perovskite. In conclusions, the information extracted in this report are valuable in developing further device technology based on halide perovskite and understand material degradation and phase transitions in MAPI.

# 6. ELECTROCHEMICAL CHARACTERIZATION OF PEROVSKITE

Note: Most of the contents from this chapter was published as a technical note in *Analytical Chemistry* Section of *ACS Publication* on 18 August 2017 by the author of this thesis along with other co-authors of the same research group. DOI number of the publication is 10.1021/acs.analchem.7b02800. The contents taken from the published article were cited where applicable.

## 6.1 Overview

In addition to outstanding optoelectronic properties, extreme interest in perovskites are attributed to ease of processing and low materials cost.[9] The simplicity of solution-based processing of perovskite materials have resulted in quick adoption in solar cells, thin film transistors (TFT),[17] light emitting diodes (LED),[123] light emitting field effect transistors,[124] lasers,[125] and more. While the properties of intrinsic perovskite materials are impressive, the delicate nature of these materials limits their ability to be precisely patterned or modified to tailor their structure and optoelectronic properties for specific applications. Furthermore, solution-based measurements of these films by electrochemistry can reveal fundamental aspects of these materials in solid state films, such as emergent energy levels and charge transfer rates. However, to date, such solution-based processing and measurements of solid-state perovskite materials have been limited [126],[127] as these materials are susceptible to dissolution in polar solvents, and nonpolar organic solvents do not support ionic transport for electrochemistry and ionic modification of films. Alternatively, an ideal fluid for processing and interrogation should not dissolve the perovskite. Furthermore, as an electrolyte, it should possess a high dielectric constant to dissolve enough ionic salt and

support electrochemical measurements. In this manner, it should function as an "orthogonal solvent," exhibiting solution behavior distinct from conventional polar and nonpolar solvents. Unfortunately, most solvents that have high dielectric constants dissolve either the perovskite material or its components. In addition to these properties, hydrogen-bond acidity, basicity, and dispersion forces should be considered, among other parameters.[128]

Fortunately, it has been demonstrated that chemically orthogonal processing of non-fluorinated organic films, both polar and non-polar, can be accomplished using highly fluorinated solvents such as hydrofluoroethers (HFEs).[129] Previous HFE treatments of various organic films did not cause any dissolution, cracking, delamination, or other unfavorable short term or long term physical or chemical damage. This was true even under extreme conditions, such as prolonged solvent exposure or elevated temperature processing.[130]–[132] Moreover, one can use HFE solvents in concert with a small addition of co-solvents to make functional electrolytes, as demonstrated with lithium based salts having fluorinated organic anions.[133],[134] HFE based electrolytes are promising for improving lithium ion battery safety and performance due to their nonflammability, high voltage stability window, less gas decomposition, modest viscosity, low freezing temperature, high vapor pressure, and low surface tension. In addition, HFEs are green fluorinated solvents with low toxicity that do not disturb the ozone. As such, these solvents are thus candidates for replacement of chlorofluorocarbons (CFCs) hydrochlorofluorocarbons (HCFCs) and perfluorocarbons (PFCs).[135]

In this chapter, the selection and optimization of a solvent based on an HFE for electrochemical characterization of a perovskite films, particularly methylammonium lead iodide perovskite (MAPI) is presented. A series of solvents were investigated to balance low solubility with high dielectric behavior, revealing the superiority of an HFE approach. A co-solvent system is then developed to create an electrolyte that optimized lithium salt solubility and conductivity. This system was then used to electrochemically characterize a MAPI film. Finally, the impact of this solution electrolyte exposure on MAPI photovoltaic device performance were studied to see if this approach maintains high photovoltaic performance.

## 6.2 Experimental section

Glass substrates with pre-patterned Indium Tin Oxide (ITO) electrodes were purchased from Lianyungang liaison quartz co., ltd. Substrates were cleaned by 20 minutes ultrasonic bath in 5 wt% of Deconex OP121 detergent in DI water solution. After ultrasonic bath, ITO-glasses were rinsed with DI water, dried at 200 $^{o}$C for 10 minutes on a hot plate and treated with oxygen plasma (Harrick Plasma, Pdc-32G) for 5 minutes. Perovskite film fabrication followed protocol published elsewhere.[41] In short $CH_3NH_3I$ (Lumtec) and lead acetate ($Pb(Ac)_2$ – Sigma Aldrich) were dissolved in anhydrous N,N-Dimethylformamide at a 3:1 molar ratio with final concentrations of 40 wt%. Perovskite films of c.a. 450 nm were prepared by spin-coating the perovskite solution at 2000 rpm in a nitrogen-filled glovebox. After spin-coating, the films were annealed at 100 °C for 5 min. Electrochemical measurements were performed using a CH Instruments CHI7014E potentiostat under Ar atmosphere. A three-electrode configuration with lithium metal as reference and counter electrode was used. HFE

solvent was donated by Orthogonal Inc. All other solvents and bis (trifluoromethane) sulfonimide lithium (LiTFSI) salt were purchased from Sigma Aldrich.

For solar cell device fabrication, a conducting polymer hole transport layer (PEDOT:PSS Hereaus 4083) was spin coated onto pre-cleaned ITO/glass substrates at 6000 rpm and then annealed at 150 °C for 10 minutes, resulting in formation of a ~30 nm thick film. Subsequently, perovskite films were deposited following the protocol described above. Devices were then transferred to a Trovato 300C vacuum thermal evaporator where 30nm of buckminsterfullerene ($C_{60}$ - Sigma Aldrich) (deposition rate 0.1 nm per second), 5 nm of bathocuproine (Sigma Aldrich) (deposition rate: 0.05 nm per second) and 100 nm of Ag metal (Kurt J. Lesker) (deposition rate: 0.2 nm per second) were deposited at a base pressure of $5 \cdot 10^{-7}$ Torr. Samples were encapsulated with recessed glass caps using UV curable epoxy resin (Ossila E131) in the glovebox and removed to air where characterization took place. Solar cell devices were tested with using an Oriel ABA solar simulator and a Keithley 2400 source measure unit.

## 6.3 Results and discussion

### 6.3.1 Solvent selection

Organic-inorganic trihalide perovskite films are typically deposited from solution that consists of an organic salt, such as methylammonium halide (MAX, here X=Cl, Br, I), and an inorganic salt, such as lead halide ($PbX_2$). In some case other chemical additives are used to enhance quality. Between these two integral constituent salts, MAX is generally the most soluble component of the perovskite; hence, it is necessary to ensure that the electrolyte to be used does not dissolve MAX. To determine an appropriate solvent, the solubility of MAI (a popularly used and highly soluble representative of

methylammonium halide) in different classes of solvents were experimentally determined. Table 6.1 summarizes the room temperature solubility of methylammonium iodide (MAI) in representative solvents of three classes: polar, nonpolar and fluorous.

Table 6.1 List of maximum solubility of MAI in different polar, non-polar and fluorous solvents along with dielectric constant.

| Solvent Category | Solvent | MAI Solubility (M) | Dielectric Constant | Reference |
|---|---|---|---|---|
| Polar | IPA | 0.45 | 18.3 | [136] |
| Polar | DMF | 6.3 | 36.7 | [136] |
| Polar | Water | 12 | 79.7 | [136] |
| Polar | Acetonitrile** | 0.75 | 37.5 | [136] |
| Fluorous | HFE 7100 | $<10^{-3}$ | 7.39 | * |
| Fluorous | HFE 7300 | $<10^{-3}$ | 6.1 | * |
| Nonpolar | Diethyl Carbonate | $<10^{-3}$ | 2.8 | [137] |
| Nonpolar | Toluene | $1.17\times10^{-3}$ | 2.38 | [136] |

*Provided by manufacturer - 3M company.

**Measured in anhydrous acetonitrile in a nitrogen atmosphere.

Due to the ionic nature of perovskite materials, polar non-fluorinated solvents such as N,N-dimethylformamide (DMF) are suitable for preparing perovskite precursor solutions. Other polar solvents extensively used for solution based growth and deposition of perovskite include N-methyl-2-pyrrolidone (NMP), γ-butyrolactone (GBL) and dimethyl sulfoxide (DMSO).[138],[78],[57] Isopropanol (IPA) is moderately effective at dissolving MAI and does not dissolve $PbI_2$, a property that has been used to make

perovskite films in a two-step process.[139] Water (protic) and acetonitrile (aprotic), two common electrolytes, both effectively dissolved MAI with similar efficacy to IPA, and hence were unsuitable for this application. Non-polar organic solvents, such as toluene and diethyl carbonate, do not dissolve MAI, and are commonly used to  and control film morphology and crystallinity.[57],[140] However, as seen in Table 6.1, these have a low dielectric constant, making them unsatisfactory as an electrolyte. Alternatively, HFEs combine reasonably high polarizability with low MAI solubility. In particular, MAI showed a low solubility (<1 mM) in HFE 7100 and HFE 7300, and these solvents have reasonably high dielectric constants between 6 and 8. These features, together with their other properties (non-flammability, low toxicity, etc.), make them promising candidates for electrolytes for perovskite films.

### 6.3.2 Electrolyte preparation

In order to, use HFE based solvents as electrolytes, the intended salt should be soluble in the solvent, the perovskite should remain insoluble, and the combined system must show high ionic conductivity and electrochemical stability. We used HFE 7100 (which is a mixture of two inseparable isomers: methyl nonafluoroisobutyl ether and methyl methyl nonafluorobutyl ether) solvent and bis (trifluoromethane) sulfonimide lithium (LiTFSI) salt. HFE 7100 does not dissolve LiTFSI at room temperature. Thus, diethyl carbonate (DEC), which also does not dissolve perovskites, was added as a co-solvent to promote LiTFSI solubility.

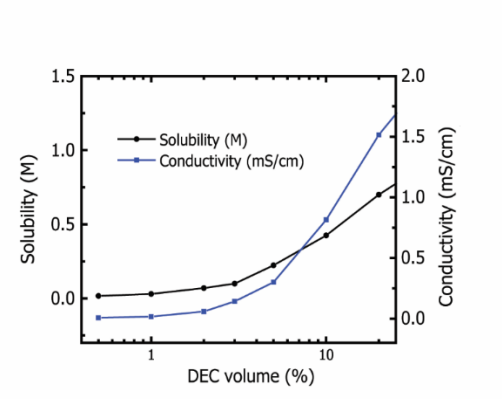


Fig. 6.1 Maximum attainable solubility of bis (trifluoromethane) sulfonimide lithium (LiTFSI) salt in HFE 7100 and diethyl carbonate (DEC) solvent mixture at room temperature with corresponding electrical conductivity.

Thus, we aimed to find a mixture of HFE with DEC that minimized DEC concentration while maintaining appreciable conductivity. We measured the solubility limit of LiTFSI salt and the corresponding electrical conductivity in various mixtures of HFE 7100 and DEC, with the results plotted in Fig. 6.1. As can be seen, the solubility gradually increased with increasing DEC volume fraction. Correspondingly, due to the different solubility of LiTFSI, the conductivity of electrolyte also increases with increasing DEC content. Therefore, the conductivity can be changed appreciably, by more than an order of magnitude, by changing the relative solvent composition of HFE 7100 and DEC. In this instance, as a low DEC concentration is desired for maximum perovskite retention, a 97% HFE fraction was selected for further electrochemical study. At this concentration, 0.1 M LiTFSI can be achieved with a conductivity of 0.14 mS/cm.

Since DEC does not dissolve perovskite and dissolve LiTFSI very well, the LiTFSI in DEC electrolyte can be an option as orthogonal electrolyte. To test the feasibility MAPI thin films was submerged in 0.1 M LiTFSI in DEC electrolyte for

different time. Over the time perovskite film gradually degraded evident from the color change (see fig. 6.2). Hence, pure DEC with LiTFSI does slowly degrade these perovskite films.

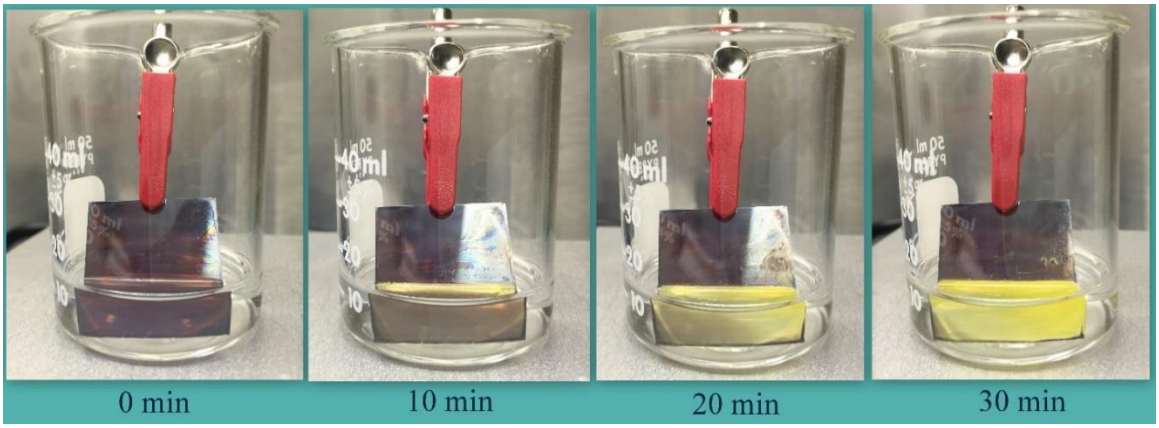


Fig. 6.2 The images of perovskite film on glass substrate submerged in 0.1M bis (trifluoromethane) sulfonimide lithium salt (LiTFSI) in diethyl carbonate (DEC) solvent at different time period.

### 6.3.3 Electrochemical toolkit development

After selecting the electrolyte, the goal of this work was to use this electrolyte for MAPI characterization by cyclic voltammetry (CV). Due to evaporative nature of HFE based electrolyte and delicacy of MAPI film, it was challenging to use the conventional setup for CV. Figure 6.3 shows the schema of the CV toolkit development. In fig. 6.3 (A), Left figure shows the cross-sectional schematic diagram of the prepared perovskite sample on ITO/glass substrate for cyclic voltammetry measurement. The perovskite film is covered with kapton tape except the area to be exposed in electrolyte for cyclic voltammetry. Right figure shows the top view of the same sample. Silver paste is used at the contact points of the electrode. Fig. 6.3 (B) shows, (Left) Cross sectional schematic diagram of the counter and reference electrode, (Right) Top view of counter and

reference electrode. Li sheet is attached on the glass substrate with the help of double sided kapton tape. In fig. 6.3 (C) images of the real kit used for CV measurement is shown. A rubber sealed customized electrolyte container (left) that can be enclosed by lid from which sample and electrode can be mounted. Right image shows the top view of the lid from the other side.

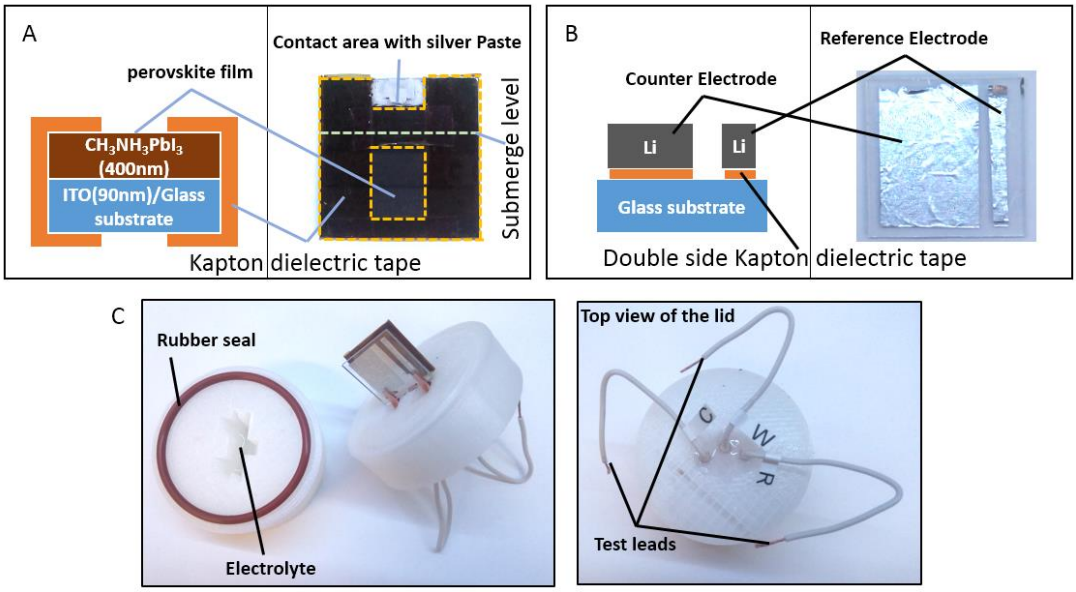


Fig. 6.3 (A) MAPI sample preparation for CV, (B) Reference and counter electrode preparation. (C) Images of the real kit used for CV measurement.

### 6.3.4 Cyclic voltammetry of MAPI

To validate the selected electrolyte solvent mixture for electrochemical oxidation and reduction of organic lead halide perovskites, cyclic voltammetry (CV) was performed on MAPI films coated on ITO using the toolkit mentioned above. CVs were recorded in three-electrode configuration using CHI7014E potentiostat. To test perovskite electrochemistry, a 400 nm thick MAPI film on ITO was used as the working electrode, and lithium metal was used as reference and counter electrode, a common reference with

lithium salts. The scan rate for CV was 10 mV/s. Figure 6.4a shows the cyclic voltammogram of ITO and ITO/MAPI. For the perovskite film on ITO, a peak anode current (IPA) of $2.8\times10^{-7}$ A and peak cathode current ($I_{PC}$) of $1.5\times10^{-7}$ A were observed at 4.96 V and 4.65 V respectively. The $I_{PA}$ and $I_{PC}$ were found to be comparable, which indicated that the oxidation reaction is quasi-reversible. Multiple cycle data (Fig. 6.4b) confirms the stability of the system with fixed redox peak positions. Small current drop after a few consecutive scans can be caused by the evaporation of volatile HFE solvent through the micropores of the plastic electrochemical cell (Fig. 6.3C).

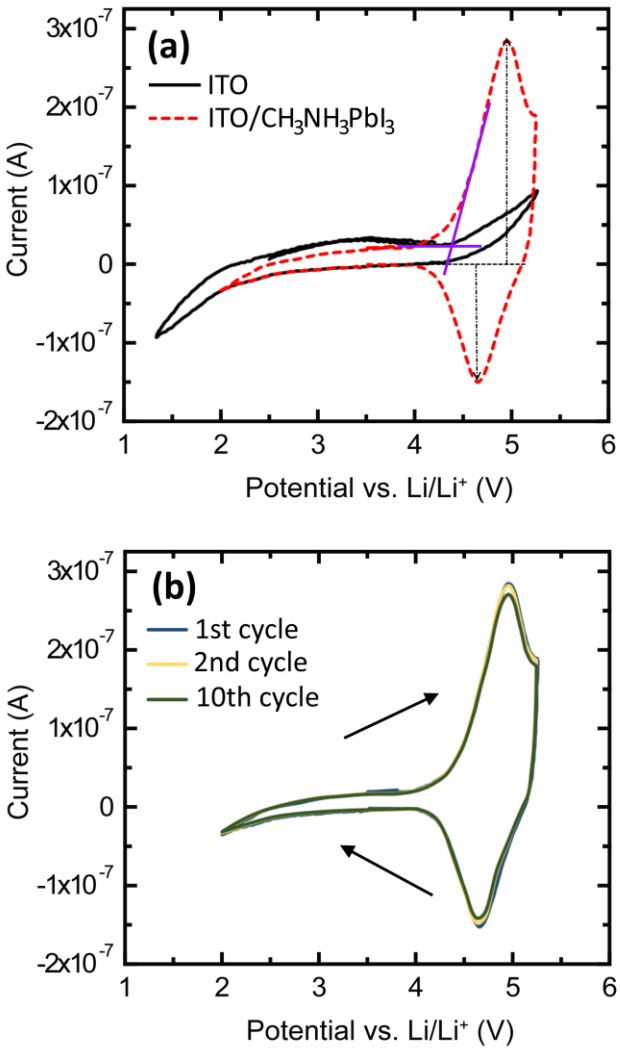


Fig. 6.4 (a) Cyclic voltammetry of ITO/MAPI and bare ITO in HFE electrolyte. ITO shows no peak for oxidation and reduction. For ITO/MAPI oxidation peaks are observed. (b) Multiple CV scans of ITO/MAPI in HFE electrolyte indicate stability of the system. Small current loss is associated with evaporation of volatile electrolyte solvent. [141]

The CV of a bare ITO film on glass was measured to test electrolyte stability, and no redox reaction was observed from this system. This indicated that the observed oxidation peaks were contributed only by the perovskite film and that the electrolyte is

stable for the voltage window from 1V to 5.5V. The HOMO level of MAPI can be estimated from the oxidation onset voltage of the CV using equation 6.1:

$$E_{HOMO} = -e\,(E_{ox}^{onset} + E_{Li/Li+}) \qquad (6.1)$$

Using, this, the HOMO level is found to be -5.64 eV, which conforms to the range of reported valence band energy level values measured using ultraviolet and x-ray photoelectron spectroscopic techniques.[142],[143],[144]

### 6.3.5 Photovoltaic performance test after electrolyte treatment of MAPI

Although a low solubility of the delicate perovskite component MAI in HFE and DEC was shown from solubility and CV measurements, it is critical to ensure negligible delamination of full perovskite films and minimal surface adsorption of the electrolyte when perovskite films are exposed to the electrolyte. To further confirm the inertness of the HFE based electrolyte on perovskite films directly, we compared the photovoltaic performance of perovskite solar cells fabricated with and without electrolyte treatment. Samples were immersed into electrolyte in the glass beakers. Some of the samples were washed using a mixture of HFE and DEC solvent. For washing samples were spin rinsed at 1000 RPM for 1 min using approximately 2 mL of cleaning solvents. All treatments were done inside N2 glove box. A batch of identical perovskite solar cells were prepared and grouped into four categories for different electrolyte treatments as described in table 6.2. The films were treated with 0.1 M LiTFSI in 97% HFE 7100/3% DCE (v/v), the same electrolyte mixture as used for CV measurements. Sample (A) was not treated with electrolyte and was used as a reference.

Table 6.2 Solar cell performance of four groups of samples after different electrolyte treatment and HFE wash.

| Sample type | Treatment | Efficiency (%) | FF | $J_{SC}$ ($mA/cm^2$) | $V_{OC}$ (V) |
|---|---|---|---|---|---|
| A | Reference | 13.52 | 66.4 | 21.80 | 0.93 |
| B | Dipped in electrolyte + 5 min | 0.000054 | 24 | 0.0015 | 0.13 |
| C | Dipped in electrolyte for 5 min + Spin rinsed[a] | 12.60 | 59.40 | 23.00 | 0.92 |
| D | Dipped in electrolyte for 5 min + Spin rinsed[b] | 13.54 | 63.60 | 22.20 | 0.96 |

[a]Rinsed with 90% HFE 7100+ 10% DEC spin rinsing

[b]Rinsed with 90% HFE 7300+ 10% DEC spin rinsing

After the different electrolyte treatment, the active layers were dried in N2 and deposited with electron transport layers and silver electrode, followed by encapsulation before photovoltaic characterization. The device structure of the fabricated cells were ITO/PEDOT:PSS/MAPI/$C_{60}$/BCP/Ag which is similar as described in section 4.2.

Figure 6.5 shows the illuminated and dark current density-voltage (J-V) characteristics of devices A, C and D. Device B showed no photovoltaic behavior and hence is not shown in the figure.

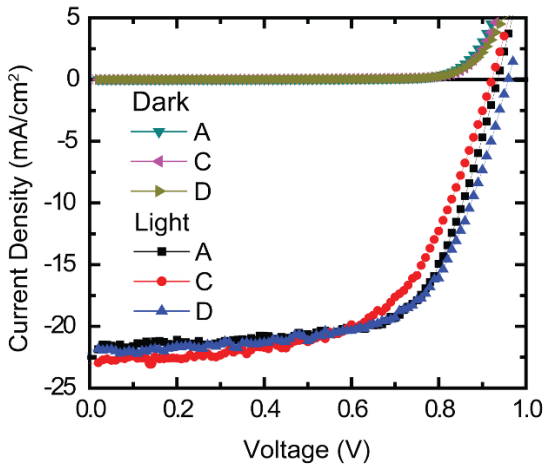


Fig. 6.5 J-V characteristics of solar cells with different electrolyte treatment as described in Table II. The dark current density graphs are indistinguishable for all the types of sample. Negligible deviation in J-V graphs are evident between reference sample A and electrolyte treated sample C, D.

The photovoltaic parameters are tabulated in Table 6.2. Device C and D show comparable performance as Device A and the minor differences observed were within the experimental deviation. The poor performance of device B is attributed to significant amount of residual salt after drying the film which can be clearly observed in the SEM images in fig. 6.6.

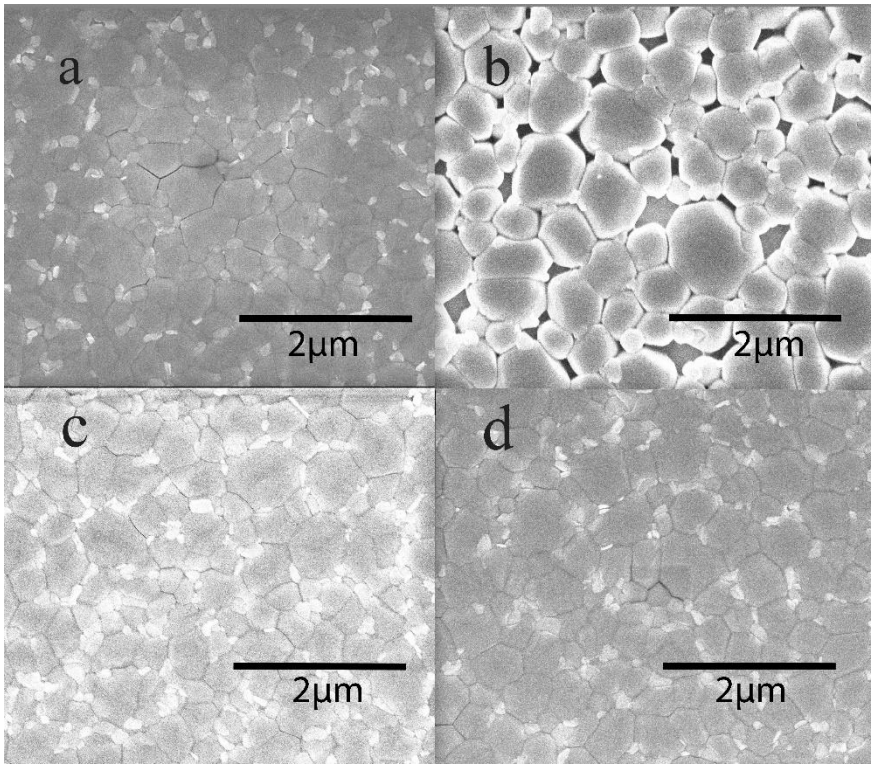


Fig. 6.6 SEM images of the samples A-D. Sample A is the reference sample, which was not treated with electrolyte. Sample B dipped in electrolyte for five minutes but not washed after that. The residue salt is visible on the surface of the sample B. Sample C and D also dipped in electrolyte for 5min, then followed by spin rinsing using 90% HFE 7100+ 10% DEC and 90% HFE 7300+ 10% DEC respectively.

This residual salt forms an insulating layer between the electron transport layer and the perovskite, leading to complete loss of photovoltaic performance. On the other hand, SEM images show negligible changes for Sample C and D, indicating that rinsing with 90% HFE+ 10% DEC removes of all the residual salt from the surface.

## 6.4 Conclusion

In summary, the low solubility of MAI in HFEs and DEC solvents were observed from direct study. To enhance the conductivity of the HFE based electrolyte, a small

amount of (~ 3 vol. %) DEC with LiTFSI salt was added. Further applicability of the solvent mixture for carrying out electrochemistry to study redox reactions of perovskite films was demonstrated with cyclic voltammetry. Finally, we showed that perovskite films subjected to this optimized electrolyte treatment had a negligible effect on the photovoltaic performance when films were used as active layers in solar cells. Hence HFE based electrolyte show promising potential for future electrochemical processing such as redox, characterization, transport and doping. [141]

# 7. CONCLUSION AND FUTURE SCOPE

## 7.1 Introduction

To recapitulate, the whole research work reported in this dissertation consists of three projects. In the first project, solution-based perovskite synthesis was optimized by manipulating the precursor solution. The second project was done on temperature and illumination-dependent study of MAPI solar cell. The third project was the development of electrochemical characterization and processing capabilities for perovskite. In the section to follow, conclusion on the outcome of the individual projects has been drawn. Besides, the outline of the prospective future research is presented.

## 7.2 Solution-based perovskite synthesis optimization

### 7.2.1 Conclusion

The central focus of the MAAc assisted MAPI deposition method is to achieve scalability of solar cell fabrication. Up to final stage of the current research device fabrication was not scaled up. However, a scalable, reproducible noble approach of an one-step solution-based perovskite deposition method was developed.

The introduction of MAAc of optimum proportion in the precursor solution evidently facilitated to obtain a uniform, large grain defect free MAPI and $MAPbBr_3$ thin film. The characterization of films and devices derived from the films suggest that the use of MAAc is more effective for one step synthesis method compared with other techniques. Ink formulation optimization benefited without introducing new process steps. The results presented here are based on spin-coated deposition. Commercial solution-based thin film deposition usually done by slot-die or roll to roll method. After developing this process, Texas State Univerisity, Organic Semiconductor Device lab

secured a *National Science Foundation's* SBIR grant phase I (#1721884) for "Scalable fabrication of stable perovskite solar panels using slot-die coating technique." nTACT is a slot-die solution provider company, partnering with Texas State in this project. To propose the future scope of this deposition technique, little exposure of the preliminary results of the slot die project worth discussing. As a part of this project work, one of the co-researchers of the Organic semiconductor lab, Chris Manspeaker conducted slot die coating of the MAAc based perovskite on both large glass substrate and flexible substrates. Thin films were deposited using different dispense rate then characterized using UV-Vis and XRD. Fig. 7.1a shows the perovskite films coated using the slot die method in nTACT company. Fig. 7.1b shows the XRD data for the 1:1:1 ink at the different dispense rates. These figures are adopted from the PhD thesis of Chris Manspeaker.[145] The peaks observed in the XRD pattern agrees with the tetragonal MAPI phase with additional peak for unconverted $PbI_2$.

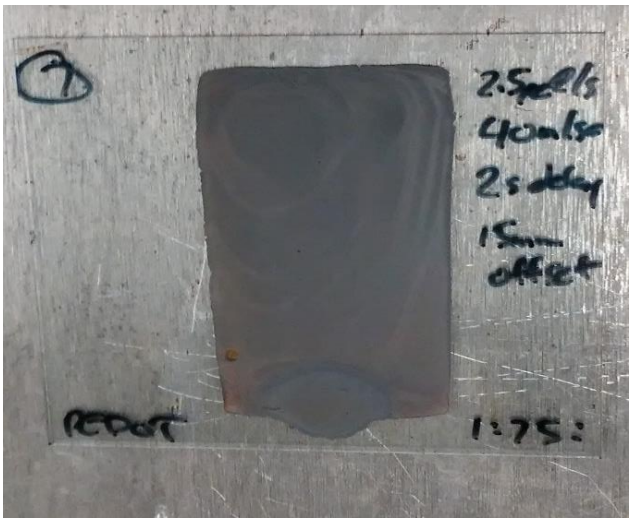

(a)

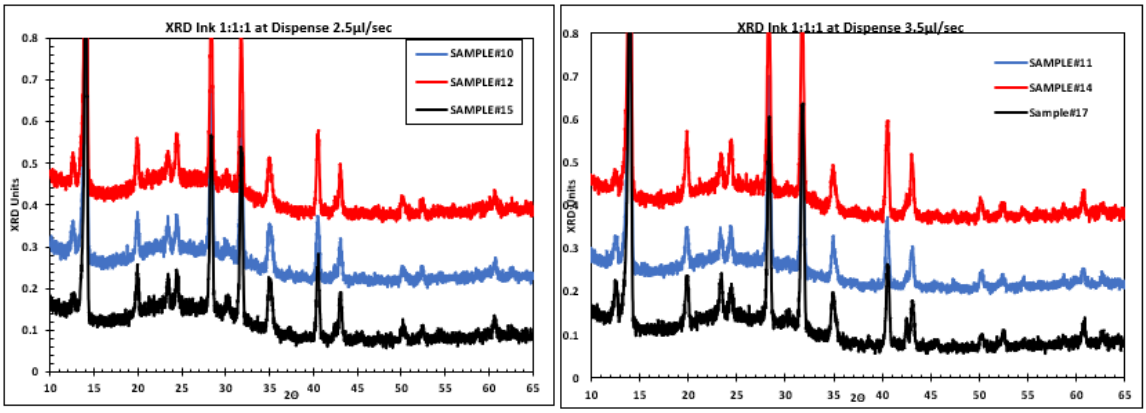


(b)

Fig. 7.1 (a) Photograph of slot-die coated MAPI film. (b) XRD data for the 1:1:1 ink at the different dispense rates. Thicker samples are in red, thinnest is black. (figures adopted from reference [145])

### 7.2.2 Future scope

The MAAc assisted perovskite deposition method is a highly promising technique for commercialization. In this research, a comprehensive study of the MAAc assisted

method for MAPI is done. Compatibility of the technique for $MAPbBr_3$ is also partially explored. However, a lot of future prospective research can be done based on the current outcome of this research as listed below.

1. Compatibility of the technique for the other perovskite such as mixed halide, mixed cation perovskite deposition can be investigated.
2. Slot-die has been utilized for large area MAPI deposition. It seems a very promising method for large scale deposition. One important thing to note that, the deposition parameters and environment are different for slot-die compared with spin coating. Thus, ink formulation, dispense rate and annealing need to be optimized for best results.
3. Upon slot-die process optimization, solar cell fabrication is the next critical work to be done. Current lab facility of the Texas State is customized for 1 square inch substrates. Transformation to a bigger substrate needs significant modification of the infrastructures. Upon availability, large area solar cell panel can be fabricated using the slot-die coated perovskite thin film.

## 7.3 Temperature and light intensity dependent study

### 7.3.1 Conclusion

In this project, the temperature and light intensity dependent solar cell performance was investigated. Also, the origin and type of carrier recombination were studied. It was found that most of the recombination occurs in the hole transport layer-MAPI interface. This observation suggests that the improvement of the HTL/MAPI interface can improve the efficiency of the cell. Moreover, the dielectric constant of the MAPI thin film was determined for three different crystallographic phases.

### 7.3.2 Future scope

The future scope of this projects is enlisted below:

1. Recently two copper-based inorganic HTLs are investigated and optimized for the solar cell structure used in this research. A comparative carrier recombination study can be conducted to find the best HTL.
2. For intensity dependent study, maximum intensity of 56.6 mW/cm$^2$ was available in the current system. This study can be further extended to one sun (100 mW/cm$^2$), which is considered as standard.

## 7.4 Development of electrochemistry for perovskite processing

### 7.4.1 Conclusion

A suitable electrolyte and electrochemical toolkit were developed for MAPI perovskite processing. The system was utilized for cyclic voltammetry, oxidation potential, and HOMO level study of MAPI this film. Photovoltaic properties of MAPI thin film were retained even after electrolyte. The photovoltaic property was tested by fabricating solar cells after electrolyte treatment. This is a pioneering development towards electrochemical characterization and processing of perovskite. Until this development, no stable electrolyte was reported that allow perovskite to study without damage or degradation.

### 7.4.2 Future scope

Being a new field, the scope of perovskite electrochemistry for further research is wide open. The electrochemical method can be utilized for interrogating as well as modifying the properties of perovskite. All successful attempt of high-efficiency solar cell reported are based on p-i-n or n-i-p architecture. One of the reasons behind adopting

those architectures instead of conventional p-n architecture is the inability to dope perovskites. Electrochemical doping is an established technique for doping. Following two are suggestion from a list of potential research among so many options:

1. The implemented perovskite optoelectronic device architecture uses intrinsic perovskites. Conventional doping techniques by diffusion during the deposition of the thin film is inapt for solution processed perovskite thin films. However, electrochemical doping is an appropriate method for perovskite doping. [146] Successive anionic and cationic doping of solid-state perovskite films can be achieved in HFE-based electrochemically-driven ion implantation. This p and n-type doping can bring new electronic states for improved photon absorption, conductivity, and power conversion efficiency.
2. As a representative of hybrid perovskite, only MAPI was studied using cyclic voltammetry. The other representative of perovskites such as mixed halide, mixed cation, and combination thereof can be investigated by the electrochemical method. To be noted that, the HOMO level of MAPI was estimated accurately using CV data. Still, the LUMO level was not studied due to the limitation of the system. By improving the electrochemical stability window, a further measurement can be done on MAPI.

## REFERENCES


[1] A. A. Benson, C. F. Allen, P. Good, H. F. Davis, P. Chisum, J. B. Mudd, R. B. Holtz, A. A. Benson, E. Racker, W. J. Dyer, P. Mazliak, M. Kates, T. S. Moore, T. Kagawa, H. Beevers, E. P. Kennedy, K. W. A. Wirtz, D. B. Zilversmit, R. M. Dawson, M. G. Sarzala, J. Zborowski, L. Wojtczak, and G. Hubscher, "Amorphous Semiconductor Switching in Melanins," *Science (80-. ).*, vol. 183, no. 6, pp. 853–855, 1973.

[2] C. W. Tang, "Two-layer organic photovoltaic cell," *Appl. Phys. Lett.*, vol. 48, no. 2, pp. 183–185, 1986.

[3] NREL, "Best Research-Cell Efficiencies," *Best Research-Cell Efficiencies*, 2019. [Online]. Available: https://www.nrel.gov/pv/assets/pdfs/best-research-cell-efficiencies-190416.pdf.

[4] S. Yang, W. Fu, Z. Zhang, H. Chen, and C.-Z. Li, "Recent advances in perovskite solar cells: efficiency, stability and lead-free perovskite," *J. Mater. Chem. A*, vol. 00, pp. 1–21, 2017.

[5] S. A. Veldhuis, P. P. Boix, N. Yantara, M. Li, T. C. Sum, N. Mathews, and S. G. Mhaisalkar, "Perovskite Materials for Light-Emitting Diodes and Lasers," *Adv. Mater.*, pp. 6804–6834, 2016.

[6] K. Leo, "Signs of stability," *Nat. Nanotechnol.*, vol. 10, no. 7, pp. 574–575, 2015.

[7] J. Yang, B. D. Siempelkamp, E. Mosconi, F. De Angelis, and T. L. Kelly, "Origin of the Thermal Instability in CH3NH3PbI3 Thin Films Deposited on ZnO," *Chem. Mater.*, vol. 27, no. 12, pp. 4229–4236, 2015.

[8] Q. Chen, N. De Marco, Y. Yang, T. Bin Song, C. C. Chen, H. Zhao, Z. Hong, H. Zhou, and Y. Yang, "Under the spotlight: The organic-inorganic hybrid halide perovskite for optoelectronic applications," *Nano Today*, vol. 10, no. 3, pp. 355–396, 2015.

[9] M. A. Green, A. Ho-Baillie, and H. J. Snaith, “The emergence of perovskite solar cells,” *Nat Phot.*, vol. 8, no. 7, pp. 506–514, 2014.

[10] Y.-C. Hsiao, T. Wu, M. Li, Q. Liu, W. Qin, and B. Hu, “Fundamental physics behind high-efficiency organo-metal halide perovskite solar cells,” *J. Mater. Chem. A*, vol. 3, no. 30, pp. 15372–15385, 2015.

[11] Z. Shi and A. H. Jayatissa, “Perovskites-based solar cells: A review of recent progress, materials and processing methods,” *Materials (Basel).*, vol. 11, no. 5, 2018.

[12] M. M. Lee, J. Teuscher, M. Tsutomu, M. Tarkurou, and H. Snaith, “Efficient Hybrid Solar Cells Based on Meso-Superstructured Organometal Halide Perovskites,” vol. 338, no. November, pp. 643–647, 2012.

[13] J. H. Noh, S. H. Im, J. H. Heo, T. N. Mandal, and S. Il Seok, “Chemical Management for Colorful, E ffi cient, and Stable Inorganic − Organic Hybrid Nanostructured Solar Cells,” 2013.

[14] C. C. Stoumpos, C. D. Malliakas, and M. G. Kanatzidis, “SI: Semiconducting tin and lead iodide perovskites with organic cations: Phase transitions, high mobilities, and near-infrared photoluminescent properties,” *Inorg. Chem.*, vol. 52, no. 15, pp. 9019–9038, 2013.

[15] L. K. Ono, M. R. Leyden, S. Wang, and Y. Qi, “Organometal halide perovskite thin films and solar cells by vapor deposition,” *J. Mater. Chem. A*, vol. 4, no. 18, pp. 6693–6713, 2016.

[16] J. Cui, H. Yuan, J. Li, X. Xu, Y. Shen, H. Lin, and M. Wang, “Recent progress in efficient hybrid lead halide perovskite solar cells,” *Sci. Technol. Adv. Mater.*, vol. 16, no. 3, p. 036004, 2015.

[17] Y. Mei, C. Zhang, Z. V. Vardeny, and O. D. Jurchescu, “Electrostatic gating of hybrid halide perovskite field-effect transistors: balanced ambipolar transport at room-temperature,” *MRS Commun.*, vol. 5, no. 02, pp. 297–301, 2015.

[18] X. Y. Chin, D. Cortecchia, J. Yin, A. Bruno, and C. Soci, “Lead Iodide Perovskite Light-Emitting Field-Effect Transistor,” *Nat. Commun.*, vol. 6, no. May, p. Advance, 2015.

[19] D. Bi, S.-J. Moon, L. Häggman, G. Boschloo, L. Yang, E. M. J. Johansson, M. K. Nazeeruddin, M. Grätzel, and A. Hagfeldt, “Using a two-step deposition technique to prepare perovskite (CH3NH3PbI3) for thin film solar cells based on ZrO2 and TiO2 mesostructures,” *RSC Adv.*, vol. 3, no. 41, p. 18762, 2013.

[20] J. Wang, F. Liu, G. Wang, L. Wang, and C. Jiang, “Novel organic-perovskite hybrid structure forward photo field effect transistor,” *Org. Electron. physics, Mater. Appl.*, vol. 38, pp. 158–163, 2016.

[21] Y. Wu, J. Li, J. Xu, Y. Du, L. Huang, J. Ni, H. Cai, and J. Zhang, “Organic–inorganic hybrid CH $_3$ NH $_3$ PbI $_3$ perovskite materials as channels in thin-film field-effect transistors,” *RSC Adv.*, vol. 6, no. 20, pp. 16243–16249, 2016.

[22] H. Chen, “Two-Step Sequential Deposition of Organometal Halide Perovskite for Photovoltaic Application,” *Adv. Funct. Mater.*, vol. 27, no. 8, 2017.

[23] I. V Markov, *Crystal Growth for Beginners*. 2003.

[24] Q. Chen, N. De Marco, Y. Yang, T. Bin Song, C. C. Chen, H. Zhao, Z. Hong, H. Zhou, and Y. Yang, “Under the spotlight: The organic-inorganic hybrid halide perovskite for optoelectronic applications,” *Nano Today*, vol. 10, no. 3, pp. 355–396, 2015.

[25] N. G. Park and H. Segawa, “Research Direction toward Theoretical Efficiency in Perovskite Solar Cells,” *ACS Photonics*, vol. 5, no. 8, pp. 2970–2977, 2018.

[26] Jeol Ltd, “SEM Scanning Electron Microscope A To Z Basic Knowledge For Using The SEM Construction of Instrument Electron Gun Construction of Lens Condenser Lens and Objective Lens Specimen Stage Secondary Electron Detector Image Display and Recording Vacuum System,” *Jeol Ltd*, pp. 1–32, 2009.

[27] M. Mazumder, R. Ahmed, A. Wajahat Ali, and S. J. Lee, “SEM and ESEM techniques used for analysis of asphalt binder and mixture: A state of the art review,” *Constr. Build. Mater.*, vol. 186, pp. 313–329, 2018.

[28] A. A. Bunaciu, E. gabriela Udriştioiu, and H. Y. Aboul-Enein, “X-Ray Diffraction: Instrumentation and Applications,” *Crit. Rev. Anal. Chem.*, vol. 45, no. 4, pp. 289–299, 2015.

[29] Keigo Nagao, “X-ray thin film measurement techniques - Pole figure measurement,” vol. 27, no. 2, p. 2, 2014.

[30] K. Inaba, S. Kobayashi, K. Uehara, A. Okada, S. L. Reddy, and T. Endo, “High Resolution X-Ray Diffraction Analyses of (La,Sr)MnO<sub>3</sub>/ZnO/Sapphire(0001) Double Heteroepitaxial Films,” *Adv. Mater. Phys. Chem.*, vol. 03, no. 01, pp. 72–89, 2013.

[31] J. A. W. Co, *CompleteEASE ™ Data Analysis Manual*. 2011.

[32] Tektronix, “Performing Cyclic Voltammetry Measurements Using Model 2450-EC or 2460-EC Electrochemistry Lab System,” pp. 1–8.

[33] N. Elgrishi, K. J. Rountree, B. D. McCarthy, E. S. Rountree, T. T. Eisenhart, and J. L. Dempsey, “A Practical Beginner’s Guide to Cyclic Voltammetry,” *J. Chem. Educ.*, vol. 95, no. 2, pp. 197–206, 2018.

[34] S. a Myers, “An Investigation of Liquid Crystalline and Semiconducting Blends for Applications in Photovoltaics,” no. May, 2012.

[35] L. Qiu, L. K. Ono, and Y. Qi, “Advances and challenges to the commercialization of organic–inorganic halide perovskite solar cell technology,” *Mater. Today Energy*, vol. 7, pp. 169–189, 2018.

[36] Z. Xiao, C. Bi, Y. Shao, Q. Dong, Q. Wang, Y. Yuan, C. Wang, Y. Gao, and J. Huang, “Efficient, high yield perovskite photovoltaic devices grown by interdiffusion of solution-processed precursor stacking layers,” *Energy Environ. Sci.*, vol. 7, no. 8, pp. 2619–2623, 2014.

[37] Z. Xiao, Q. Dong, C. Bi, Y. Shao, Y. Yuan, and J. Huang, “Solvent Annealing of Perovskite-Induced Crystal Growth for Photovoltaic-Device Efficiency Enhancement,” *Adv. Mater.*, vol. 26, no. 37, pp. 6503–6509, 2014.

[38] W. S. Yang, J. H. Noh, N. J. Jeon, Y. C. Kim, S. Ryu, J. Seo, and S. Il Seok, “High-performance photovoltaic perovskite layers fabricated through intramolecular exchange,” *Science (80-. ).*, vol. 348, no. May, pp. 1234–1237, 2015.

[39] J. W. Lee, H. S. Kim, and N. G. Park, “Lewis Acid-Base Adduct Approach for High Efficiency Perovskite Solar Cells,” *Acc. Chem. Res.*, vol. 49, no. 2, pp. 311–319, 2016.

[40] D. Forgács, M. Sessolo, H. J. Bolink, Y. C. Kim, S. Ryu, J. Seo, S. I. Seok, S. Lu, Y. Liu, H. Zhou, Y. Yang, S. Yao, Y. Chen, R. H. Friend, L. A. Estroff, U. Wiesner, and H. J. Snaith, “Lead acetate precursor based p-i-n perovskite solar cells with enhanced reproducibility and low hysteresis,” *J. Mater. Chem. A*, vol. 3, no. 27, pp. 14121–14125, 2015.

[41] W. Zhang, M. Saliba, D. T. Moore, S. K. Pathak, M. T. Horantner, T. Stergiopoulos, S. D. Stranks, G. E. Eperon, J. A. Alexander-Webber, A. Abate, A. Sadhanala, S. Yao, Y. Chen, R. H. Friend, L. A. Estroff, U. Wiesner, and H. J. Snaith, “Ultrasmooth organic-inorganic perovskite thin-film formation and crystallization for efficient planar heterojunction solar cells,” *Nat Commun*, vol. 6, p. 6142, 2015.

[42] F. K. Aldibaja, L. Badia, E. Mas-Marzá, R. S. Sánchez, E. M. Barea, and I. Mora-Sero, “Effect of different lead precursors on perovskite solar cell performance and stability,” *J. Mater. Chem. A*, vol. 3, no. 17, pp. 9194–9200, 2015.

[43] F. Huang, Y. Dkhissi, W. Huang, M. Xiao, I. Benesperi, S. Rubanov, Y. Zhu, X. Lin, L. Jiang, Y. Zhou, A. Gray-Weale, J. Etheridge, C. R. McNeill, R. A. Caruso, U. Bach, L. Spiccia, and Y. B. Cheng, “Gas-assisted preparation of lead iodide perovskite films consisting of a monolayer of single crystalline grains for high efficiency planar solar cells,” *Nano Energy*, vol. 10, pp. 10–18, 2014.

[44] B. Conings, A. Babayigit, M. T. Klug, S. Bai, N. Gauquelin, N. Sakai, J. T.-W. Wang, J. Verbeeck, H.-G. Boyen, and H. J. Snaith, “A Universal Deposition Protocol for Planar Heterojunction Solar Cells with High Efficiency Based on Hybrid Lead Halide Perovskite Families,” *Adv. Mater.*, pp. 1–9, 2016.

[45] J. Qing, H. T. Chandran, Y. H. Cheng, X. K. Liu, H. W. Li, S. W. Tsang, M. F. Lo, and C. S. Lee, “Chlorine Incorporation for Enhanced Performance of Planar Perovskite Solar Cell Based on Lead Acetate Precursor,” *ACS Appl. Mater. Interfaces*, vol. 7, no. 41, pp. 23110–23116, 2015.

[46] L. Zhao, D. Luo, J. Wu, Q. Hu, W. Zhang, K. Chen, T. Liu, Y. Liu, Y. Zhang, F. Liu, T. P. Russell, H. J. Snaith, R. Zhu, and Q. Gong, “High-Performance Inverted Planar Heterojunction Perovskite Solar Cells Based on Lead Acetate Precursor with Efficiency Exceeding 18%,” *Advanced Functional Materials*, 2016.

[47] J. Liu, C. Gao, X. He, Q. Ye, L. Ouyang, D. Zhuang, C. Liao, J. Mei, and W. Lau, “Improved Crystallization of Perovskite Films by Optimized Solvent Annealing for High Efficiency Solar Cell,” *ACS Appl. Mater. Interfaces*, vol. 7, no. 43, pp. 24008–24015, 2015.

[48] S. Venkatesan, F. Hao, J. Kim, Y. Rong, Z. Zhu, and Y. Liang, “Moisture-driven phase transition for improved perovskite solar cells with reduced trap-state density,” *Nano Res.*, vol. 10, no. 4, pp. 1413–1422, 2017.

[49] A. Dubey, N. Kantack, N. Adhikari, K. Reza, S. Venkatesan, M. Kumar, D. Khatiwada, S. Darling, and Q. Qiao, “Room Temperature, Air Crystallized Perovskite film for High Performance Solar Cells,” *J. Mater. Chem. A*, vol. 4, pp. 10231–10240, 2016.

[50] D. Bi, C. Yi, J. Luo, J.-D. Décoppet, F. Zhang, S. M. Zakeeruddin, X. Li, A. Hagfeldt, and M. Grätzel, “Polymer-templated nucleation and crystal growth of perovskite films for solar cells with efficiency greater than 21%,” *Nat. Energy*, vol. 1, no. September, p. 16142, 2016.

[51] G. E. Eperon, V. M. Burlakov, P. Docampo, A. Goriely, and H. J. Snaith, "Morphological control for high performance, solution-processed planar heterojunction perovskite solar cells," *Adv. Funct. Mater.*, vol. 24, no. 1, pp. 151–157, 2014.

[52] K. G. Stamplecoskie, J. S. Manser, and P. V Kamat, "Dual nature of the excited state in organic-inorganic lead halide perovskites," *Energy Environ. Sci.*, vol. 8, no. 1, pp. 208–215, 2015.

[53] J. S. Manser, B. Reid, and P. V. Kamat, "Evolution of Organic-Inorganic Lead Halide Perovskite from Solid-State Iodoplumbate Complexes," *J. Phys. Chem. C*, vol. 119, no. 30, pp. 17065–17073, 2015.

[54] L. Zhao, D. Luo, J. Wu, Q. Hu, W. Zhang, K. Chen, T. Liu, Y. Liu, Y. Zhang, F. Liu, T. P. Russell, H. J. Snaith, R. Zhu, and Q. Gong, "Perovskite Solar Cells: High-Performance Inverted Planar Heterojunction Perovskite Solar Cells Based on Lead Acetate Precursor with Efficiency Exceeding 18% (Adv. Funct. Mater. 20/2016)," *Adv. Funct. Mater.*, vol. 26, no. 20, pp. 3551–3551, May 2016.

[55] S. Venkatesan, F. Hao, J. Kim, Y. Rong, Z. Zhu, Y. Liang, J. Bao, and Y. Yao, "Moisture-driven phase transition for improved perovskite solar cells with reduced trap-state density," *Nano Res.*, vol. 10, no. 4, pp. 1413–1422, 2017.

[56] Z. Zhu, V. G. Hadjiev, Y. Rong, R. Guo, B. Cao, Z. Tang, F. Qin, Y. Li, Y. Wang, F. Hao, S. Venkatesan, W. Li, S. Baldelli, A. M. Guloy, H. Fang, Y. Hu, Y. Yao, Z. Wang, and J. Bao, "Interaction of organic cation with water molecule in perovskite MAPbI3: from dynamic orientational disorder to hydrogen bonding," *Chem. Mater.*, vol. 28, pp. 7385–7393, 2016.

[57] N. J. Jeon, J. H. Noh, Y. C. Kim, W. S. Yang, S. Ryu, and S. Il Seok, "Solvent engineering for high-performance inorganic-organic hybrid perovskite solar cells.," *Nat. Mater.*, vol. 13, no. July, pp. 1–7, 2014.

[58] B. Yang, O. Dyck, J. Poplawsky, J. Keum, A. Puretzky, S. Das, I. Ivanov, C. Rouleau, G. Duscher, D. Geohegan, and K. Xiao, "Perovskite Solar Cells with Near 100% Internal Quantum Efficiency Based on Large Single Crystalline Grains and Vertical Bulk Heterojunctions," *J. Am. Chem. Soc.*, vol. 137, no. 29, pp. 9210–9213, 2015.

[59] L. Oesinghaus, J. Schlipf, N. Giesbrecht, L. Song, Y. Hu, T. Bein, P. Docampo, and P. Müller-Buschbaum, "Toward Tailored Film Morphologies: The Origin of Crystal Orientation in Hybrid Perovskite Thin Films," *Advanced Materials Interfaces*, 2016.

[60] X. Huang, Z. Zhao, L. Cao, Y. Chen, E. Zhu, Z. Lin, M. Li, A. Yan, A. Zettl, Y. M. Wang, X. Duan, T. Mueller, and Y. Huang, "High-performance photovoltaic perovskite layers fabricated through intramolecular exchange," *Science (80-. ).*, vol. 348, no. 6240, pp. 1230–1234, 2015.

[61] J. Cao, X. Jing, J. Yan, C. Hu, R. Chen, J. Yin, J. Li, and N. Zheng, "Identifying the Molecular Structures of Intermediates for Optimizing the Fabrication of High-Quality Perovskite Films," *J. Am. Chem. Soc.*, vol. 138, no. 31, pp. 9919–9926, 2016.

[62] A. Dubey, N. Kantack, N. Adhikari, K. M. Reza, S. Venkatesan, M. Kumar, D. Khatiwada, S. Darling, and Q. Qiao, "Room temperature, air crystallized perovskite film for high performance solar cells," *J. Mater. Chem. A*, vol. 4, no. 26, pp. 10231–10240, 2016.

[63] P. Fan, D. Gu, G. X. Liang, J. T. Luo, J. L. Chen, Z. H. Zheng, and D. P. Zhang, "High-performance perovskite CH3 NH3 PbI3 thin films for solar cells prepared by single-source physical vapour deposition," *Sci. Rep.*, vol. 6, no. June, pp. 1–9, 2016.

[64] H. Gao, C. Bao, F. Li, T. Yu, J. Yang, W. Zhu, X. Zhou, G. Fu, and Z. Zou, "Nucleation and crystal growth of organic-inorganic lead halide perovskites under different relative humidity," *ACS Appl. Mater. Interfaces*, vol. 7, no. 17, pp. 9110–9117, 2015.

[65] P. Using, X. Di, T. J. Jacobsson, L. J. Schwan, M. Ottosson, A. Hagfeldt, and T. Edvinsson, “Determination of Thermal Expansion Coe ffi cients and Locating the Temperature-Induced Phase Transition in Methylammonium Lead Perovskites Using X - ray Di ff raction,” 2015.

[66] M. van S. and P. R. F. B. Aurélien M. A. Leguy, a Pooya Azarhoosh, M. Isabel Alonso, Mariano Campoy-Quiles, Oliver J. Weber, Jizhong Yao, Daniel Bryant, Mark T. Weller, Jenny Nelson, Aron Walsh, “Experimental and theoretical optical properties of methylammonium lead halide perovskites,” pp. 6317–6327, 2016.

[67] Y. Sun, Z. Yang, P. Gao, J. He, X. Yang, J. Sheng, S. Wu, Y. Xiang, and J. Ye, “Si/PEDOT:PSS Hybrid Solar Cells with Advanced Antireflection and Back Surface Field Designs,” *Nanoscale Res. Lett.*, vol. 11, no. 1, pp. 1–6, 2016.

[68] R. A. Synowicki, “Suppression of backside reflections from transparent substrates,” *Phys. Status Solidi Curr. Top. Solid State Phys.*, vol. 5, no. 5, pp. 1085–1088, 2008.

[69] S. Venkatesan, M. Hasan, J. Kim, N. R. Rady, S. Sohal, E. Neier, Y. Yao, and A. Zakhidov, “Tailoring nucleation and grain growth by changing the precursor phase ratio for efficient organic lead halide perovskite optoelectronic devices,” *J. Mater. Chem. C*, vol. 5, no. 39, pp. 10114–10121, 2017.

[70] C. Ma, H. Wang, W. Hu, W. Yu, A. D. Sheikh, F. Li, and T. Wu, “Ambipolar solution-processed hybrid perovskite phototransistors,” *Nat. Commun.*, vol. 6, pp. 1–8, 2015.

[71] H. S. Jung and N. G. Park, “Perovskite solar cells: From materials to devices,” *Small*, vol. 11, no. 1. pp. 10–25, 2015.

[72] W. Nie, H. Tsai, R. Asadpour, A. J. Neukirch, G. Gupta, J. J. Crochet, M. Chhowalla, S. Tretiak, M. a Alam, H. Wang, J.-C. Blancon, J. J. Crochet, H. Wang, and A. D. Mohite, “High-efficiency solution-processed perovskite solar cells with millimeter-scale grains,” *Science (80-. ).*, vol. 347, no. 6221, pp. 522–525, 2015.

[73] Y. Shao, Z. Xiao, C. Bi, Y. Yuan, and J. Huang, “Origin and elimination of photocurrent hysteresis by fullerene passivation in CH3NH3PbI3 planar heterojunction solar cells,” *Nat. Commun.*, vol. 5, pp. 1–7, 2014.

[74] T. Oku, “Crystal Structures and Related Perovskite Compounds Used for Solar Cells,” *Sol. Cells - New Approaches Rev.*, pp. 77–101, 2015.

[75] S.-S. Li, C.-H. Chang, Y.-C. Wang, C.-W. Lin, D.-Y. Wang, J.-C. Lin, C.-C. Chen, H.-S. Sheu, H.-C. Chia, W.-R. Wu, U.-S. Jeng, C.-T. Liang, R. Sankar, F.-C. Chou, and C.-W. Chen, “Intermixing-seeded growth for high-performance planar heterojunction perovskite solar cells assisted by precursor-capped nanoparticles,” *Energy Environ. Sci.*, vol. 9, no. 1, pp. 1282–1289, 2016.

[76] P. W. Liang, C. Y. Liao, C. C. Chueh, F. Zuo, S. T. Williams, X. K. Xin, J. Lin, and A. K. Y. Jen, “Additive enhanced crystallization of solution-processed perovskite for highly efficient planar-heterojunction solar cells,” *Adv. Mater.*, vol. 26, no. 22, pp. 3748–3754, 2014.

[77] V. A. Online, “Enhanced e ffi ciency of planar perovskite solar cells via a two-step deposition using DMF as an additive to optimize the crystal growth behavior †,” pp. 13032–13038, 2017.

[78] Y. Rong, Z. Tang, Y. Zhao, X. Zhong, S. Venkatesan, H. Graham, M. Patton, Y. Jing, A. M. Guloy, and Y. Yao, “Solvent engineering towards controlled grain growth in perovskite planar heterojunction solar cells,” *Nanoscale*, vol. 7, no. 24, p. pp 10595-10599, 2015.

[79] T. Liu, F. Jiang, J. Tong, F. Qin, W. Meng, Y. Jiang, Z. Li, and Y. Zhou, “Reduction and oxidation of poly(3,4-ethylenedioxythiophene):poly(styrenesulfonate) induced by methylamine (CH3NH2)-containing atmosphere for perovskite solar cells,” *J. Mater. Chem. A*, vol. 00, pp. 1–7, 2016.

[80] W. Yang, Y. Yao, and C. Q. Wu, “Origin of the high open circuit voltage in planar heterojunction perovskite solar cells: Role of the reduced bimolecular recombination,” *J. Appl. Phys.*, vol. 117, no. 9, 2015.

[81] D. Ompong and J. Singh, “High open-circuit voltage in perovskite solar cells: The role of hole transport layer,” *Org. Electron. physics, Mater. Appl.*, vol. 63, no. June, pp. 104–108, 2018.

[82] M. Yang, T. Zhang, P. Schulz, Z. Li, G. Li, D. H. Kim, N. Guo, J. J. Berry, K. Zhu, and Y. Zhao, “Facile fabrication of large-grain CH3NH3PbI3-xBrx films for high-efficiency solar cells via CH3NH3Br-selective Ostwald ripening,” *Nat. Commun.*, vol. 7, no. May, pp. 2–10, 2016.

[83] Q. Fu, X. Tang, B. Huang, T. Hu, L. Tan, L. Chen, and Y. Chen, “Recent Progress on the Long-Term Stability of Perovskite Solar Cells,” *Adv. Sci.*, vol. 5, no. 5, p. 1700387, May 2018.

[84] M. I. Asghar, J. Zhang, H. Wang, and P. D. Lund, “Device stability of perovskite solar cells – A review,” *Renew. Sustain. Energy Rev.*, vol. 77, pp. 131–146, Sep. 2017.

[85] D. Wang, M. Wright, N. K. Elumalai, and A. Uddin, “Stability of perovskite solar cells,” *Sol. Energy Mater. Sol. Cells*, vol. 147, pp. 255–275, Apr. 2016.

[86] L. Contreras-Bernal, C. Aranda, M. Valles-Pelarda, T. T. Ngo, S. Ramos-Terrón, J. J. Gallardo, J. Navas, A. Guerrero, I. Mora-Seró, J. Idígoras, and J. A. Anta, “Homeopathic Perovskite Solar Cells: Effect of Humidity during Fabrication on the Performance and Stability of the Device,” *J. Phys. Chem. C*, vol. 122, no. 10, pp. 5341–5348, Mar. 2018.

[87] S.-W. Lee, S. Kim, S. Bae, K. Cho, T. Chung, L. E. Mundt, S. Lee, S. Park, H. Park, M. C. Schubert, S. W. Glunz, Y. Ko, Y. Jun, Y. Kang, H.-S. Lee, and D. Kim, “UV Degradation and Recovery of Perovskite Solar Cells,” *Sci. Rep.*, vol. 6, no. 1, p. 38150, Dec. 2016.

[88] Y. Sun, X. Fang, Z. Ma, L. Xu, Y. Lu, Q. Yu, N. Yuan, and J. Ding, “Enhanced UV-light stability of organometal halide perovskite solar cells with interface modification and a UV absorption layer,” *J. Mater. Chem. C*, vol. 5, no. 34, pp. 8682–8687, Aug. 2017.

[89] J. Yang, Z. Yuan, X. Liu, S. Braun, Y. Li, J. Tang, F. Gao, C. Duan, M. Fahlman, and Q. Bao, “Oxygen- and Water-Induced Energetics Degradation in Organometal Halide Perovskites,” *ACS Appl. Mater. Interfaces*, vol. 10, no. 18, pp. 16225–16230, May 2018.

[90] N. Aristidou, C. Eames, I. Sanchez-Molina, X. Bu, J. Kosco, M. S. Islam, and S. A. Haque, “Fast oxygen diffusion and iodide defects mediate oxygen-induced degradation of perovskite solar cells,” *Nat. Commun.*, vol. 8, p. 15218, May 2017.

[91] G. Niu, X. Guo, and L. Wang, “Review of recent progress in chemical stability of perovskite solar cells,” *J. Mater. Chem. A*, vol. 3, no. 17, pp. 8970–8980, Apr. 2015.

[92] A. Dualeh, P. Gao, S. Il Seok, M. K. Nazeeruddin, and M. Grätzel, “Thermal Behavior of Methylammonium Lead-Trihalide Perovskite Photovoltaic Light Harvesters,” *Chem. Mater.*, vol. 26, no. 21, pp. 6160–6164, Nov. 2014.

[93] N. Ashurov, B. L. Oksengendler, S. Maksimov, S. Rashiodva, A. R. Ishteev, D. S. Saranin, I. N. Burmistrov, D. V. Kuznetsov, and A. A. Zakhisov, “Current state and perspectives for organo-halide perovskite solar cells. Part 1. Crystal structures and thin film formation, morphology, processing, degradation, stability improvement by carbon nanotubes. A review,” *Mod. Electron. Mater.*, vol. 3, no. 1, pp. 1–25, Mar. 2017.

[94] Y. Liu, K. Palotas, X. Yuan, T. Hou, H. Lin, Y. Li, and S.-T. Lee, “Atomistic Origins of Surface Defects in $CH_3NH_3PbBr_3$ Perovskite and Their Electronic Structures,” *ACS Nano*, vol. 11, no. 2, pp. 2060–2065, Feb. 2017.

[95] W. Nie, J.-C. Blancon, A. J. Neukirch, K. Appavoo, H. Tsai, M. Chhowalla, M. A. Alam, M. Y. Sfeir, C. Katan, J. Even, S. Tretiak, J. J. Crochet, G. Gupta, and A. D. Mohite, "Light-activated photocurrent degradation and self-healing in perovskite solar cells," *Nat. Commun.*, vol. 7, p. 11574, May 2016.

[96] A. Singh, P. K. Nayak, S. Banerjee, Z. Wang, J. T.-W. Wang, H. J. Snaith, and K. S. Narayan, "Insights Into the Microscopic and Degradation Processes in Hybrid Perovskite Solar Cells Using Noise Spectroscopy," *Sol. RRL*, vol. 2, no. 1, p. 1700173, Jan. 2018.

[97] P. S. Whitfield, N. Herron, W. E. Guise, K. Page, Y. Q. Cheng, I. Milas, and M. K. Crawford, "Structures, Phase Transitions and Tricritical Behavior of the Hybrid Perovskite Methyl Ammonium Lead Iodide," *Sci. Rep.*, vol. 6, no. 1, p. 35685, Dec. 2016.

[98] V. Sarritzu, N. Sestu, D. Marongiu, X. Chang, S. Masi, A. Rizzo, S. Colella, F. Quochi, M. Saba, A. Mura, and G. Bongiovanni, "Optical determination of Shockley-Read-Hall and interface recombination currents in hybrid perovskites," *Sci. Rep.*, vol. 7, p. 44629, Mar. 2017.

[99] J. M. Frost and A. Walsh, "What is moving in hybrid halide perovskite solar cells?," Jan. 2016.

[100] M. C. Gélvez-Rueda, N. Renaud, and F. C. Grozema, "Temperature Dependent Charge Carrier Dynamics in Formamidinium Lead Iodide Perovskite," *J. Phys. Chem. C*, vol. 121, no. 42, pp. 23392–23397, Oct. 2017.

[101] L. Contreras-Bernal, M. Salado, A. Todinova, L. Calio, S. Ahmad, J. Idígoras, and J. A. Anta, "Origin and Whereabouts of Recombination in Perovskite Solar Cells," *J. Phys. Chem. C*, vol. 121, no. 18, pp. 9705–9713, May 2017.

[102] T. S. Sherkar, C. Momblona, L. Gil-Escrig, J. Ávila, M. Sessolo, H. J. Bolink, and L. J. A. Koster, "Recombination in Perovskite Solar Cells: Significance of Grain Boundaries, Interface Traps, and Defect Ions," *ACS Energy Lett.*, vol. 2, no. 5, pp. 1214–1222, May 2017.

[103] D. B. Khadka, Y. Shirai, M. Yanagida, T. Masuda, and K. Miyano, “Enhancement in efficiency and optoelectronic quality of perovskite thin films annealed in MACl vapor,” *Sustain. Energy Fuels*, vol. 1, no. 4, pp. 755–766, 2017.

[104] Y. Cheng, H.-W. Li, J. Qing, Q.-D. Yang, Z. Guan, C. Liu, S. H. Cheung, S. K. So, C.-S. Lee, and S.-W. Tsang, “The detrimental effect of excess mobile ions in planar $CH_3NH_3PbI_3$ perovskite solar cells,” *J. Mater. Chem. A*, vol. 4, no. 33, pp. 12748–12755, Aug. 2016.

[105] Energetiq Inc., “ENERGETIQ - Laser-Driven Light Sources.” .

[106] N. Elumalai, M. Mahmud, D. Wang, and A. Uddin, “Perovskite Solar Cells: Progress and Advancements,” *Energies*, vol. 9, no. 11, p. 861, Oct. 2016.

[107] L. T. Schelhas, J. A. Christians, J. J. Berry, M. F. Toney, C. J. Tassone, J. M. Luther, and K. H. Stone, “Monitoring a Silent Phase Transition in $CH_3NH_3PbI_3$ Solar Cells via *Operando* X-ray Diffraction,” *ACS Energy Lett.*, vol. 1, no. 5, pp. 1007–1012, Nov. 2016.

[108] W. A. Saidi and J. J. Choi, “Nature of the cubic to tetragonal phase transition in methylammonium lead iodide perovskite,” *J. Chem. Phys.*, vol. 145, no. 14, p. 144702, Oct. 2016.

[109] Y.-Y. Zhang, S. Chen, P. Xu, H. Xiang, X.-G. Gong, A. Walsh, and S.-H. Wei, “Intrinsic Instability of the Hybrid Halide Perovskite Semiconductor $CH_3NH_3PbI_3$ *,” *Chinese Phys. Lett.*, vol. 35, no. 3, p. 036104, Mar. 2018.

[110] Y. Kawamura, H. Mashiyama, and K. Hasebe, “Structural Study on Cubic–Tetragonal Transition of $CH_3NH_3PbI_3$,” *J. Phys. Soc. Japan*, vol. 71, no. 7, pp. 1694–1697, Jul. 2002.

[111] V. Sarritzu, N. Sestu, D. Marongiu, X. Chang, S. Masi, A. Rizzo, S. Colella, F. Quochi, M. Saba, A. Mura, and G. Bongiovanni, “Optical determination of Shockley-Read-Hall and interface recombination currents in hybrid perovskites.,” *Sci. Rep.*, vol. 7, p. 44629, Mar. 2017.

[112] D. B. Khadka, Y. Shirai, M. Yanagida, and K. Miyano, “Degradation of encapsulated perovskite solar cells driven by deep trap states and interfacial deterioration,” *J. Mater. Chem. C*, vol. 6, no. 1, pp. 162–170, 2018.

[113] S. Paul, S. Grover, I. L. Repins, B. M. Keyes, M. A. Contreras, K. Ramanathan, R. Noufi, Z. Zhao, F. Liao, and J. V. Li, “Analysis of Back-Contact Interface Recombination in Thin-Film Solar Cells,” *IEEE J. Photovoltaics*, vol. 8, no. 3, pp. 871–878, May 2018.

[114] N. K. Elumalai and A. Uddin, “Open circuit voltage of organic solar cells: an in-depth review,” *Energy Environ. Sci.*, vol. 9, no. 2, pp. 391–410, Feb. 2016.

[115] S. S. Hegedus and W. N. Shafarman, “Thin-film solar cells: device measurements and analysis,” *Prog. Photovoltaics Res. Appl.*, vol. 12, no. 23, pp. 155–176, Mar. 2004.

[116] N.-K. Kim, Y. H. Min, S. Noh, E. Cho, G. Jeong, M. Joo, S.-W. Ahn, J. S. Lee, S. Kim, K. Ihm, H. Ahn, Y. Kang, H.-S. Lee, and D. Kim, “Investigation of Thermally Induced Degradation in CH3NH3PbI3 Perovskite Solar Cells using In-situ Synchrotron Radiation Analysis,” *Sci. Rep.*, vol. 7, no. 1, p. 4645, Dec. 2017.

[117] F. Gao, Z. Li, J. Wang, A. Rao, I. A. Howard, A. Abrusci, S. Massip, C. R. McNeill, and N. C. Greenham, “Trap-Induced Losses in Hybrid Photovoltaics,” *ACS Nano*, vol. 8, no. 4, pp. 3213–3221, Apr. 2014.

[118] C. L. Davies, M. R. Filip, J. B. Patel, T. W. Crothers, C. Verdi, A. D. Wright, R. L. Milot, F. Giustino, M. B. Johnston, and L. M. Herz, “Bimolecular recombination in methylammonium lead triiodide perovskite is an inverse absorption process,” *Nat. Commun.*, vol. 9, no. 1, p. 293, Dec. 2018.

[119] T. Hahn, S. Tscheuschner, F.-J. Kahle, M. Reichenberger, S. Athanasopoulos, C. Saller, G. C. Bazan, T.-Q. Nguyen, P. Strohriegl, H. Bässler, and A. Köhler, “Monomolecular and Bimolecular Recombination of Electron-Hole Pairs at the Interface of a Bilayer Organic Solar Cell,” *Adv. Funct. Mater.*, vol. 27, no. 1, p. 1604906, Jan. 2017.

[120] H. Li, K. Cao, J. Cui, S. Liu, X. Qiao, Y. Shen, and M. Wang, “14.7% efficient mesoscopic perovskite solar cells using single walled carbon nanotubes/carbon composite counter electrodes,” *Nanoscale*, vol. 8, no. 12, pp. 6379–6385, Mar. 2016.

[121] S. Bi, X. Zhang, L. Qin, R. Wang, J. Zhou, X. Leng, X. Qiu, Y. Zhang, H. Zhou, and Z. Tang, “Incorporating an Inert Polymer into the Interlayer Passivates Surface Defects in Methylammonium Lead Halide Perovskite Solar Cells,” *Chem. - A Eur. J.*, vol. 23, no. 58, pp. 14650–14657, Oct. 2017.

[122] Z. Sun, G. Sitbon, T. Pons, A. A. Bakulin, and Z. Chen, “Reduced Carrier Recombination in PbS - CuInS2 Quantum Dot Solar Cells,” *Sci. Rep.*, vol. 5, no. 1, p. 10626, Sep. 2015.

[123] H. Cho, S.-H. Jeong, M.-H. Park, Y.-H. Kim, C. Wolf, C.-L. Lee, J. H. Heo, A. Sadhanala, N. Myoung, S. Yoo, S. H. Im, R. H. Friend, and T.-W. Lee, “Overcoming the electroluminescence efficiency limitations of perovskite light-emitting diodes,” *Science*, vol. 350, no. 6265, pp. 1222–1225, 2015.

[124] X. Y. Chin, D. Cortecchia, J. Yin, A. Bruno, and C. Soci, “Lead Iodide Perovskite Light-Emitting Field-Effect Transistor,” *Arxiv*, vol. 6, no. May, p. Advance, 2015.

[125] H. Zhu, Y. Fu, F. Meng, X. Wu, Z. Gong, Q. Ding, M. V Gustafsson, M. T. Trinh, S. Jin, and X.-Y. Zhu, “Lead halide perovskite nanowire lasers with low lasing thresholds and high quality factors.,” *Nat. Mater.*, vol. 14, no. 6, pp. 636–642, 2015.

[126] H.-Y. Hsu, L. Ji, H. S. Ahn, J. Zhao, E. T. Yu, and A. J. Bard, “A Liquid Junction Photoelectrochemical Solar Cell Based on p-Type MeNH3PbI3 Perovskite with 1.05 V Open-Circuit Photovoltage,” *J. Am. Chem. Soc.*, vol. 137, no. 46, pp. 14758–14764, Nov. 2015.

[127] Z. Li, C. C. Mercado, M. Yang, E. Palay, K. Zhu, C. Bi, P. Sharma, A. Gruverman, J. Huang, N. G. Park, Y. E. Romanyuk, S. Buecheler, S. D. Tilley, L. H. Wong, A. N. Tiwari, and M. Grätzel, "Electrochemical impedance analysis of perovskite–electrolyte interfaces," *Chem. Commun.*, vol. 53, no. 16, pp. 2467–2470, Feb. 2017.

[128] C. M. Hansen, *Hansen Solubility Parameters: A User's Handbook, Second Edition*. .

[129] A. A. Zakhidov, J. K. Lee, H. H. Fong, J. A. DeFranco, M. Chatzichristidi, P. G. Taylor, C. K. Ober, and G. G. Malliaras, "Hydrofluoroethers as orthogonal solvents for the chemical processing of organic electronic materials," *Adv. Mater.*, vol. 20, pp. 3481–3484, 2008.

[130] A. A. Zakhidov, B. Lüssem, K. Leo, and J. Defranco, "P-170 : Influence of HFE Solvent Processing on OLED Lifetime," *SID Symp. Dig. Tech. Pap.*, vol. 42, no. 1, pp. 1740–1741, 2011.

[131] A. A. Zakhidov, S. Reineke, B. Lüssem, and K. Leo, "Hydrofluoroethers as heat-transfer fluids for OLEDs: Operational range, stability, and efficiency improvement," *Org. Electron.*, vol. 13, no. 3, pp. 356–360, Mar. 2012.

[132] S. Krotkus, F. Nehm, R. Janneck, S. Kalkura, A. A. Zakhidov, M. Schober, O. R. Hild, D. Kasemann, S. Hofmann, K. Leo, and S. Reineke, "Influence of bilayer resist processing on p-i-n OLEDs: towards multicolor photolithographic structuring of organic displays," *Proc. SPIE*, vol. 9360, p. 93600W, 2015.

[133] G. Nagasubramanian and C. J. Orendorff, "Hydrofluoroether electrolytes for lithium-ion batteries: Reduced gas decomposition and nonflammable," *J. Power Sources*, vol. 196, no. 20, pp. 8604–8609, 2011.

[134] K. Naoi, E. Iwama, N. Ogihara, Y. Nakamura, H. Segawa, and Y. Ino, "Nonflammable Hydrofluoroether for Lithium-Ion Batteries: Enhanced Rate Capability, Cyclability, and Low-Temperature Performance," *J. Electrochem. Soc.*, vol. 156, no. 4, p. A272, 2009.

[135] W. T. Tsai, “Environmental risk assessment of hydrofluoroethers (HFEs),” *J. Hazard. Mater.*, vol. 119, no. December 2004, pp. 69–78, 2005.

[136] I. M. Smallwood, *Handbook of Organic Solvent Properties.* John Wiley & Sons, 1996.

[137] E. R. S. Circular, N B S, Arthur A. Maryott, *Table of Dielectric Constants of Pure Liquids*. 1951.

[138] W. Nie, H. Tsai, R. Asadpour, J.-C. Blancon, A. J. Neukirch, G. Gupta, J. J. Crochet, M. Chhowalla, S. Tretiak, M. A. Alam, H.-L. Wang, and A. D. Mohite, “High-efficiency solution-processed perovskite solar cells with millimeter-scale grains,” *Science (80-. ).*, vol. 347, no. 6221, pp. 522–525, 2015.

[139] J. Burschka, N. Pellet, S.-J. Moon, R. Humphry-Baker, P. Gao, M. K. Nazeeruddin, and M. Grätzel, “Sequential deposition as a route to high-performance perovskite-sensitized solar cells.,” *Nature*, vol. 499, no. 7458, pp. 316–9, 2013.

[140] M. Xiao, F. Huang, W. Huang, Y. Dkhissi, Y. Zhu, J. Etheridge, A. Gray-Weale, U. Bach, Y.-B. Cheng, and L. Spiccia, “A Fast Deposition-Crystallization Procedure for Highly Efficient Lead(supporting),” *Angew. Chemie*, vol. 126, no. 37, pp. 10056–10061, 2014.

[141] M. Hasan, S. Venkatesan, D. Lyashenko, J. D. Slinker, and A. Zakhidov, “Solvent Toolkit for Electrochemical Characterization of Hybrid Perovskite Films,” *Anal. Chem.*, vol. 89, no. 18, pp. 9649–9653, 2017.

[142] H. S. Jung and N. G. Park, “Perovskite solar cells: From materials to devices,” *Small*, vol. 11, no. 1, pp. 10–25, 2015.

[143] X. Zhou, X. Li, Y. Liu, F. Huang, and D. Zhong, “Interface electronic properties of co-evaporated MAPbI3 on ZnO(0001): In situ X-ray photoelectron spectroscopy and ultraviolet photoelectron spectroscopy study,” *Applied Physics Letters*, vol. 108, no. 12. p. 121601, 2016.

[144] V. Adinolfi, M. Yuan, R. Comin, E. S. Thibau, D. Shi, M. I. Saidaminov, P. Kanjanaboos, D. Kopilovic, S. Hoogland, Z. H. Lu, O. M. Bakr, and E. H. Sargent, "The In-Gap Electronic State Spectrum of Methylammonium Lead Iodide Single-Crystal Perovskites," *Adv. Mater.*, vol. 28, no. 17, pp. 3406–3410, 2016.

[145] C. Manspeaker, "Role of the cation in hybrid orgainc-inorganic perovskite solar materials," 2018.

[146] Q. Jiang, M. Chen, J. Li, M. Wang, X. Zeng, T. Besara, J. Lu, Y. Xin, X. Shan, B. Pan, C. Wang, S. Lin, T. Siegrist, Q. Xiao, and Z. Yu, "Electrochemical Doping of Halide Perovskites with Ion Intercalation," *ACS Nano*, vol. 11, no. 1, pp. 1073–1079, 2017.